Electrochemical Modulation and Restructuring of Planar Metallic Metamaterials

Zur Erlangung des akademischen Grades eines
Doktors der Naturwissenschaften
der Fakultät für Physik des
Karlsruher Instituts für Technologie (KIT)

genehmigte

Dissertation

von

Diplom-Physiker Matthias Ruther
aus Ostfildern-Ruit

Tag der mündlichen Prüfung: 15. April 2011
Referent: Prof. Dr. Martin Wegener
Korreferent: Prof. Dr. Kurt Busch

Contents

Publications

Parts of this work have already been published in refereed scientific journals

- L.-H. Shao, M. Ruther, S. Linden, J. Weissmüller, S.Essig, K. Busch, and M. Wegener "Electrochemical Modulation of Photonic Metamaterials," Advanced Materials **22**, 5173–5177 (2010)

- M. Ruther, L.-H. Shao, S. Linden, J. Weissmüller, and M. Wegener "Electrochemical restructuring of plasmonic metamaterials," Appl. Phys. Lett. **98**, 013112 (2011)

Additional work on other topics has been published in refereed scientific journals

- M. Wegener, J. L.Garcia-Pomar, C. M. Soukoulis, N. Meinzer, M. Ruther, and S. Linden "Toy model for plasmonic metamaterial resonances coupled to two-level system gain," Opt. Express **16**, 19785–19798 (2008)

- M. Decker, M. Ruther, C. E. Kriegler, J. Zhou, C. M. Soukoulis, S. Linden, and M. Wegener "Strong optical activity from twisted-cross photonic metamaterials," Opt. Lett. **34**, 2501–2503 (2009)

- N. Meinzer, M. Ruther, S. Linden, C. M. Soukoulis, G. Khitrova, J. Hendrickson, J. D. Olitzky, H. M. Gibbs, and M. Wegener "Arrays of Ag split-ring resonators coupled to InGaAs single-quantum-well gain," Opt. Exp. **18**, 24140–24151 (2010)

Parts of this work have already been presented on international conferences (only own presentation)

- S. Linden, M. Ruther, L.-H. Shao, J. Weissmüller, S.Essig, K. Busch, and M. Wegener "Electrochemical Modulation of Photonic Metamaterials," CLEO/QELS San José, California (USA), QThB3 (2010)

Chapter 1

Introduction

The field of metallic photonic metamaterials and plasmonics in general has become an integral part of optics over the last years. The word metamaterial is an umbrella term for an artificially composed structure, which typically consists of periodically arranged metallic building blocks as smallest functional elements, interacting with the light field and each other. Compared to natural materials, whose optical properties for the case of a crystal, are determined by the periodically arranged atoms and their interaction with the light field, one obviously finds similarities.

Therfore, these kind of artificial materials can be treated as an effective material, as long as the wavelength of the interacting light is much smaller than the dimension and the lattice constants of the periodically arranged elements. The optical properties can now be controlled by the shape and composition of the building blocks, which the metamaterial consists of. This mighty concept offers the opportunity to design materials with desired optical properties and even to create novel optical phenomena, which are not accessible within natural materials.

The conceptional starting point for this success story began in the year 1968, when the Russian physicist V. Veselago theoretically discussed the optical properties of a fictitious material, which exhibits a negative magnetic- and electric response represented by the permeability $\mu < 0$ and permittivity $\epsilon < 0$, as underlying optical material parameters [1]. Veselago predicted, that a material of this kind would enable extraordinary phenomena such as negative refraction, an inverse Doppler shift or inverse Cerenkov radiation - just to give a selection of the effects predicted. For a long time this work has only been of theoretical interest, being due to the fact that the material described by Veselago, especially the property of a negative permeability, had not been present in the optical regime.

This changed, after Pendry and colleagues presented a novel metamaterial design consisting of a metallic ring geometry with a small intersection, the so-called split-ring resonator [2]. Within this resonator an oscillating ring current can be excited by an external magnetic field, which leads to a magnetic response and a permeability $\mu < 0$.

Another milestone, which demonstrated the experimental realization of Veselago's vision, has been presented by Shelby and his coworkers, who introduced a structure design consisting of the split-ring concept and long metallic wires. This hybrid structure designed for the microwave regime exhibits both, a negative magnetic permeability and electric permittivity,

and fulfills the conditions Veselago predicted for a material with a negative refractive index. Over the last years, the achievements within the field of micro- and nano-structuring have brought the concept of metamaterials closer to the optical spectral range. Astonishing effects mediated by metallic nano-structures, exhibiting a negative permeability at frequencies of 100 THz and structures with a negative index of refraction even in the optical spectral range, have been presented [3, 4].

A further stimulus has been performed by the field of transformation optics, which afforded the concept of cloaking presented by Leonhard and Pendry [5, 6]. The field of transformation optics provides the opportunity to guide light onto a desired path within a material by tailoring the spatial distribution of the permeability $\mu(\boldsymbol{x})$ and permittivity $\epsilon(\boldsymbol{x})$. Works inspired by this concept lead to remarkable improvements in the fields of photonic metamaterials and fabrication technologies [7–11].

Beyond this, some approaches may have the potential to pave the way towards future applications. On that way, the work of Pendry has been one of the driving forces. Pendry proposed, that a thin slab of a negative index metamaterial enables to perform sub-wavelength or even perfect imaging [12]. A promising transposition has been given by Fang *et al.*, who presented a design composed of a thin silver film, used for imaging a grid into a photo resist [13]. Within this setup, Fang demonstrated the possibility to gain a sub-wavelength image of the grid within the photo resist.

A major goal in research developments on photonic metamaterials is given by realizing the discussed phenomena in the visible spectral range [14, 15]. Most of the effects discussed are related to resonant excitations of metallic nano-structures. The performance of these effects suffers from metal intrinsic losses especially for visible wavelength of light. Additionally, nano-scale metal objects typically show increased losses compared to metal films or bulk metal properties [16]. Therefore, possible applications of metamaterials and small metallic nano-structures in general are strongly dependent on this metal intrinsic insufficiencies. Hence, a lot of effort has been spent on compensation strategies of these losses. Approaches on metal improvement and gain-mediated loss compensations strategies have been presented [17, 18].

Furthermore, possible future applications of photonic structures require for a spectral tunability and modulation of the underlying resonances to bring the desired optical properties in the region of interest. This can be achieved by a size scaling of the underlying metal objects [19]. Concerning applications, methods providing a continuous and reversible resonance modulation of plasmonic structures and its corresponding optical properties would be desirable. Promising approaches based on field-effect metal-semiconductor composite structures have been reported for terahertz frequencies [20, 21]. In the visible spectral range, works on electrochemically modulating the optical properties of chemically synthesized metal nano-crystals and influencing surface plasmon polaritons, excited within thin gold films, have been presented [22, 23].

Beyond the established work on modulating the optical properties of metals, we present an electrochemical approach based on metamaterial structures, being intermediate in size between gold nano-crystals and thin gold films. This is of fundamental interest, since this size

regime is characteristic of near-infrared- and optical metamaterials.

Additionally, our electrochemical approach provides the possibility to reduce losses within the metallic metamaterial structures. These observations are based on an electrochemically induced metal surface improvement, making our work distinct from the present concepts of thermal annealing or incorporating gain-materials to achieve loss reductions.

The results presented in this thesis give rise to the assumption, that our electrochemical approach could contribute to help paving the way towards possible future applications incorporating photonic metamaterials.

Outline of this thesis

This work deals with two aspects of electrochemically manipulating arrays of plasmonic nano-structures: (i) actively influencing the resonance properties of plasmonic nano-structures by modulating the resonance position and line-widths and (ii) restructuring of plasmonic nano-structures aiming a reduction of Ohmic losses .

Along these lines, in chapter 2 we present the basic principles of optics, giving the theoretical framework based on linear interaction of light with matter and giving an overview about the the loss mechanisms, especially for thin metallic films and wires, describing the constituents a metamaterial building block typically consists of. Chapter 3 comprises the fundamental concepts of metamaterials starting with the optical properties of effective media and introducing the split-ring resonator as a famous representative for metamaterial building blocks. By presenting specific metamaterial effects, which are extraordinary and equally vivid, we would like to stimulate the reader's interest for this exciting field of research. The fabrication and characterization of the photonic metamaterials are discussed in chaper 5 and 6, comprising all manufacturing steps and fabrication techniques as well as the characterization procedure before, during and after the electrochemical treatment. In chapter 4 we introduce the reader to the conceptual framework of the electrochemically induced phenomena, the optical modulation and -restructuring effects are based on. The results of our experimental investigations are summarized in chapter 7 and 8. The phenomena of surface restructuring and electrochemical modulation are historically linked, but are seperately discussed. This is due to the different mechanisms, these effects – especially the reversible modulations – are based on.

The spectral modulation shows huge shifts of up to 55 THz, which is more than 18 % of the corresponding central frequency. The observed modulation effects consist of reversible as well as irreversible fractions, of which the reversible effets dominate. Both factors are investigated systematically and discussed in terms of spectral and line-width modulation.

For restructuring nano-sized metallic antennae we achieved a Ohmic loss reduction for thin-metal films exceeding factors of three. Even for 30 nm thick nano-structures, we find loss reductions up to 30 %.

Finally, we conclude our findings and give an outlook about the classification of our work within the scientific context.

Chapter 2

Principles of Optics

The optical properties of metamaterials can be deduced from the interaction of light with matter which can be understood in a classical framework and described with the formalism of Maxwell's equations. In this notion, the interaction of the electromagnetic wave with matter depends on the amplitude of the wave and can be classified into linear and nonlinear interactions with the constituting materials. For this work we can limit our considerations on the linear optical effects, since we are using thermal emitters for spectroscopy only.

We discuss the electromagnetic response of dielectrics, idealized- and real metals over a broad spectral range. We separately discuss the mechanism of damping in general and especially for bulk metals as well as metallic nano-structures. We end up with the formalism describing the charge density oscillations in metallic films and particles forming the basic framework in understanding the optical behavior of metamaterials.

2.1 Basics of Linear Optics

2.1.1 Maxwell's Equations

The behavior of electromagnetic fields in media - in the classical picture - are described by the macroscopic Maxwell equations. In SI-units, they are defined according to [24]:

$$\nabla \cdot \boldsymbol{D}(\boldsymbol{r},t) = \rho(\boldsymbol{r},t), \tag{2.1a}$$

$$\nabla \cdot \boldsymbol{B}(\boldsymbol{r},t) = 0, \tag{2.1b}$$

$$\nabla \times \boldsymbol{E}(\boldsymbol{r},t) = -\frac{\partial \boldsymbol{B}(\boldsymbol{r},t)}{\partial t}, \tag{2.1c}$$

$$\nabla \times \boldsymbol{H}(\boldsymbol{r},t) = \boldsymbol{j}(\boldsymbol{r},t) + \frac{\partial \boldsymbol{D}(\boldsymbol{r},t)}{\partial t}. \tag{2.1d}$$

These equations connect the four macroscopic fields, the dielectric displacement $\boldsymbol{D}(\boldsymbol{r},t)$, the electric field $\boldsymbol{E}(\boldsymbol{r},t)$, the magnetic field $\boldsymbol{H}(\boldsymbol{r},t)$, and the magnetic induction $\boldsymbol{B}(\boldsymbol{r},t)$, with the external charge density $\rho(\boldsymbol{r},t)$ and the external current density $\boldsymbol{j}(\boldsymbol{r},t)$.

The external charge density and the external current density are connected through the charge

conservation law, which can be expressed in the following form:

$$\nabla \cdot \boldsymbol{j}(\boldsymbol{r}, t) + \frac{\partial \rho(\boldsymbol{r}, t)}{\partial t} = 0. \tag{2.2}$$

In our notation, we use the "external" charge separations and currents ($\rho(\boldsymbol{r}, t)$, $\boldsymbol{j}(\boldsymbol{r}, t)$) for discribing the stimulus of the system, whereas all "internal" charge separations and currents are the response induced by the driving fields and lead to a macroscopic electric polarization $\boldsymbol{P}$ and a macroscopic magnetization $\boldsymbol{M}$. Therfore, the wave propagation in media is described by the material equations, which link the dielectric displacement and the magnetic induction with the electric and magnetic field. They are given by:

$$\boldsymbol{D}(\boldsymbol{r}, t) = \epsilon_0 \boldsymbol{E}(\boldsymbol{r}, t) + \boldsymbol{P}(\boldsymbol{r}, t), \tag{2.3a}$$

$$\boldsymbol{B}(\boldsymbol{r}, t) = \mu_0 \boldsymbol{H}(\boldsymbol{r}, t) + \boldsymbol{M}(\boldsymbol{r}, t), \tag{2.3b}$$

where ϵ_0 and μ_0 are the permittivity[1] and the permeability[2] of free space. They are connected by the relation: $\epsilon_0 = \frac{1}{c_0^2 \mu_0}$ with the vacuum speed of light[3].
The polarization and the magnetization are connected to the external fields $\boldsymbol{E}$ and $\boldsymbol{H}$, by the electric and magnetic susceptibilities $\chi_{\mathrm{e}}(\boldsymbol{r} - \boldsymbol{r}', t - t')$ and $\chi_{\mathrm{m}}(\boldsymbol{r} - \boldsymbol{r}', t - t')$, respectively. Thus, the polarization and magnetization are given by [24]:

$$\boldsymbol{P}(\boldsymbol{r}, t) = \int_{-\infty}^{\infty} \int_{-\infty}^{t} \epsilon_0 \chi_{\mathrm{e}}(\boldsymbol{r} - \boldsymbol{r}', t - t') \boldsymbol{E}(\boldsymbol{r}', t') \mathrm{d}t' \mathrm{d}^3 r', \tag{2.4a}$$

$$\boldsymbol{M}(\boldsymbol{r}, t) = \int_{-\infty}^{\infty} \int_{-\infty}^{t} \mu_0 \chi_{\mathrm{m}}(\boldsymbol{r} - \boldsymbol{r}', t - t') \boldsymbol{H}(\boldsymbol{r}', t') \mathrm{d}t' \mathrm{d}^3 r'. \tag{2.4b}$$

Both susceptibilities have the form of second rank tensors in general. For isotropic materials, these tensors reduces to a scalar value implying that the induced electric and magnetic dipoles are aligned parallel or anti parallel to the corresponding external fields. In order to take into account, that most materials only provide a local response, it is not necessary to execute the integration over the entire space $\mathrm{d}^3 r'$. We translate Eq. (2.3a) and Eq (2.3b) from time-, to frequency domain (see section 2.1.3), in the following form:

$$\boldsymbol{D}(\boldsymbol{r}, \omega) = \qquad \epsilon_0 [1 + \chi_{\mathrm{e}}(\omega)] \boldsymbol{E}(\boldsymbol{r}, \omega) = \qquad \epsilon_0 \epsilon(\omega) \boldsymbol{E}(\boldsymbol{r}, \omega), \tag{2.5a}$$

$$\boldsymbol{B}(\boldsymbol{r}, \omega) = \qquad \mu_0 [1 + \chi_{\mathrm{m}}(\omega)] \boldsymbol{H}(\boldsymbol{r}, \omega) = \qquad \mu_0 \mu(\omega) \boldsymbol{H}(\boldsymbol{r}, \omega). \tag{2.5b}$$

The effective material parameters permittivity ϵ and permeability μ describe the linear response of the electromagnetic fields with isotropic and homogeneous materials. These are macroscopic effective parameters including all microscopic charge- and current distributions of the underlying material. In section 2.2.1, we give a simple microscopic model for dielectrics and metals (see section 2.2.2) from which we will derive the effective material parameters. The model describing dielectrics is based on an arrangement of atoms consisting

---

[1] $\epsilon_0 = 8.85 \times 10^{-12} \, F/m$
[2] $\mu_0 = 1.257 \times 10^{-6} \, H/A$
[3] $c_0 = 299792458 \, \mathrm{m/s}$

of a negatively charged electron and the corresponding positively charged atomic core. The model describing the metal properties is based on the concept of a free-electron gas combined with an immobile ionic background and driven by an externally applied electric field. In Eqs. (2.3a) - (2.5b), we discussed the material response on externally applied stimuli. For instance, the electric field $\boldsymbol{E}$ interacts with the medium and induces electric dipoles or influences the already existent electric dipoles within the medium. This leads to a modification of the dielectric displacement $\boldsymbol{D}$. Analagously, the magnetic field $\boldsymbol{H}$ induces or modifies magnetic dipoles, leading to a modification of the magnetic induction $\boldsymbol{B}$. For completeness, it should be noted that generally, an applied electric field might generate magnetic dipole moments and an applied magnetic field leads to electric dipole moments. This can be the case for naturally existant, so-called optically active materials, or artificially designed metamaterials [25, 26]. In the formalism, this leads to cross-coupling terms in Eq. (2.5a) and Eq. (2.5b). Those aspects will be further discussed in section 3.3.1. At this point, we refrain from a deeper treatment, since this aspect does not prevent to understand the following discussed relations given in this context.

2.1.2 Wave Equation

By combining the material equations (2.3a) and (2.3b) with Maxwell's equations (2.1a) - (2.1d), we obtain the inhomogeneous wave equations for the electric and magnetic field [27]

$$\nabla \times \nabla \times \boldsymbol{E} + \mu_0\epsilon_0\frac{\partial^2 \boldsymbol{E}}{\partial t^2} = -\mu_0\frac{\partial}{\partial t}\left(\boldsymbol{j} + \frac{\partial \boldsymbol{P}}{\partial t} + \nabla \times \boldsymbol{M}\right), \qquad (2.6a)$$

$$\nabla \times \nabla \times \boldsymbol{H} + \mu_0\epsilon_0\frac{\partial^2 \boldsymbol{H}}{\partial t^2} = \nabla \times \boldsymbol{j} + \nabla \times \frac{\partial \boldsymbol{P}}{\partial t} - \epsilon_0\frac{\partial^2 \boldsymbol{M}}{\partial t^2}, \qquad (2.6b)$$

where $\boldsymbol{j}$ is the external source current density and $\frac{\partial}{\partial t}\boldsymbol{P}$ and $\nabla \times \boldsymbol{M}$ can be interpreted as polarization and magnetization current density, respectively. These are the source terms of the equations.

This form can be simplified for the case of homogeneous and isotropic media for which $\epsilon, \mu = \mathrm{const.}$ without external currents and charges. Therefore, the wave equations reduce to the form

$$\nabla^2 \boldsymbol{E} + \mu_0\mu\epsilon_0\epsilon\frac{\partial^2 \boldsymbol{E}}{\partial t^2} = 0. \qquad (2.7)$$

This wave equation (2.7) can be solved with an ansatz of the type

$$\boldsymbol{E}(\boldsymbol{r}, t) = \frac{1}{2}\left[\boldsymbol{E}_0\exp\left(\mathrm{i}\boldsymbol{k} \cdot \boldsymbol{r} - \mathrm{i}\omega t\right) + \boldsymbol{E}_0^*\exp\left(-\mathrm{i}\boldsymbol{k} \cdot \boldsymbol{r} + \mathrm{i}\omega t\right)\right]. \qquad (2.8)$$

This form is a representation of plane waves oscillating with the angular frequency ω and propagating in direction of the wave vector $\boldsymbol{k}$. Furthermore, we obtain the dispersion relation by inserting the plane wave solution (2.8) into the wave equation (2.7)

$$\frac{\omega^2}{|\boldsymbol{k}|^2} = \frac{c_0^2}{\epsilon\mu}, \qquad (2.9)$$

and the refractive index

$$n = \pm\sqrt{\epsilon\mu}. \tag{2.10}$$

At this point the question arises, which sign of the square root we have to choose. For natural materials we do not have to care about this fact, because there is no magnetic response at optical frequencies ($\mu = 1$) and therefore we choose the positive sign of Eq. (2.10). This can be motivated by the continuity conditions for the fields at interfaces (see section 2.1.4). For special materials showing also a magnetic response at optical frequencies, e.g. metamaterials (compare chapter 3), this special assumption is no longer valid. We can use a universal formula derived in Ref. [28], using the complex values of the permittivity ϵ and the permeability μ to deduce the right sign, and absolute value of n.

2.1.3   Fourier Transformation

To derive the spectrum $\boldsymbol{E}(\boldsymbol{r}, \omega)$ of a time dependent field $\boldsymbol{E}(\boldsymbol{r}, t)$ and *vice versa*, we have to perform a transformation from $t \rightleftharpoons \omega$. This can be achieved by applying the Fourier transformation for real valued fields, which is defined by

$$\boldsymbol{E}(\boldsymbol{r}, \omega) = \frac{1}{\sqrt{2\pi}} \int_{-\infty}^{\infty} \exp(-\mathrm{i}\omega t)\boldsymbol{E}(\boldsymbol{r}, t)dt, \tag{2.11}$$

and the inverse operation

$$\boldsymbol{E}(\boldsymbol{r}, t) = \frac{1}{\sqrt{2\pi}} \int_{-\infty}^{\infty} \exp(\mathrm{i}\omega t)\boldsymbol{E}(\boldsymbol{r}, \omega)d\omega. \tag{2.12}$$

This very powerful method allows for switching between time- and frequency domain. It is a helpful tool, which facilitates the solving of differential equations. In linear optics, a time dependent electromagnetic field can be written as a linear combination of monochromatic plane waves of the form

$$\boldsymbol{E}(\boldsymbol{r}, t) = \boldsymbol{E}(\boldsymbol{r}, \omega)\exp(\mathrm{i}\omega t). \tag{2.13}$$

By inserting this relation into the homogeneous wave equation (2.7) we obtain

$$\nabla^2 \boldsymbol{E}(\boldsymbol{r}, \omega) - \frac{\omega^2}{c^2}\boldsymbol{E}(\boldsymbol{r}, \omega) = 0, \tag{2.14}$$

by applying the definition of the speed of light in media $c^2 = \frac{1}{\mu_0\mu\epsilon_0\epsilon}$.

2.1.4   Transmittance, Reflectance and Absorption

By assuming an incident plane wave impinging onto a single planar interface formed by two homogeneous and isotropic half spaces with $\mu_1 = 1$, ϵ_1, n_1 and $\mu_2 = 1$, ϵ_2 and n_2, respectively (see Fig. 2.1), we can calculate the reflection and transmittance relations. One part of the wave is back-reflected at the interface to half space one and the other part is
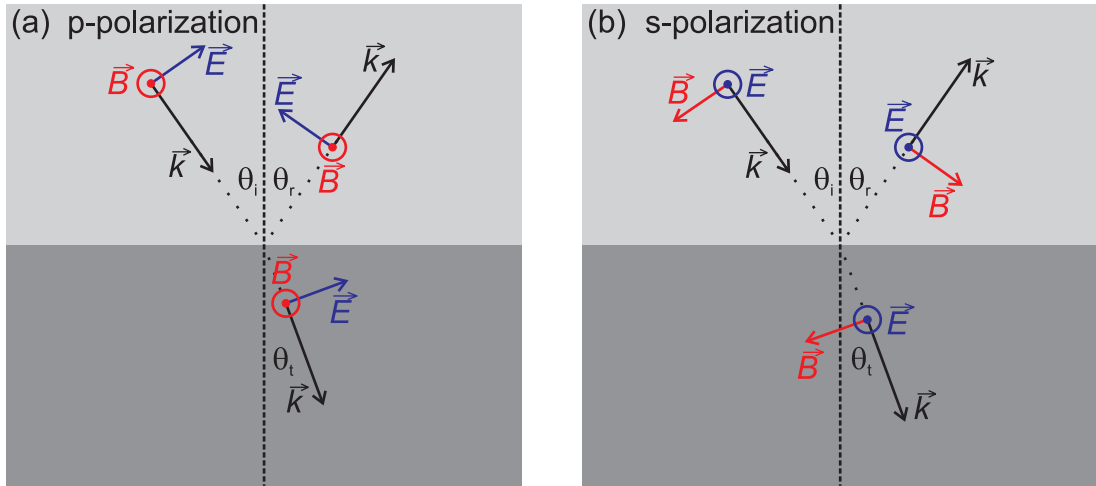
Figure 2.1: Reflection and transmittance of incident p-, and s-polarized light at an interface of two different half spaces of permittivities ϵ_1 and ϵ_2.

transmitted into half space two. The refraction of the transmitted wave can be described by Snell's law

$$\frac{\sin \theta_i}{\sin \theta_t} = \frac{n_2}{n_1}, \tag{2.15}$$

where both angles are defined relative to the surface normal and are given in Fig. 2.1. For deriving the relative intensities that are transmitted and reflected, we describe an arbitrarily polarized incoming wave, as a superposition of two orthogonally polarized plane waves. The superpositions are betoken as s- and p-polarized wave according to Fig. 2.1[4]. These two contributions are defined as a component parallel (p-polarized), and perpendicular (s-polarized) with respect to the incident plane, defined by the wave vector of the incident wave $\boldsymbol{k}_i$ and the normal vector of the interface. We now want to derive the Fresnel equations relating the incident electric fields to the reflected and transmitted electric fields. The Fresnel equations can be derived from the continuity relations at the interface for the $\boldsymbol{E}$- and $\boldsymbol{D}$-field components. We give the results without an exact derivation of this relation which can be found in [24], for instance:

(i) The tangential component of $\boldsymbol{E}$ and the normal component of $\boldsymbol{D}$ are continuous.

(ii) The normal component of $\boldsymbol{E}$ and the tangential component of $\boldsymbol{D}$ are discontinuous.

In addition, the transverse components of the wave vector (in this case, k_x and k_y) are conserved when the wave crosses the interface.
The transmittance and reflectance coefficients, t and r, relate the incident and transmitted or

---

[4]The term "polarization" in this context defines the direction of the electric fields relative to its incidence. This term should not be mixed up with the previous section 2.1.1, where polarization refers to the spatial average over the electric dipole moments.

the incident and reflected fields, respectively. They are defined as [29]

$$r_{\rm s}(k_x, k_y) = \frac{k_{z1} - k_{z2}}{k_{z1} + k_{z2}}, \quad r_{\rm p}(k_x, k_y) = \frac{\epsilon_2 k_{z1} - \epsilon_1 k_{z2}}{\epsilon_2 k_{z1} + \epsilon_1 k_{z2}}, \tag{2.16a}$$

$$t_{\rm s}(k_x, k_y) = \frac{2k_{z1}}{k_{z1} + k_{z2}}, \quad t_{\rm p}(k_x, k_y) = \frac{2\epsilon_2 k_{z1}}{k_{z1} + k_{z2}} \sqrt{\frac{\epsilon_1}{\epsilon_2}}. \tag{2.16b}$$

In addition, these amplitude coefficients are used to extract the intensities T and R of the transmitted and reflected plane waves. These intensities are defined as the time average of the Poynting vector $\langle \boldsymbol{S} \rangle = \frac{1}{2}\mathrm{Re}\,(\boldsymbol{E} \times \boldsymbol{H}^*)$ [5]. For plane waves, this leads to

$$|\langle \boldsymbol{S} \rangle| = \frac{1}{2}\sqrt{\frac{\epsilon_0 \epsilon}{\mu_0 \mu}}\, |\boldsymbol{E}|^2 . \tag{2.17}$$

Therefore, we obtain $T = \frac{n_2 \cos\theta_{\rm t}}{n_1 \cos\theta_{\rm i}}|t|^2$ and $R = |r|^2$.
The absorption within a media, can be understood, by introducing dissipation for the constituting materials. As a result, the refractive index n, becomes complex valued and can be written as

$$\begin{aligned}\tilde{n}(\omega) &= n(\omega) + i\kappa(\omega) \\ &= \sqrt{\epsilon_{\rm Re}(\omega) + i\epsilon_{\rm Im}(\omega)}.\end{aligned} \tag{2.18}$$

The media now becomes dispersive and the relation between the real- and imaginary part is subject to the Kramer's Kronig relation [30].
Next, we consider a plane wave propagating in z-direction of the form

$$E(z, t) = E_0 \exp\left(i\,(\boldsymbol{k}_z z - \omega t)\right) \tag{2.19}$$

with the angular frequency ω and the wave vector $\boldsymbol{k}_z$. The wave vector can be written in terms of a unit vector $\hat{e}_z$

$$\begin{aligned}\boldsymbol{k}_z &= \frac{\omega}{c_0}\tilde{n}\hat{\boldsymbol{e}}_z \\ &= \frac{\omega}{c_0}(n + i\kappa)\hat{\boldsymbol{e}}_z.\end{aligned} \tag{2.20}$$

Using equation (2.18) and (2.20), one obtains

$$E(z, t) = E_0 \underbrace{\exp\left(i\omega\left(\frac{n(\omega)z}{c_0} - t\right)\right)}_{propagation} \cdot \underbrace{\exp\left(-\left(\frac{\omega\kappa(\omega)z}{c_0}\right)\right)}_{dissipation} . \tag{2.21}$$

This equation shows an attenuated propagation of the wave within the media. We know from Eq. (2.17), that $I(z, t) \propto |E(z, t)|^2$ and can herewith link the decreasing part of the intensity

---

[5]Informally, the time average of the Poynting vector $\langle \boldsymbol{S} \rangle$ is usually simply betoken as Poynting vector $\boldsymbol{S}$ For simplicity, we also use this term in following.

with the absorption coefficient $\beta(\omega)$ of Beer's law, describing the exponential decrease in intensity of a wave, propagating through a dispersive media

$$I(z) = I_0 \exp\left(-\beta(\omega)z\right).$$

(2.22)

The absorption coefficient is given by

$$\beta(\omega) = \frac{2\omega\kappa(\omega)}{c},$$

(2.23)

which is directly linked to the skin- or penetration depth by $\delta_z = \frac{1}{\beta(\omega)}$, which describes the length of propagation of a wave within a dispersive media, until its intensity decreases by a factor of e.

2.2 Linear Optics in Solid Continua

In the previous sections we discussed the propagation of light in homogeneous matter. To deduce the characteristic material properties, we need a model taking into account the microscopic properties and transform them into a macroscopic formalism afterwards. This is mandatory, to match the macroscopic description of light interaction with the inherent description of the material parameters.

2.2.1 Optical Properties of Dielectrics

The interaction of electromagnetic waves with dielectric materials can be described classically in the so-called Lorentz model [31, 32]. It is based on the assumption, that an electron which is bound to its corresponding atom core, is externally driven by an oscillating electric field. This is graphically depicted in Figure 2.2. Therfore, we are dealing with the well known problem of a driven and attenuated harmonic oscillator driven by an external force which can be described by the following equation of motion

$$m_e \frac{\partial^2}{\partial t^2}\boldsymbol{x}(t) + m_e\Gamma\frac{\partial}{\partial t}\boldsymbol{x}(t) + m_e\omega_0^2\boldsymbol{x}(t) = -eE_0\exp(-\mathrm{i}\omega t).$$

(2.24)

On the right hand side of the equation we have the external electric field as driving term. The electron mass is given by m_e, Γ describes the damping and e the electron charge. The atom core movement can be neglected because of the big mass difference between the electron and the atom core. The damping Γ can be understood as a composition of the radiative contribution Γ_{rad} and the non-radiative part Γ_{nonrad}, which is due to intrinsic losses, for instance due to electron-phonon interactions. Non-radiative contributions will be further discussed for metals in section 2.2.3. Without a loss of generality, we reduce the dimensionality of the system and assume an electron elongation along the x-axis. We further assume, that the wavelength of the incident stimulus, e.g. a plane wave, is much bigger than the Bohr radius of the electron, which is in very good agreement for optical wavelength. This allows us to assume a spatially constant electric field on each site. The single dipole moment is given by the
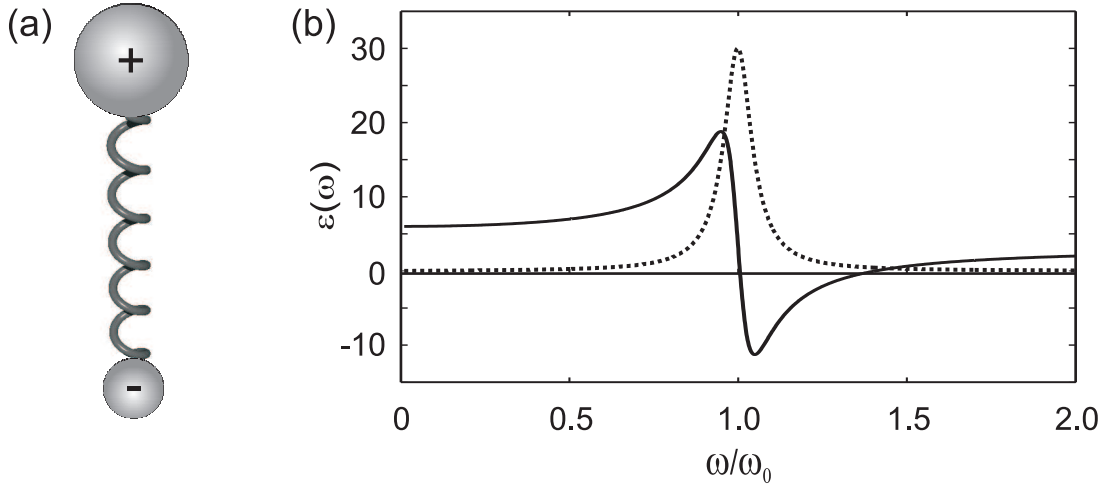
Figure 2.2: In (a), a spring model illustrates the oscillations performed by an electron and its corresponding atom core coupled by the Coulomb force, driven by an external electric field. The plot in (b) shows the real- (solid curve) and imaginary part (dashed curve) of the permittivity $\epsilon(\omega)$ according to Eq. (2.29). The damping parameter is given by $\Gamma = \frac{\omega_0}{10}$.

elementary charge of the electron and its displacement relative to the equilibrium position, which is given by the solution of the equation of motion (2.24)

$$p(t) = -e \cdot x(t) = \left(\frac{e^2}{m_e \left(\omega_0^2 - \omega^2 - \mathrm{i}\Gamma\omega \right)} \right) E_0 \exp(-\mathrm{i}\omega t). \qquad (2.25)$$

Thus, the electric dipole moment is proportional to the electric field. The corresponding proportionality factor $\alpha(\omega)$ is called polarizability and describes the microscopic response to a given external stimulus. It reads

$$\alpha(\omega) = \frac{e^2/m_e}{\omega_0^2 - \omega^2 - \mathrm{i}\Gamma\omega}. \qquad (2.26)$$

One has to keep in mind, however, that we are still in the microscopic picture and the polarizability $\alpha(\omega)$ just describes the response by forming one single dipole. The aim is to find a collective formulation in the macroscopic picture, which will be done in the following.

From Microscopic- to Macroscopic Response

In the previous section we derive a microscopic model, describing the interaction of a single electron and its atom core with an external stimulus, represented by a plane wave. We now want to expand this model to a collective response of all contributing atoms in a material to an external electric field, assuming that there is no interaction between the single dipoles. This leads us from the polarizability $\alpha(\omega)$ of one site in the microscopic- to the electric susceptibility $\chi(\omega)$ and the associated permittivity $\epsilon(\omega)$ in the macroscopic picture.
We again assume a plane wave as external stimulus. Each single dipole excited by the plane wave, re-radiates a spherical wave which superimposes to a plane wave again in the far-field. Therefore, the collective material properties can be described, as a spatial average over all

non-interacting sites, with the polarizability $\alpha(\omega)$. One might think, that the constraint of non-interacting dipoles is an impermissible generalization, which is just valid for a diluted gas and certainly not for a densely packed solid. Nevertheless, this assumption leads to a qualitatively very good approximation for the macroscopic properties of dielectrics in linear optics. Consequently, the macroscopic polarization $P(\boldsymbol{r}, \omega)$, introduced by equation (2.4a) can be written according to the assumptions above

$$P(\omega) = E(\omega) \Big\langle \sum_i \alpha_i(\omega) \delta(\boldsymbol{r} - \boldsymbol{r}_i) \Big\rangle, \tag{2.27}$$

where $\langle ... \rangle$ describes the spatial average, of the dipoles located at position r_i with the polarizability $\alpha_i(\omega)$. Therefore, we receive a macroscopic polarizability $\Lambda(\omega)$, generating the macroscopic polarization

$$P(\omega) = \Lambda(\omega)E(\omega) = \epsilon_0\chi(\omega)E(\omega) = \epsilon_0\left(\epsilon(\omega) - 1\right)E(\omega) \tag{2.28}$$

and the electric susceptibility $\chi(\omega)$ and the permittivity

$$\epsilon(\omega) = 1 + \frac{Ne^2}{m_e\left({\omega_0}^2 - \omega^2 - \mathrm{i}\omega\Gamma\right)}. \tag{2.29}$$

Here, N denotes the electron density, m_e the electron mass, ω_0 the eigenfrequency and Γ the damping. The typical spectral behavior of the permittivity in the Lorentz model is shown in Fig. 2.2 (b).

2.2.2   Linear Optical Properties of Metals

In the previous section, we derived the optical properties of dielectric materials, where the macroscopic properties are well described with a model of non-interacting superimposed oscillators. In the following, we describe the linear optical properties of metals, which can modeled by the movement of electrons in a periodic potential, given by the atom cores and leading to conduction bands where the electrons can move almost undisturbed. This behavior can phenomenologically be described in the so-called Drude model [32, 33]. This classical model describes the typical metallic response in the linear regime. We further discuss possible loss channels, appearing in the model and especially for nanoscale-objects.

Linear Optical Properties of Free-Electron Gases

The optical properties of metals can be well described by the formalism of a free-electron gas. Within this formalism, the electrons in the conduction band follow the applied external electric field and can move almost undisturbed through the crystal structure of the solid. However, the movement is just only nearly undisturbed, because the free electron movement suffers from electron scattering processes with other constituents leading to dissipation. In addition also the electrons in the valence band lead to distributions to the optical response, but these effects can be neglected for the desired frequencies in the first approximation. Therefore, we can use a model, which is similar to the previously discussed Lorentz-oscillator
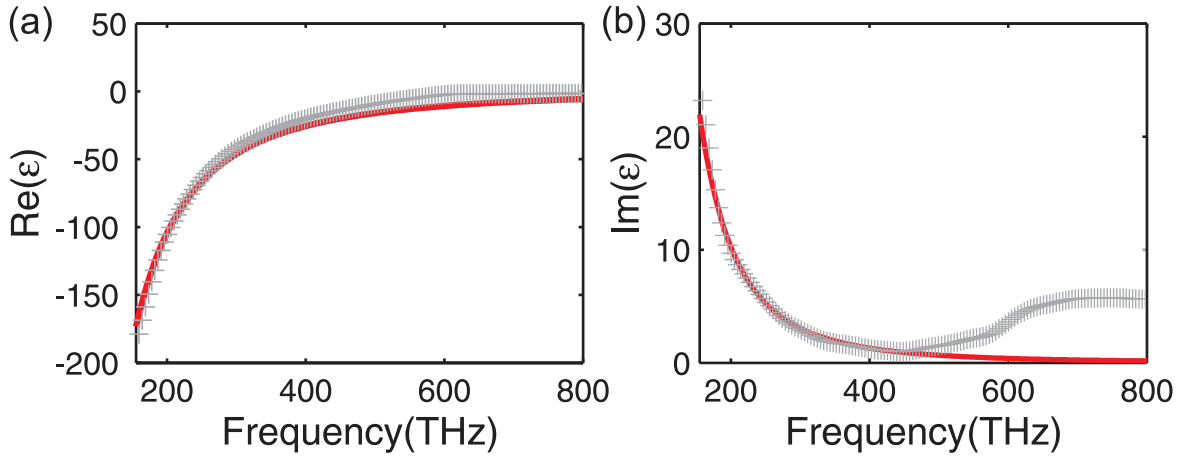
Figure 2.3: In this graph the real- (a) and imaginary part (b) of the permittivity of gold are shown in the spectral interval 150-800 THz. The crosses correspond to experimentally determined data of ϵ from Ref. [16] and the solid red line to a fit of the experimental data to the Drude formula (2.32).

model, but with the crucial difference, that a restoring force for free electrons is obviously missing. Therefore, this system does not oscillate around an equilibrium position, given by the specific atom cores as intrinsic potential. Nevertheless, the electrons follow the direction of the external stimulus, given by the time dependent electric field $E(t) = E_0 \exp(-i\omega t)$. By neglecting the restoring term in in the Lorentz-oscillator model (2.24), we receive an adapted equation of motion for the electron

$$m_e \frac{\partial^2}{\partial t^2} x(t) + m_e \gamma_c \frac{\partial}{\partial t} x(t) = -eE(t), \tag{2.30}$$

where the dissipation or collision frequency is given by γ_c and the driving field $E(t)$. The electron displacement is given by $x(t)$ and can be written as

$$x(t) = \frac{e}{m_0} \frac{1}{\omega \left(\omega + i\gamma_c\right)} E(t). \tag{2.31}$$

Following the derivations of 2.2.1, we receive the permittivity

$$\epsilon(\omega) = 1 - \frac{\omega_{\text{pl}}^2}{\omega^2 + i\gamma_c\omega}, \tag{2.32}$$

where we introduce the free electron density n_e and the plasma frequency $\omega_{\text{pl}} = \sqrt{\frac{n_e e^2}{m_e \epsilon_0}}$. This equation can be adapted, taking into account the dielectric background given by the valence electrons and the corresponding atomic cores, by introducing ϵ_∞. This leads to an offset with respect to Eq. (2.32). We obtain

$$\epsilon(\omega) = \epsilon_\infty - \frac{\omega_{\text{pl}}^2}{\omega^2 + i\gamma_c\omega}. \tag{2.33}$$

Figure 2.3 shows experimental data from Ref. [16] of the real- and imaginary part of the permittivity of gold, plotted over frequency as crosses. These values can nicely be fitted to the

Drude formula given by Eq. (2.32) with the free parameters $\omega_{\mathrm{pl}} = 2\pi \times 2064 \times 10^{12}\,\mathrm{s}^{-1}$ and $\gamma_c = 2\pi \times 19.4 \times 10^{12}\,\mathrm{s}^{-1}$, displayed as solid lines. The presented experimental data are in very good agreement to the Drude model for frequencies below $550\,\mathrm{THz}$. For higher frequencies, there are deviations to the model, caused by interband-transitions in gold [34], where the light leads to excitations of electrons from the valence- to the conduction band[6]. To account for these effects, a more sophisticated modeling has to be done. Due to the fact, that this spectral region plays no significant role in our work, we refer interested readers to [34, 35]. To understand, what happens to an electromagnetic wave at a metallic interface, we assume a plane wave coming from a vacuum- and interacting with a metal half space. Due to the permittivity, we expect a strong reflectance at the interface [compare Eq. (2.16a), (2.16b)]. The transmitted wave propagation is exponentially damped in the metal, due to the strong imaginary part within the wave vector and can be described by Eq. (2.21). The corresponding skin depth $\delta = \frac{c_0}{2\omega\kappa}$ in gold, is about $24\,\mathrm{nm}$ for a frequency of $\omega = 2\pi \times 200 \times 10^{12}\,\mathrm{s}^{-1}$.

2.2.3 Damping in Bulk vs. Thin Metallic Films and Wires

The optical properties of metals are determined by their specific dispersive character. Therefore, the damping plays a major role in this context. By taking into account Eq. (2.30), in general, two main contributions can be classified, based on the Drude model.

- A radiative dissipation, caused by the electron acceleration $\frac{\partial^2}{\partial t^2}x(t)$.

- A intrinsic dissipation, which is related to the drift velocity of the electrons $\frac{\partial}{\partial t}x(t)$ and taken into account within this model, by the collision frequency γ_c.

By considering the intrinsic dissipation only, we solve Eq. (2.30) in the stationary case $\left(\frac{\partial^2}{\partial t^2}x(t) = 0\right)$ and obtain the drift velocity $v_d(t)$ of a single electron. By introducing the electron density n_e we find the stationary current given by

$$j(t) = n_e e v_d(t) = \frac{e^2 n_e \gamma_c}{m_e} \cdot E(t) \tag{2.34}$$

The conductivity, i.e. the ratio between the charge-carrier flux and the stimulus given by the external electric field, is therefore given by

$$\sigma = \frac{j(t)}{E(t)} = \frac{e^2 n_e}{m_e \gamma_c}. \tag{2.35}$$

The "Ohmic" resistivity ρ is defined as $\rho = \frac{1}{\sigma}$. The microscopic dissipation effects, that influence the conductivity of bulk material, are merged together into the phenomenological damping constant γ_c. The contributions to this constant are composed of interaction with

---

[6]Electrons from the $5d$-valence band are excited into the $6s$-conduction band. The required energy is $2.38\,\mathrm{eV}$, corresponding to a frequency of $575\,\mathrm{THz}$.

phonon's, static lattice imperfections (e.g. impurity atoms) and grain boundaries which scatter the conductance electrons due to a localized potential variation, compared to a "perfect" lattice. These contributions can be added according the Matthiesen rule [36]

$$\gamma_c = \gamma_{\text{Phonon}} + \gamma_{\text{Defects}} + ... + \gamma_{...}. \tag{2.36}$$

To get a deeper insight to the damping mechanism leading to the phenomenological value γ_c in the Drude model, we have to focus onto the electron scattering effects within the solid crystal. The characteristic values for these scattering effects are the mean free path l_∞, describing the distance between two scattering events and the corresponding relaxation time τ, giving the time interval between these events.

The insufficiency of properly discussing electron scattering within the drude model, is due to the fact, that we need an adequate velocity distribution of the electrons, which is not inherently given within this model. Obviously, the electrons as fermions follow the Fermi-Dirac distribution. We briefly introduce an extended electron theory (without deriving the following relations), by Sommerfeld [37, 38], which also takes into account the electron-phonon interactions and the right statistics, leading to proper values for the mean free path and the relaxation times.

Let us assume, that only the electrons with energies on the Fermi-sphere $E_f = \hbar^2 k_F{}^2/2m_e$, contribute to the conductance in the ground state. The corresponding momentum of these electrons is then be given by

$$k_F = \left(3\pi^2 n_e\right)^{-\frac{1}{3}}. \tag{2.37}$$

The velocity of the electrons at the Fermi-edge, leading us to the desired expression for the mean free path and the corresponding time, which is given by

$$\nu_F = \frac{\hbar}{m_e} \cdot k_F, \tag{2.38}$$

where $\hbar$ is the Planck constant[7].To give some numbers, for bulk gold [37], we assume a Fermi-vector $k_F = 0.1206\,\text{nm}^{-1}$ and a Fermi-velocity $\nu_F = 1.41 \times 10^6\text{m/s}$. This is a remarkable velocity, showing us that the electrons have about two per cent of the light velocity c_0. In addition, we can assume an external electric field, which only causes a shift of the Fermi-sphere along the momentum vector of the electron flux. The mean free path for bulk material is then given by the relation $l_\infty = \nu_F \tau$, where τ denotes the scattering time. By finding the expression for scattering lengths and times, we can switch back to the Drude conductivity of Eq. (2.35), and find

$$\sigma_\infty = \frac{e^2 n_e l_\infty}{m_e \nu_\infty}. \tag{2.39}$$

By estimating the mean free path of gold bulk material [36, 37], we use a conductivity of $\sigma_{\infty,300\text{K}} = 4.55 \times 10^5 (\Omega\,\text{cm})^{-1}$ at room temperature, an electron density of $n_e = 5.8 \times 10^{22}\text{cm}^{-3}$ and the assumptions above. We receive a mean free path of $l_\infty = 55\,\text{nm}$.

As a consequence of these findings, we have to take into account finite-size effects by downscaling the geometric dimensions comparable to this critical length.

---

[7]$\hbar = 6.582 \cdot 10^{-16}\text{eV s}$
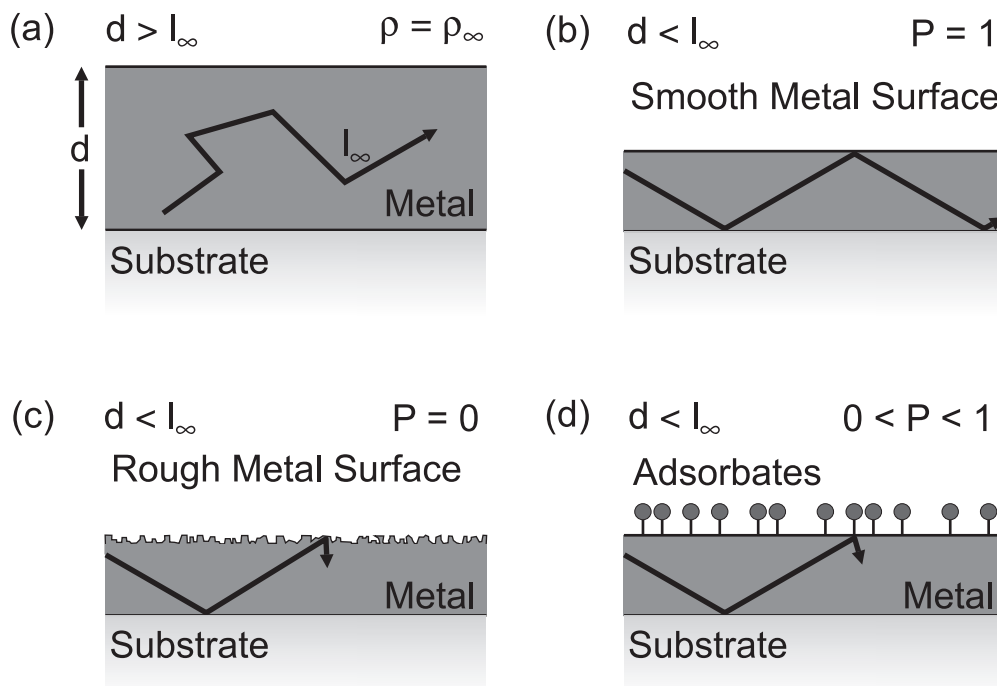
Figure 2.4: In this sketch several metal layer configurations are shown. The parameter P is the so-called specularity parameter describing the scattering probability of the electron at interfaces. Thus, $P = 1$ is the case for elastic- and $P = 0$ for inelastic scattering. In (a) the metallic layer thickness d is bigger than the mean free path l_∞ of the electron in bulk metal. For this setting we do not expect any finite size effects. In (b) the layer thickness is decreased below the characteristic mean free path. The specularity parameter is set to $P = 1$. We expect an influence by the finite size of the thickness and elastic scattering at the boundaries. In (c) the absolute layer thickness is also below the scattering length. In contrast to (b) we only obtain diffusive scattering, due to the corrugated metallic surface. In (d) we find a scattering influence given by adsorbates, covering the metallic surface.

Damping Properties in Thin Metallic Films and Wires

One result, we get from the considerations of the previous section is, that we have to keep in mind finite-size effects by decreasing the geometric dimension of a conductor. For nanoscale-objects this aspect becomes obviously very important. To motivate this influence, we depicted a possible electron trajectory, within a material slab, given in Fig. 2.4 (a).

The scattering characteristics of the electron interacting with the slab boundaries are determined by a phenomenological parameter, the so-called specularity parameter P. For total inelastic-scattering this parameter is given by $P = 0$ and for total elastic scattering we set $P = 1$. This parameter can therefore be used, to model the surface properties and to incorporate surface modifications, i.e. rough metal films, ad-atoms or molecules, adsorbates, or surface alloying, which might influence the electron scattering [compare Fig. 2.4 (b)]. This method is used to frame a theory describing the conductive properties of metallic films and wires, with dimensions smaller than the characteristic scattering length l_∞ in bulk metal [39]. Obviously, this method is limitated to very small slab thicknesses $d \ll l_\infty$. When reaching the regime where the dimensionality of the conductance is reduced, other more sophisticated models have to be taken into account.

To model a thin metallic slab or wire with the scaling parameter d, two simple approximations for the resistivity can be considered, respectively [39]:

$$\text{Slab,} \quad d \gg l_\infty \qquad \frac{\rho}{\rho_\infty} = 1 + \frac{3}{8} \cdot (1 - P) \cdot \frac{l_\infty}{d}, \tag{2.40a}$$

$$\text{Slab,} \quad d \ll l_\infty \qquad \frac{\rho}{\rho_\infty} = \frac{4 \cdot (1 - P)}{3 \cdot (1 + P)} \cdot \frac{l_\infty}{d \cdot \log\left(\frac{l_\infty}{d}\right)}, \tag{2.40b}$$

$$\text{Wire,} \quad d \gg l_\infty \qquad \frac{\rho}{\rho_\infty} = 1 + \frac{3}{4} \cdot (1 - P) \cdot \frac{l_\infty}{d}, \tag{2.40c}$$

$$\text{Wire,} \quad d \ll l_\infty \qquad \frac{\rho}{\rho_\infty} = \frac{(1 - P)}{(1 + P)} \cdot \frac{l_\infty}{d}. \tag{2.40d}$$

By assuming totally diffusive surface scattering $P = 0$ the length scale dependent contributions in Eqs. (2.40a-2.40d) maximizes. For $P = 1$, i.e. perfect scattering at the interface, Eq.2.40a and Eq.2.40c reduce to the expression $\rho = \rho_\infty$. Simultaneously, Eq. 2.40b and Eq. 2.40d are zero. This is necessary, because for perfect surface scattering we would of course expect a bulk conductivity, described within the regime $d \gg l_\infty$. From a practical point of view, a perfect surface scattering for length scales below the scattering length is a constructed case, which is not expectable in real metallic films of thicknesses comparable to the mean free path of electrons in metals.

The equations are plotted for slabs Fig. 2.5 (a) and wires Fig. 2.5 (b). The graphs are plotted for different size regimes given by $d \ll l_\infty$ for the left column and $d \gg l_\infty$ for the right column. The depicted red and black graphs display the different specularity parameters $P = 0$ and $P = 0.5$, respectively. The relative damping increases for decreasing film thicknesses and wire diameters. According to the discussions about the mean free path, these results seems to be expectable. The specularity parameter scales the scattering efficiency at the boundaries. Therfore, for total inelastic scattering we get an increased damping as well. To describe the specularity parameter P analytically, we have to consider the surface effects in a quantum mechanical framework. This has been done in [40], where also surface corrugation effects have been taken into account. This is performed by introducing a short scale roughness and a long scale corrugation length, which determines the effective scattering efficiency of an electron at an interface. For a more detailed description, we kindly refer the interested reader to this illustrative article [40].

Another remarkable result, is the difference in resistivity scaling of metal slabs and wires. By confining the metal in one dimension, meaning decreasing one dimension of the slab and changeover to a wire, we decrease the effective scattering length and increase the scattering probability at the surface. This obviously causes higher resistivity for wires compared to slabs for equal scaling parameters d. This could be a reason why the effective damping parameters assumed for nanoscale objects, which can be composed as an arrangement of wires [3], usually differs from the optical parameters deduced from thin metal films [16].
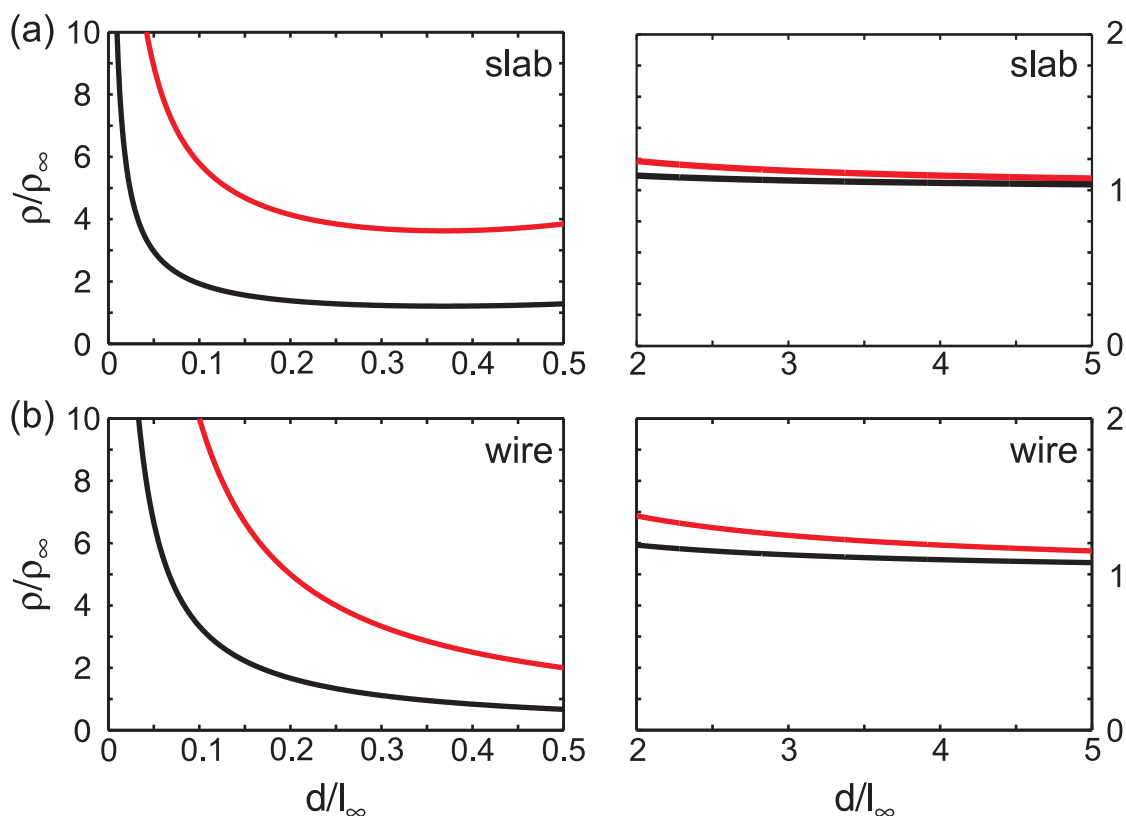
Figure 2.5: In graph (a) the relative resistivity changes are plotted over the relative changes in material thickness for a thin metal slab in the left and a thick metal slab in the right column. The used equations are given by Eqs. (2.40b), (2.40d) for left- and Eqs. (2.40a), (2.40c) for the right column. In addition, two different specularity parameters $P = 0$ (red) and $P = 0.5$ (black) are depicted for ech sub-panel. The crucial scaling parameter is the mean free path l_∞. Plot (b) shows the same relation as (a) but for a thin wire, according to Eq. (2.40c) and (2.40d).

2.3 Wave Excitation in Nano-Scale Objects

In this section, we describe the possibility to externally excite electromagnetic waves traveling along metal-dielectric interfaces - so-called surface plasmon polaritons - and collective charge density oscillations inside a metallic particle, leading to so-called particle plasmons. These effects are cornerstones in understanding the optical properties of effective materials, by deducing the physics of the constituting single elements.

2.3.1 Surface Waves

Surface waves at metal dielectric interfaces, also known as surface plasmon polaritons, are electromagnetic waves confined evanescently along the surface normal and traveling along the materials interfaces. The surface plasmon polaritons are launched by the interaction of an external electro-magnetic field with the free electron gas of a metal. Along these lines, we discuss the wave equation of the surface plasmon polariton and deduce the dispersion relation of these surface waves.

The waveguide confining the surface plasmon polariton is given by a metal- and a dielectric interface. For simplicity reasons, we chose $\epsilon_\uparrow = 1$ for the dielectric half space and $\epsilon_\downarrow = \epsilon(\omega)$ for the metallic half space. The underlying setup is sketched in Fig. 2.6 (a). We want to find eigenmodes of the wave equation, because we are searching for surface waves also existent without the presence of a permanent external stimulus. To find them, we have to solve the homogeneous wave equation [27]

$$\nabla \times \nabla \times \boldsymbol{E}(\boldsymbol{r}, \omega) - \frac{\omega^2}{c_0^2} \epsilon_{\uparrow\downarrow}(\boldsymbol{r}, \omega) \boldsymbol{E}(\boldsymbol{r}, \omega) = 0, \tag{2.41}$$

with the following constraints:

$$\epsilon_{\uparrow\downarrow}(\boldsymbol{r}, \omega) = \epsilon_\downarrow(\omega) = \epsilon(\omega) \quad \forall \quad z < 0 \quad \wedge \quad \epsilon_{\uparrow\downarrow}(\boldsymbol{r}, \omega) = \epsilon_\uparrow(\omega) = 1 \quad \forall \quad z > 0. \tag{2.42}$$

By solving the equation for waves in the xy-plane, we find that only p-polarized waves are propagating solutions, whose z-component of the electric field decays evanescently. For a surface plasmon polariton traveling along the interface in x-direction, the corresponding dispersion relation is given by [27]

$$k_x^2 = \frac{\epsilon(\omega)}{\epsilon(\omega) + 1} \frac{\omega^2}{c_0^2}. \tag{2.43}$$

It is plotted in Fig. 2.6. For the z-component of the wave vector in the lower half space, we find

$$k_z^2 = \frac{\epsilon(\omega)^2}{\epsilon(\omega) + 1} \frac{\omega^2}{c_0^2}, \tag{2.44}$$

and for the upper one

$$k_z^2 = \frac{1}{\epsilon(\omega) + 1} \frac{\omega^2}{c_0^2}. \tag{2.45}$$

By regarding the dispersion relations we can derive constraints for the permittivities $\epsilon_\uparrow(\omega)$ and $\epsilon_\downarrow(\omega)$ assuming, that we have a traveling wave in x-direction. For simplicity, we only consider real values of $\epsilon_{\uparrow\downarrow}(\omega)$. This does not influence the generality of the assumption, because we still receive real, as well as imaginary numbers for k_x. Since we are aiming for traveling waves, we neglect the imaginary values of k_x, which decay over space. Additionally, surface plasmon polaritons are confined in the xy-plane. Thus, in both half spaces, the z-component of the wave vector must be imaginary, this is mandatory to ensure an only planar propagation. Both constraints (k_x is real and k_z is imaginary) are only fulfilled if [compare Eqs. (2.43), (2.44) and (2.45)]

$$\epsilon(\omega) + 1 \; < \; 0 \quad \wedge \quad \epsilon(\omega) \; < \; 0. \tag{2.46}$$

In a broad spectral range, these conditions are only fulfilled for a metal-dielectric waveguide.

For a Drude metal with $\omega_{\mathrm{pl}} = 2\pi \times 2064 \times 10^{12}\,\mathrm{s}^{-1}$ and $\gamma = 0$, we obtain the surface plasmon polariton dispersion relation shown in Fig. 2.6 as solid line. The dashed line is the free-space
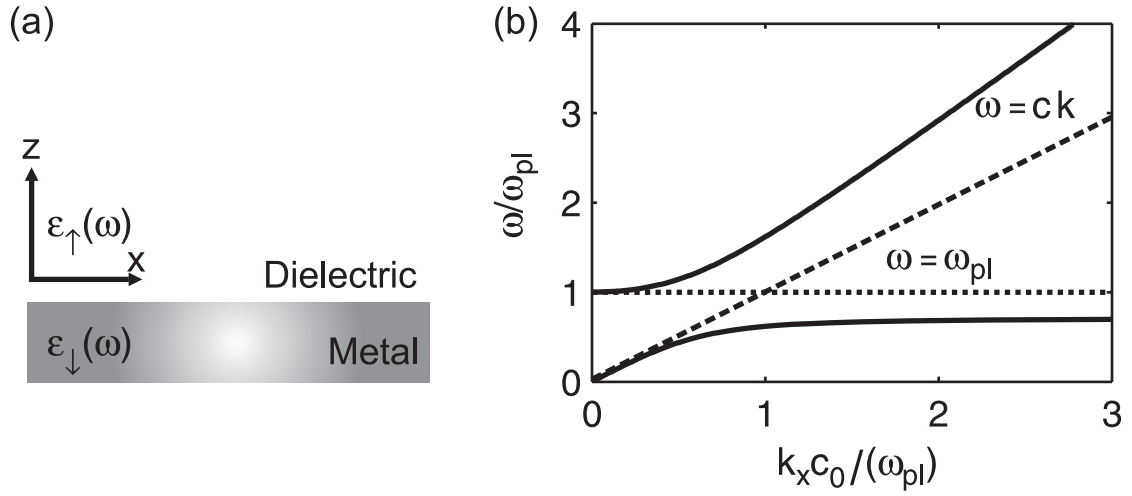
Figure 2.6: In (a), a typical waveguide geometry for a surface plasmon polariton is depicted. The materials permittivity is given by $\epsilon_\uparrow$ for the dielectric- and $\epsilon_\downarrow$ for the metallic half space. In (b) three different dispersion relations are depicted. The solid lines represent the dispersion relation for a surface plasmon polariton traveling along a metal-vacuum interface. The dashed line displays the light line, given by the free-space dispersion of electromagnetic waves. The dotted line corresponds to the dispersion relation of a bulk plasmon.

dispersion $\omega = ck$ of electromagnetic waves in vacuum and the dotted horizontal line corresponds to the bulk plasmon, which is the collective oscillation of the free electron gas. The shape of the surface plasmon polariton dispersion curve, is due to the strong coupling between the light field and the conduction electrons, leading to spreading branches [41].
The lower branch converges to $\omega = \omega_{\mathrm{pl}}/\sqrt{2}$. It lies below the free space dispersion curve for all frequencies. It follows, that due to the momentum mismatch, these modes can not couple to free space and *vice versa*. Thus, we need technical appliances, to bypass the free space momentum mismatch and excite surface plasmon polaritons [42]. One strategy is the excitation of surface waves, by using a prism-coupling setup, based on the method of attenuated total internal reflection, proposed by Otto [43] and Kretschmann [44]. Another strategy is using an electron beam as stimulus. For this method, we have the possibility to efficiently excite surface plasmon polaritons, without the obstacles occurring by the photonic excitation, due to momentum mismatch [45]. It is also shown in Fig. 2.6 that the frequency of the lower branch dispersion relation of the surface plasmon polariton is limited, whereas the wave vector $k_x = 2\pi/\lambda$ is not. As a consequence of this findings, the wavelength can approach arbitrarily small values. For real metal-dielectric systems, these modes are attenuated and will be strongly decreased after a short propagation length [42].
The upper branch of the dispersion relation of surface plasmon polariton lies above the light line. Thus, these excitations can couple to the light filed. In this region ($\omega > \omega_{\mathrm{pl}}$), the metal behaves like an ordinary dielectric.

2.3.2   Particle Plasmons

In the previous section, we discussed the excitation of a surface plasmon polariton in a two dimensional metallic slab as an eigenmode of the wave equation. By reducing the dimensionality of this slab, then forming a metallic finite elongated particle, it is also possible to find excitation, due to an external electromagnetic stimulus. These excitations, are denoted as particle plasmons, which can be described as a collective oscillation of the free-electron gas being confined to the volume of the particle. Many investigations have been done for different geometries, e.g. spheres, ellipsoids [46], cubes [47], shells [48, 49] and the fundamental building blocks of metamaterials like split-ring resonators [3, 50].

The interaction of light with a small particle can be well described within the so-called quasi static approximation, as long as the particle size is small compared to the wavelength of the exciting field ($d \ll \lambda$). In this regime, the spatial phase variation of the harmonic oscillating electric field is negligible and can assumed to be constant over the considered range.
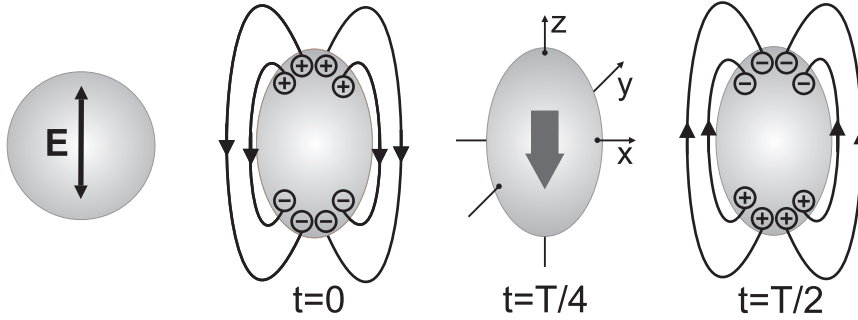
Figure 2.7: Illustration of a particle plasmon excited by an oscillating external electric field. The four pictures describe a spherical as well as three snap shots of an ellipsoidal particle. The snap shots represent three points in time, where we have a formed dipole with a full elongation of the electron gas (t=0, T=T/2) and the compensation current (t=T/4).

As a macroscopic analogon for a one dimensional elongated electron gas, we can use the picture of an antenna in first approximation. The incident electric field $\boldsymbol{E}_0$ drives the electron gas along the antenna axis and forms a dipole. The dipole moment is related to an opposing field, which causes a restoring force for the charge carriers. The system starts to oscillate and forms a harmonic oscillator driven by an external force, which can be described within the already discussed Lorentz model 2.2.1. By assuming a spherical shaped particle, we obtain the polarizability α given by [41]

$$\alpha = 4\pi\epsilon_0 R^3 \frac{\epsilon - \epsilon_m}{\epsilon + 2\epsilon_m}, \tag{2.47}$$

with the sphere radius R, the permittivity of the surrounding medium ϵ_m and ϵ the permittivity of the sphere material. The dipole moment of the sphere is given by $p = \epsilon_m \alpha E_0$. For real valued ϵ, we reach the resonance conditions, when the absolute value of the denominator $|\epsilon + 2\epsilon_m|$ becomes minimal. As a consequence of these findings, the polarizability and with it the polarization are maximized.

The principle of the quasi-static approximation can also be expanded onto different shapes

and geometries. One example which can also be completely analytically described within this formalism, is an ellipsoidal particle. By transforming on principal axes, we find that we have for each elongation direction a separate polarizability. Therfore, the polarization can be described by a tensor of the form [51]

$$
\begin{pmatrix} p_x \\ p_y \\ p_z \end{pmatrix} = \epsilon_m \begin{pmatrix} \alpha_1 & 0 & 0 \\ 0 & \alpha_2 & 0 \\ 0 & 0 & \alpha_3 \end{pmatrix} \begin{pmatrix} E_{0,x} \\ E_{0,y} \\ E_{0,z} \end{pmatrix}. \tag{2.48}
$$

For the elements of the polarization tensor, we obtain [41]

$$
\alpha_i = \frac{4}{3}\pi\epsilon_0 V_{\text{ellipsoid}} \frac{\epsilon - \epsilon_m}{\epsilon_m + (\epsilon - \epsilon_m)L_i}. \tag{2.49}
$$

Where L_i, with $i = 1, 2, 3$ describes the normalized geometry parameter ($\sum_i L_i = 1$) and $V_{\text{ellipsoid}}$ the volume of the ellipsoidal particle. From Eq. (2.49), we find, that the resonance conditions are dependent on the material properties given by the permittivities of the materials ϵ and ϵ_m, as well as on the geometry, given by the shape of the particle, which is described by the volume $V_{\text{ellipsoid}}$ and the geometry parameter L_i.

By assuming an electric field, polarized along the z-direction (compare Fig.2.7), we receive a decrease of the resonance frequency by decreasing L_x and L_y, by a constant volume $V_{\text{ellipsoid}}$ of the particle.

Within the quasi-static approximation we are now interested in the optical response given by the metallic particle. A "microscopical" description can be given by the ability of the particles to scatter and absorb light. This is quantified within the scattering and absorption cross-sections, which are connected with the polarizability α_i. They are given according to [51]

$$
C_{\text{scat},i} = \frac{k_j^4}{6\pi} \cdot |\alpha_i| = \frac{8k_j^4\pi}{27} V_{\text{ellipsoid}}^2 \cdot \left| \frac{\epsilon - \epsilon_m}{\epsilon_m + (\epsilon - \epsilon_m)L_i} \right|^2, \tag{2.50}
$$

where k_j denotes the corresponding wave vector to the polarization of the wave in direction of E_i. The related absorption cross-section is given by

$$
C_{\text{abs},i} = k_j \cdot \text{Im}\,[\alpha_i] = \frac{4k_j\pi^2}{9} V_{\text{ellipsoid}} \cdot \text{Im}\left[\frac{\epsilon - \epsilon_m}{\epsilon_m + (\epsilon - \epsilon_m)L_i} \right]. \tag{2.51}
$$

The extinction coefficient, describing all dissipations of the incoming wave. It is given by $C_{\text{ext},i} = C_{\text{scat},i} + C_{\text{abs},i}$.

For the simple case of a sphere with volume V_{Sphere} and a metal dielectric function given by $\epsilon = \epsilon_1 + i\epsilon_2$ this leads to [41]

$$
C_{\text{ext}} = 9\frac{\omega}{c}\epsilon_m^{\frac{3}{2}} V_{\text{Sphere}} \frac{\epsilon_2}{\left(\epsilon_1 + 2\epsilon_m\right)^2 + \epsilon_2^2}. \tag{2.52}
$$

The scaling of the scattering cross-section in general is given by $C_{\text{scat},i} \propto V_{\text{ellipsoid}}^2$, whereas the absorption cross section scales according to $C_{\text{abs},i} \propto V_{\text{ellipsoid}}$. A consequence given by the relations in Eq. (2.50) and (2.51), is a rapidly decreasing scattering contribution to the

extinction $C_{\text{ext},i}$ for decreasing particle dimensions.

All assumptions made above are only valid in the framework of the quasi-static approximation. For particle sizes and wavelength, where the condition ($d \ll \lambda$) is not valid, we are forced to find another description. For spheres, this can be done analytically with the so-called Mie theory [52]. Within this framework, Maxwell's equations are solved for an incident plane wave interacting with a sphere, described by the material permittivity ϵ and the corresponding geometry parameters including the surrounding medium. The scattering- and extinction cross-sections are then given as multipole expansions [51]. Nevertheless, for broad spectral investigations of the scattering properties of arbitrary shaped, ordered and maybe coupled particles, a rigorous numerical calculation is required.

Chapter 3

The Metamaterial Concept

The propagation of light within matter can be well understood within the classical framework given by Maxwell's equations (compare chapter 2.1.1). The effective material properties used within this framework result from averaging the microscopic response of the material constituents, i.e. the atoms that make up the material. Hence, the spatial structure of the single atoms are not taken into account. Due to this assumption, we must demand that the light wave can not resolve the atomic structure. Thus, the relevant wavelengths have to be much larger than the diameters of the atoms.

This concept can be regarded as universally valid, as long as one simultaneously scales the wavelength of light and the spatial dimensions of the building blocks, that make up the material. Along these lines, we can imagine an effective material, consisting of manufactured building blocks complying the above made assumptions. Such a material is denoted as metamaterial. These building blocks are made of natural substances and form the smallest functional unit, a metamaterial consists of. It is not unusual to informally denote these building blocks as "photonic atoms"[1]. As long as the interacting wavelength of light is much larger than the dimensions of the functional building blocks, we can extract the well known effective optical material parameters, i.e. the permittivity ϵ and the permeability μ.

The metamaterial concept gives the opportunity to influence the effective permeability and permittivity of the material by tailoring the properties of the metamaterial building blocks. This can be done for instance by a proper manufacturing of the geometrical structure and the choice of the substances, the functional elements consists of.

This is an astonishing concept, since beside the adjustment of the permittivity ϵ it allows a tailoring of the permeability μ. It is interesting to gain a material with a magnetic response at optical frequencies, since it is unknown for natural materials . The ability to externally control both, the electric as well as the magnetic effective material parameters, paves the way towards materials showing intended optical properties and even unique optical effects not known from natural substances.

Perhaps the most famous phenomenon created in the context of metamaterials is a medium with a negative refractive index [53,54]. This can be achieved by tailoring the building blocks

---

[1]This term has to be taken with a grain of salt, because the "photonic atom" is no atom in the literal sense. This term only emphasizes one property, i.e. the smallest functional element of the effective material.

in a way, that one receives a negative permittivity and permeability in an overlapping spectral range. At this point it has to be noted that a negative refractive index is only sufficient for negative refraction [55]. Negative refraction can also occur in anisotropic materials [56, 57], in crystals with an anomalous dispersion [58, 59] and in thin metal dielectric films due to a negative beam displacement [60].

A material with a negative refractive index opens up many physical implications, i.e. inverse Doppler shifts [61], an anomalous Cerenkov effect [1] and "perfect" imaging provided by planar lenses [12, 62, 63]. In the following chapter, we want to introduce the derivation of the material parameters, provided by the effective medium theory. We present concepts on tuning the electric as well as the magnetic response within an effective material. By doing so, we mainly focus on tuning the magnetic properties of the metamaterial given by the permeability μ. For nature offers a huge variety of substances which cover a wide range of permittivity values. Furthermore, we present a small excerpt of optical effects occurring within metamaterials.

3.1   Optical Properties of Effective Media

The formalism discribed in section 2.1 gives us the effective parameters for a natural material. Along these lines, we want to introduce the derivation of the optical parameters provided by an effective material. Similar to a conventional crystal, we assume a periodically arranged structure of the metamaterial building block elements with the diameter d of the element and the lattice constant a, defining the displacement between the single elements. Within this formalism we have to ensure, that the wavelength of light interacting with the effective material is small compared to the diameters of the building blocks. This claim is necessary to fulfill the dipole approximation. In addition, the lattice constant is chosen such, that no coupling between the single elements occurs. By doing so, we can assign to each single building block element an electric polarizability α_e and a magnetic polarizability α_m, as the "microscopic" response of the associated dipoles to an external stimulus. By introducing the density n of all sites, we obtain the macroscopic polarization

$$P = n\alpha_e E = \epsilon_0 \chi_e E, \tag{3.1}$$

and the permittivity given by $\epsilon = 1 + \chi_e$ (compare section 2.1.1). Equally, we can derive the macroscopic magnetic response by

$$M = n\alpha_m H = \mu_0 \chi_m H, \tag{3.2}$$

where the permeability is given by $\mu = 1 + \chi_m$. The formalism given above is denoted as effective medium theory. Beyond the assumptions made, also inhomogeneous media or materials consisting of coupled building blocks can described within the effective medium theory. However, the derivation of the effective properties is based on more sophisticated methods. For more information about effective medium theory in general, and the retrieval of effective material parameters in particular, we refer the interested reader to [25, 46, 55].

3.2 Charge Density Changes in Metals

The optical properties of metals strongly depend on the density of free charge carriers within the metal. The ability to change the amount of free charge carriers obviously offers the opportunity to change the optical properties. In the following sections, we discuss strategies pursued to achieve charge carrier density changes within an effective material, given by a so-called diluted metal.

3.2.1 Diluted Metal

In section 2.2.2 we discuss the optical properties of metals. In Eq.(2.32) we can see that the permittivity depends on the plasma frequency $\omega_{\mathrm{pl}} = \sqrt{\frac{ne^2}{m_e\epsilon_0}}$, where n denotes the density of free electrons. Obviously, we can alter the optical response of the material by changing the free charge carrier density. This can be performed by intersecting the bulk metal with non metallic inclusions. Therefore, the effective charge carrier density in a unit volume is reduced, and the plasma frequency decreases. Experimentally, this can be realized by dielectric inclusions within a metal, consisting of a compound made of metallic pillars in air [64, 65] or long metallic stripes [50, 62, 66].

For the case of metallic pillars with a circular base of radius r, which are periodically arranged in the base plane with a lattice constant a, the effective plasma frequency, given for a an external electric field polarized along the pillar axis, is given by [64]

$$\omega_{\mathrm{pl}} = \sqrt{\frac{n_{\mathrm{eff}}e^2}{m_{e,\mathrm{eff}}\epsilon_0}}. \tag{3.3}$$

The effective electron density is given by $n_{\mathrm{eff}} = n\frac{\pi r^2}{a^2}$ with the bulk electron density n, which scales the effective metal density within the unit cell. The electron mass is now also an effective parameter, which takes into account the self inductance of the metallic wire. It is given by $m_{e,\mathrm{eff}} = \frac{\mu_0}{2\pi}a^2e^2n_{\mathrm{eff}}\ln\left(\frac{a}{r}\right)$.

Thus, the effective dilution of metals allows to tune the plasma frequency over a wide spectral range. The conception presented gives the opportunity to adjust the value of the effective permittivity for a given frequency.

This phenomenon only occurs for a specific polarization state of the excitation stimulus, which can simply be understood by a geometrical consideration of the unit cell, the effective medium is based on. Taking for instance the pillar geometry [64], one can simply imagine that the effective dilution phenomenon only occurs for an external electric field, oriented along the pillars axes. For the perpendicular polarization state an oscillation of the confined electron gas is induced, which is described in section 2.3.2 in the notion of particle plasmons. These effects also occur for similar geometrical assemblies of elongated metallic structures [67, 68].

The variation of the permittivity, described in terms of a diluted metal, is based on an effective reduction of the electron density within the metal. Therefore, this concept only allows to shift the plasma frequency to lower values. Thus, the bulk electron density in metals describes the upper boundary of the tuning range.

To increase the plasma frequency beyond value given for for bulk metals, one must have the ability to change the charge carrier density within the metal. This concept is discussed in terms of an electrochemically induced charge injection, changing the net number of free electrons within the metal [22, 69, 70]. Since the underlaying mechanisms for these effects are given in chapter 4, we discuss the related optical effects at this point as well and refer the interested reader to section 4.3.

3.3 Split-Ring Resonators as Metamaterial Representatives

One of the most widely used representatives of a plasmonic building block is the split-ring resonator. The main reason for this is due to the fact, that one can tune the magnetic response over a broad spectral range. Therefore, it is not unusual to denote the split-ring resonator as "magnetic atom"[2]. A general aspect is the resonance frequency tuning properties, which scales anti proportional to its lateral sizes, with the constraint, that the resonance frequencies are far below its plasma frequency [19, 71, 72]. Historically, this concept has been used for microwave experiments [73–75]. The advances in micro- and nano-structuring make it feasible, to expand the scope of these structures to the infrared and visible spectral-range, by miniaturizing the dimensions of the underlying split-ring resonators. By pointing out a few milestones, we can follow the evolution from resonators with a resonance in the microwave range [65, 74], the terahertz region [76, 77], over the infrared spectral range [3, 78, 79], up to the visible [19].

In the following sections we want to introduce the reader to the concepts being used to describe the optical properties of split-ring resonators. At this point, two coexistent modeling conceptions are used, which are given by the plasmonic picture on the one hand, and a LCR-resonator model on the other hand. In addition, possible excitation geometries and modifications are discussed.

3.3.1 Split-Ring Resonators as Electric Circuits

The split-ring resonator can be described within a LC-circuit model [compare Fig. 3.1 (b)] [80]. Here, the inductance L within the model is given by the ring-wire, representing one single winding of a coil, and the capacitance C, which is formed by the two end facets of the same wire. This system can be excited, where the oscillating current flux induces a magnetic dipole moment perpendicular to the model plane and the accumulated charge carriers causes an electric dipole moment, oriented in plane. The resonance frequency of the LC-resonator is then given by the well known textbook formula [42]

$$\omega_{LC} = \frac{1}{\sqrt{LC}}. \tag{3.4}$$

To adapt this simple model to real conditions of a sub-micron metallic split-ring resonator, occurring dissipation effects have to be taken into account. These loss channels essentially

---

[2]It needs to be reiterated that the word "magnetic atom" is not to be taken too literally.
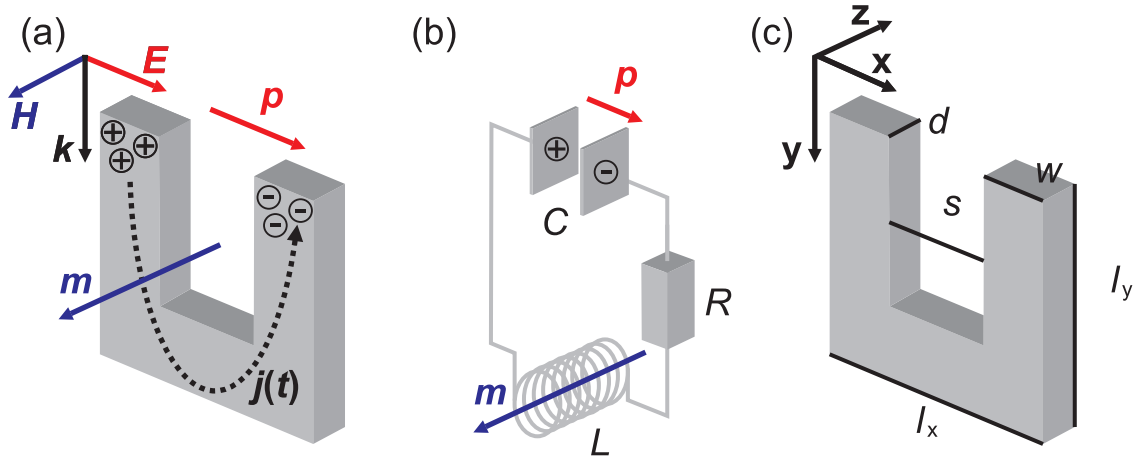
Figure 3.1: In (a) a excited split-ring resonator is depicted. The displaced charge carriers are the source for the dipole moment *p*, and the induced ring-current for the magnetic moment *m*. In (b) the corresponding LCR-circuit model is depicted. Figure (c) shows the split-ring resonator with its geometrical parameters.

consist of material intrinsic Ohmic losses and radiation losses (compare chapter 2.2.3, or [81, 82]). By defining the resistance R, we can therein effectively merge both, the Ohmic- and radiation losses and expand the LC- to a LCR-model.

Therefore, the equation of motion for the charge carriers within a split-ring resonator excited by an external stimulus can be expressed according to Kirchhoff's law. The subsequent discussion follows the derivation given in [25]. Applying Kirchoff's law we receive

$$U_C + U_R + U_L = \frac{1}{C}\int I dt + RI + L\frac{dI}{dt} = U_{\text{ind}}, \tag{3.5}$$

where the electric dipole moment is generated by the charge separation $\int I dt$ and the lateral displacement of the capacitor plates s. We assume a periodic continuation of the single elements with the lateral lattice constant $a_x = a_y = a_{xy}$ and the lattice constant in z-direction a_z. Moreover, we predict a negligible coupling between the single elements. The macroscopic polarization P can be expressed according to the density given by $N_{LCR}/\text{A} = \frac{1}{a_{xy}^2 a_z}$ and the microscopic dipole moment, which in assumptions leads to

$$P_x(t) = \frac{1}{a_{xy}^2 a_z} s \int I dt. \tag{3.6}$$

Similarly, the induced ring current microscopically induces a magnetic dipole moment m, which is defined by the current j and the area penetrated by the magnetic flux $(l_x l_y)$

$$m_z(t) = j(t) l_x l_y. \tag{3.7}$$

Using the oscillator density given above, we get the expression for the macroscopic magnetization

$$M_z(t) = \frac{1}{a_{xy}^2 a_z} j(t) l_x l_y. \tag{3.8}$$

One should point out, that the assumptions made above, take the Ohmic current into account only. This, however, is just valid for small plate distances s, where the displacement current plays a minor role.

By regarding Fig.3.1, we can see two possibilities existing to couple the resonator to the light field (also compare Fig.3.4). In the first case the H-field generates a magnetic flux given by $\Phi(t) = \mu_0 H_z(t) l_x l_y$ which induces the source voltage $U_{\text{ind}} = -\frac{\partial \Phi}{\partial t}$, according to Faraday's induction law. For a magnetic field, given by $H(t) = H_0 \exp(-i\omega t) + c.c.$, we obtain the magnetization

$$M_z(t) = \frac{f\omega^2}{\omega_{LCR}^2 - \omega^2 - i\gamma\omega} H_z, \tag{3.9}$$

where $\gamma = R/L$ with the inductance of a long coil $L = \mu_0 lxly/d$ and the filling fraction given by $f = \frac{l_x l_y d}{a_{xy}^2 a_z}$. The polarization induced by Faraday's law is then given by $P_x = \exp(-i\omega t) + c.c.$ with

$$P_x(t) = \frac{s}{l_x l_y} \frac{if\omega}{\omega_{LCR}^2 - \omega^2 - i\gamma\omega} H_z. \tag{3.10}$$

Here we assumed the capacitance to be $C = \epsilon_0 \text{wt}/d$, which is valid for a capacitor with large plates.

By presuming the electric field to be the external stimulus, we similarly find the source voltage to be $U_{\text{ind}} = E_x(t)d$, with $E_x(t) = E_x \exp(-i\omega t) + c.c.$. The resulting magnetization and polarization are then given by

$$M_z(t) = \frac{s}{\mu_0 l_x l_y} \frac{-if\omega}{\omega_{LCR}^2 - \omega^2 - i\gamma\omega} E_x \tag{3.11}$$

and

$$P_x(t) = \frac{1}{\mu_0} \left(\frac{s}{l_x l_y}\right)^2 \frac{f}{\omega_{LCR}^2 - \omega^2 - i\gamma\omega} E_x. \tag{3.12}$$

Using the material equations from section 2.1.1

$$\boldsymbol{D} = \epsilon_0 \boldsymbol{E} + \boldsymbol{P}, \tag{3.13a}$$

$$\boldsymbol{B} = \mu_0 (\boldsymbol{H} + \boldsymbol{M}) \tag{3.13b}$$

and summarizing the relations given above, we can reduce the statements to the following form

$$\begin{pmatrix} D_x \\ B_y \end{pmatrix} = \begin{pmatrix} \epsilon_0\epsilon & -ic_0^{-1}\zeta \\ +ic_0^{-1}\zeta & \mu_0\mu \end{pmatrix} \begin{pmatrix} E_x \\ H_y \end{pmatrix}. \tag{3.14}$$

Here, we introduced the electric permittivity

$$\epsilon(\omega) = 1 + \left(\frac{sc_0}{l_x l_y}\right)^2 \frac{f}{\omega_{LCR}^2 - \omega^2 - i\gamma\omega}, \tag{3.15}$$

the magnetic permeability

$$\mu(\omega) = 1 + \frac{f\omega^2}{\omega_{LCR}^2 - \omega^2 - i\gamma\omega}, \tag{3.16}$$

and the bi-anisotropy parameter

$$\zeta(\omega) = -\left(\frac{sc_0}{l_x l_y}\right) \frac{f\omega}{\omega_{LCR}^2 - \omega^2 - i\gamma\omega}. \tag{3.17}$$

Considering the relations given above, it can be stated that both, the external electric field $E(t)$ and magnetic field $H(t)$ are source for the polarization and magnetization. The extraordinary character of an effective material consisting of split-ring resonators is given by exhibiting a magnetic response $\mu(\omega)$ even for optical wavelength. This phenomenon is absolutely unusual for natural materials. A further interesting aspect discribes the fact, that one can get a magnetic response by solely coupling the resonator to the electric field (compare Fig. 3.4). This aspect is related to bi-anisotropy and leads to cross coupling terms given in Eq. (3.14). The bi-anisotropy strongly influences the excitation of the oscillator and must be accounted for the retrieval of effective optical parameters. As a result an effective material consisting of split-ring resonators looses its inversion symmetry. For further consequences of the findings described above, we refer the interested reader to [25, 83, 84].

3.3.2 Geometric Variations

Since the invention of the split-ring resonator geometry, several structural modifications have been applied to adapt the optical properties to the experimental needs. In the following we would like to discuss a selection of these modifications, which are depicted in Fig. 3.2 (a)-(e). We start in Fig. 3.2 (a) with the usual split-ring resonator geometry. By increasing the gap size, i.e. the distance between the capacitor plates within the LCR-model [compare Fig. 3.2 (b)], we decrease the capacitance of the resonator and therefore increase its resonance frequency. The configuration shown in Fig. 3.2 (c) is extended to a two slit geometry, which is denoted as cut-wires [85]. In this and the following geometries [compare Fig. 3.2 (b)-(e)] the number of gaps is increased by increments of one. Due to the fact, that the capacities are connected in series, the total capacitance decreases with the number of gaps i given by $C_{\text{tot}} = \left(\sum C_i^{-1}\right)^{-1}$. The decrease in total capacitance C_{tot} leads to further increase in the resonance frequency.

(a)   (b)   (c)   (d)   (e)
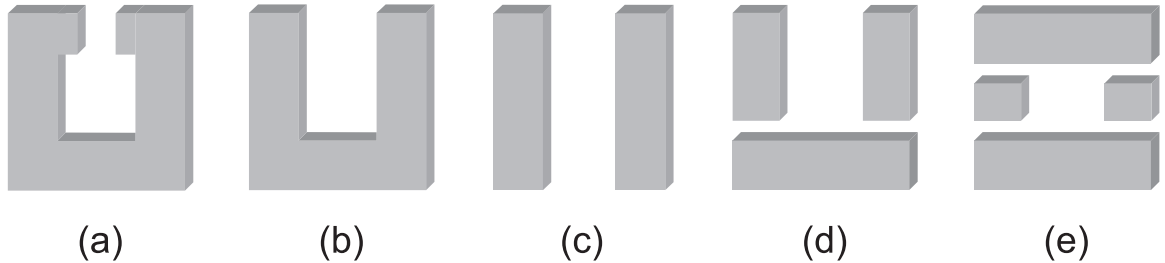
Figure 3.2: In the figures (a)-(e) possible representatives of the split-ring resonator design are depicted. In (a) the typical horse-shoe shaped resonator is shown. It is the classical design consisting of an inductance (wire) and a capacitance (plates between the gap). This can be geometrically varied to a U-shaped (b) or a double wire (c) where an additional capacitance is created. Figure (d) and (e) shows an extension to a structure with three and four capacitive elements.

3.3.3 Split-Ring Resonators as Plasmonic Objects

Another approach to describe the optical effects of plasmonic objects is similar to the discussion of section 2.3.2 and inspired by the geometry of a straight antenna [24]. By applying an external stimulus, which excites the charge carriers within the antenna along the main axis, we receive an oscillating system, where the first three eigenmodes are exemplified in Fig. 3.3 (a)-(c). Deforming the straight antenna by bending up both ends, we obtain the split-ring resonator already discussed. In analogy to the antenna geometry, the corresponding eigenmodes are visualized by the current within the resonators, given as black arrows. The excitation polarizations are depicted by the red arrows in Fig. 3.3. The fundamental mode of the split-ring resonator [Fig. 3.3 (d)] and the second order mode [Fig. 3.3 (f)] are equally excited by a horizontal polarized plane wave, whereas the first order mode of the split-ring resonator is excited by the vertical polarization. Another difference is due to the fact, that the fundamental mode of the split-ring resonator is accompanied by a circular current, which is the source for a pronounced magnetic dipole moment. Hence, this mode is denoted as magnetic mode, whereas the first order- and second order modes are denoted as vertical-electric- and horizontal-electric mode. This is due to their negligible or compared to the first order mode insufficiently pronounced magnetic dipole moment. The denotiation vertical and horizontal correspond to the polarization direction of the incident plane wave. The fundamental excitation of the split-ring resonator exhibits both, an electric- and a magnetic dipole moment. Furthermore, this mode can externally be excited by an electric and a magnetic field. Similar to the antenna, the split-ring geometry also shows a size dependent excitation char-
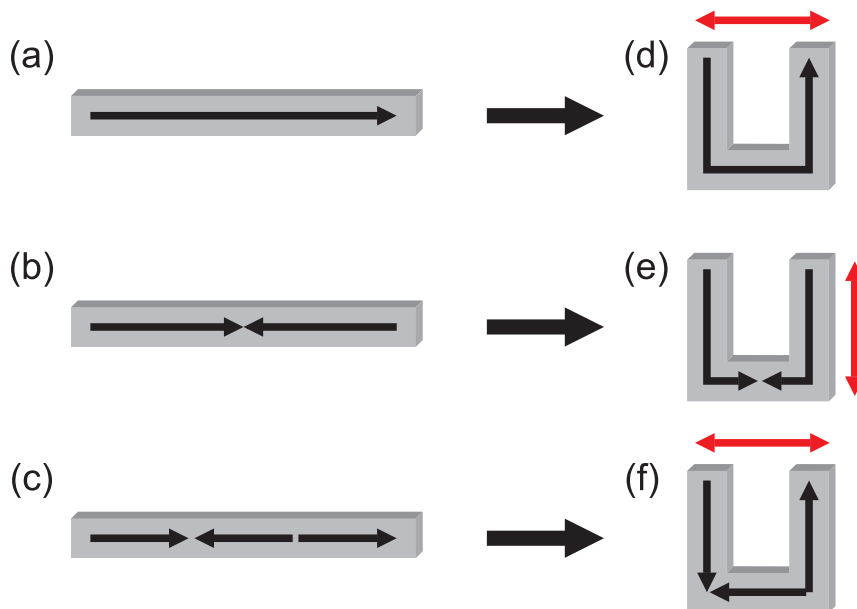
Figure 3.3: In Figure (a)-(c) the first three eigenmodes of an antenna are depicted. The excited currents within these antennae are depicted by the black arrows. By deforming its geometry and bending the antenna ends to a U-shaped "antenna" we end up with the already discussed split-ring geometry (d)-(f), where the corresponding eigenmodes of the system are depicted in analogy to the antennae modes. The corresponding excitation polarizations for the antenna and the split-ring resonator are given by the red arrows.

acter. Moreover, the wavelength of the excitation stimulus is determined by the dimensions of the underlying split-ring resonator, which are given by the lateral dimensions l_x and l_y, the thickness d and the wire width w [compare Fig. 3.1 (c)]. In addition, the excitation is also strongly polarization dependent. By scaling down the given dimension and distinguishing between the magnetic- (i) and the vertical electric mode (ii), we observe the following resonance scaling behavior for the dimensions given above:

(i) Scaling down l_x causes a shift of the magnetic-resonance to shorter wavelength. Whereas, an increase of l_y causes a shift to longer wavelength [86]. Similarly, scaling down the parameters d and w also shifts the magnetic-resonance to longer wavelength.

(ii) The vertical-electric mode can be interpreted in good approximation within the picture of a particle plasmon. Therefore, a decrease of l_y causes a shift to shorter wavelength. In contrast, scaling down l_x, w, and d shifts the vertical-electric resonance to longer wavelengths.

Concerning the underlying parameters, the absolute scaling sensitivity of the resonance differ notably. The most efficient and experimentally easiest way to tune the resonance wavelength is scaling the resonator thickness d. Concerning the experimental work presented in chapter 7 and chapter 8 we do not have this freedom, as we are forced to minimize the resonator thickness d to maximize the intended optical effects. Thus, we focused on scaling the lateral dimension l_x and l_y to shift the resonance wavelength into the regions of interest.

3.3.4 Excitation Geometries

In this section we discuss the different excitation geometries for a split-ring resonator. The term excitation geometry describes the relative orientation of the tricolon given by the wave vector $\boldsymbol{k}$, the electric field $\boldsymbol{E}$ and the magnetic field $\boldsymbol{H}$, relative to the split-ring orientation (compare Fig. 3.4). As already discussed in section 3.3.1 the magnetic-resonance can be excited by both, the electric- $\boldsymbol{E}$ and the magnetic field $\boldsymbol{H}$. Materials with this special characteristics are denoted as bi-anisotropic [25]. A direct coupling by the magnetic field to the split-ring resonators designed for optical frequencies is rather an exception [50]. This is typically due to the huge manufacturing effort being necessary to produce these structure geometries. Therefore, the common excitation geometries are depicted in Fig. 3.4 (a) and (b), where the wave vector $\boldsymbol{k}$ is oriented perpendicular to the resonator plane [3, 79, 87, 88]. For the configuration shown in Fig.3.4 (a) the electric field $\boldsymbol{E}$ couples to the vertical-electric mode of the split-ring resonator (compare section 3.3.3). By orienting the electric field $\boldsymbol{E}$ along the split-ring gap, we couple *via* the capacitance and excite the magnetic-resonance [compare Fig. 3.4 (b)]. For the geometry shown in Fig. 3.4 (c) the magnetic field $\boldsymbol{H}$ directly couples to the magnetic moment of the resonator, and excites the magnetic-mode. A similar excitation geometry can be found in section 3.4.1, where the plate- and wire-pair geometry is briefly discussed [67, 85]. In Fig. 3.4 (d) the configuration is depicted, where the electric- as well as the magnetic field couple to the magnetic mode of the split-ring resonator. It has to be noted, that for the configuration depicted in Fig. 3.4 (c)-(d) retardation effects play
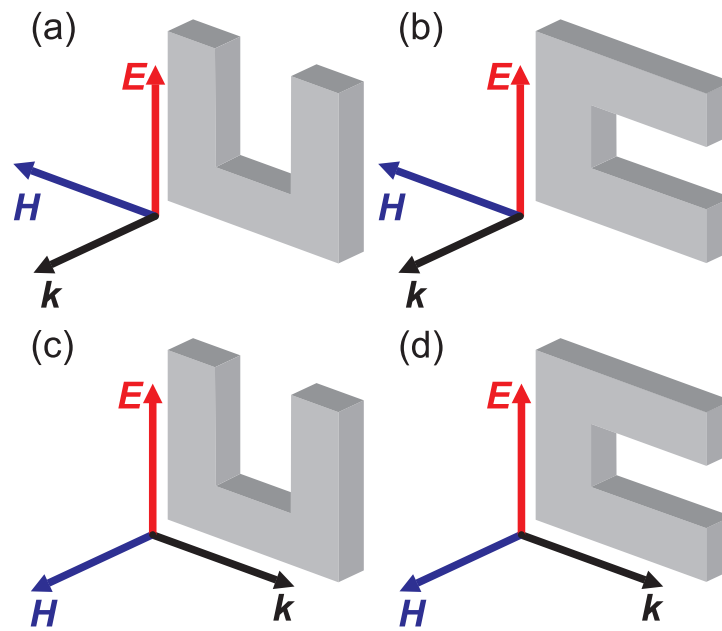
Figure 3.4: In this graph the coupling of the external electromagnetic fields to the split-ring resonator is shown. The incident wave couples to the vertical electric mode of the SRR *via* the electric E field, depicted in (a). (b) shows the orientation where the electric field E is oriented along the gap and couples *via* the capacitance to the magnetic mode. The orientations depicted in (a) and (b) are the common excitation geometries for optical wavelength. In configuration (c) the light travels along the resonators and only the H field couples to the magnetic mode, oriented perpendicular to the resonator plane. Configuration (d) shows the coupling to the magnetic mode by both, the electric field E and the magnetic filed H. As already discussed in section 3.3.1, phase delays of the driving fields have to be taken into account.

an important role. This is already discussed in section 3.3.1 and is due to the fact that both, the external electric- E and magnetic field H drive the oscillator, whereas the polarization P and magnetization fields M are phase delayed relative to their exciting stimulus [25].
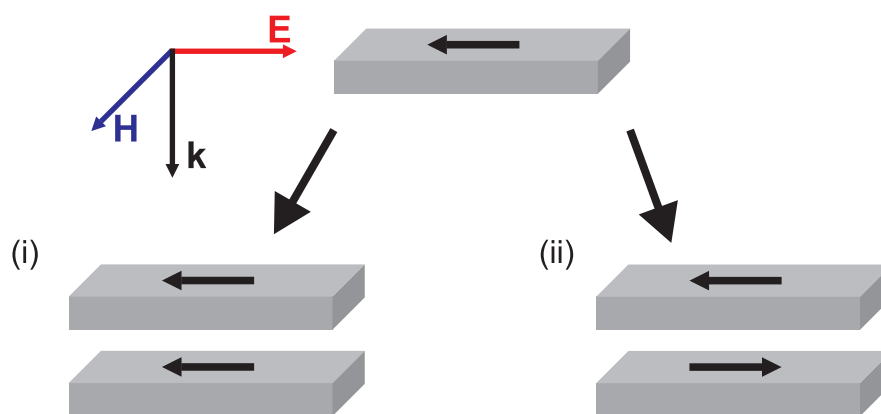
Figure 3.5: By coupling two single wires to a cut-wire pair, we receive a symmetric (i) and an antisymmetric mode (ii). The corresponding currents are visualized by black arrows. The antisymmetric oscillation is similar to the excitation geometry shown in Fig. 3.4 (c) and shows a magnetic dipole moment which leads to an effective permeability $\mu \neq 1$. The incident plane wave is depicted by the vector tricolon.

3.4 Optical Phenomena in Metamaterials

In this section we present a small selection of optical phenomena occurring in photonic metamaterials. The effects presented in the following are mainly related to the extraordinary property of photonic metamaterials allowing to tune the electric permittivity and the magnetic permeability even for optical wavelength of light. This opens up the possibility to create materials with a negative index of refraction.

3.4.1 Creating a Negative Index Metamaterial

In section 3.2.1 we discussed the concept of a diluted metal, allowing the spectral tuning of the electric permittivity. Thus, this method allows to provide a negative permittivity over a broad spectral range.

The cut-wire geometry is a variation of single plasmonic elements which are depicted in Fig. 3.5. Coupling two of these wires, by bringing them in close vicinity, generates two modes, where the currents oscillate in- and out of phase [85]. The in-phase oscillation is denoted as symmetric and the other one as antisymmetric oscillation. Similar to the excitation geometry shown in Fig. 3.4 (c), the cut-wires allow to couple *via* the electric and magnetic fields. Therefore, this structure exhibits a magnetic permeability $\mu \neq 1$.

We now would like to discuss, what we need in order to obtain a negative index of refraction. First of all, the real part of the refractive index $\mathrm{Re}(n) = \mathrm{Re}(\epsilon)\,\mathrm{Im}(\mu) + \mathrm{Im}(\epsilon)\,\mathrm{Re}(\mu) < 0$ has to be negative. Moreover, the material's permeability and permittivity have to fulfill this relation for an overlapping spectral region [55]. At this point it has to be noted, that one receives a negative index of refraction only when the real parts of the permeability and permittivity are negative [28]. This is directly connected to higher losses, which make the case of simultaneous negative real- and imaginary parts of the refractive index more desirable [50].

An experimental realization can be performed by the concept of the diluted metal discussed in section 3.2.1, allowing the spectral tuning of the electric permittivity combined with an
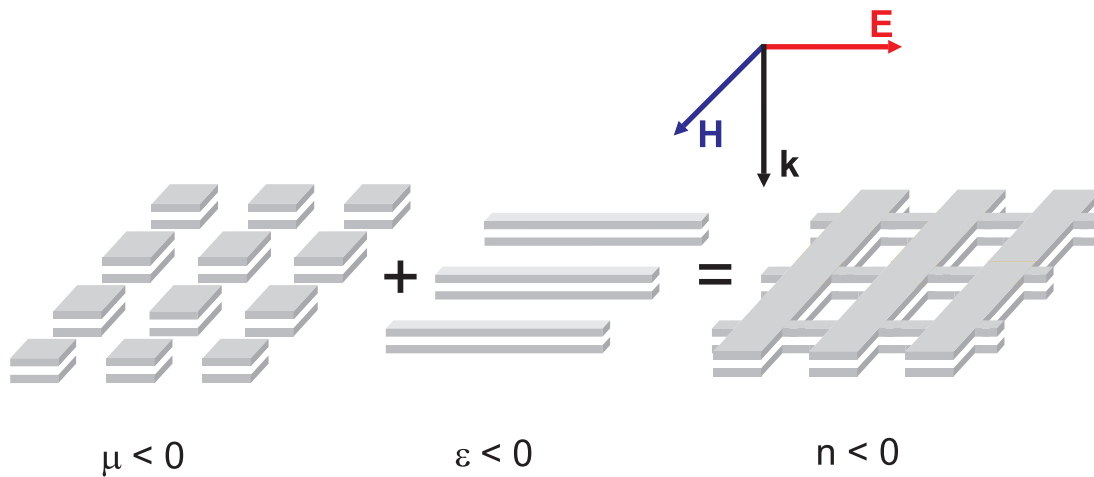
Figure 3.6: In this graph the so-called fishnet structure, providing a negative index of refraction is depicted. It is a compound of cut-wires delivering a negative permeability μ and long metallic wires which act as a diluted metal and provide a negative permittivity ϵ. Combining both, we receive the fishnet. Adapted from Ref. [55].

effective material exhibiting a magnetic dipole moment in the appropriate spectral range. The first functional structure, having both, a negative permeability and permittivity was a composite material. It consists of split-ring resonators and long metallic wires providing a negative index of refraction in the microwave region [65]. In the spirit to achieve this for optical wavelength and the new possibilities provided by micro- and nano-structuring techniques, the concept of cut-wire pairs has been combined with the long metallic stripes. This leads to a new kind of composite structure, providing a negative index of refraction in the infrared region at about 150 THz-frequency [50]. It is due to the net like assembling of this composite, that it is informally denoted as fishnet structure (compare Fig. 3.6). This structure type is composed of cut-wires pairs with an effective negative permeability, delivering a resonance with a quasi-Lorentzian line-shape and long metallic wires, which act as a diluted metal. The optical properties of a diluted metal can well be described within the standard formalism described in section 2.2. Thus, both parameters, i.e. the permeability μ and the permittivity ϵ can be adjusted by scaling the geometrical parameters of the functional elements, the fishnet structure consists of.

This was the starting point for a new stimulus given to the field of metamaterials, leading to radical improvements of fabrication techniques and putting forth the development of negative index metamaterials in the telecommunication spectral range [66] or even in the visible range at $780\,\mathrm{nm}$ wavelength [4]. Further works document, that a periodically stacking of several functional layers does not destroy the effect of negative refraction and therefore paves the way to a three-dimensional photonic metamaterial with negative refractive index [53, 54].

3.4.2 Negative Refraction

In the previous section we presented the fishnet structure providing a negative index of refraction. In the following, we would like to discuss the consequences one preserves from a negative index material in linear optics and therefore extend the discussion of section 2.1.4.
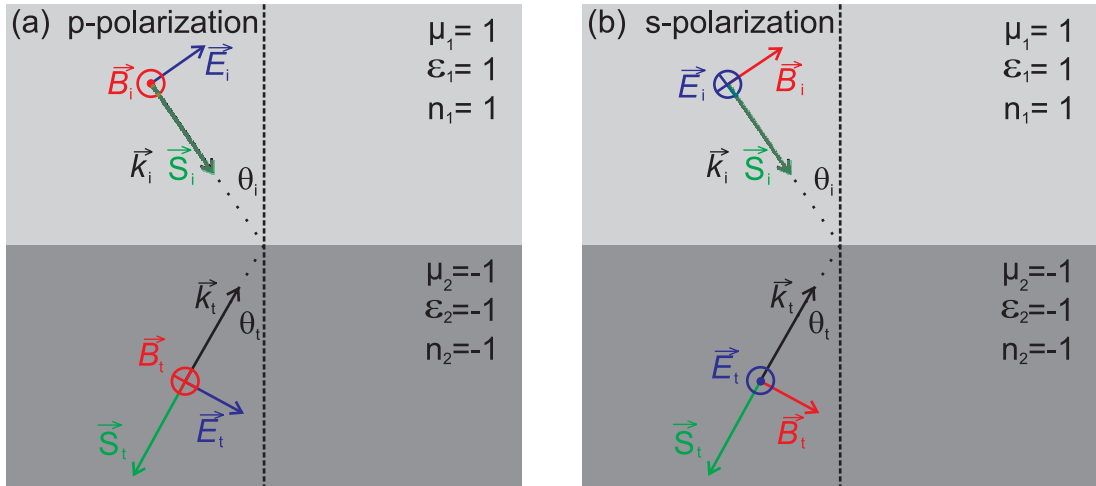
Figure 3.7: In this figure the refraction of a p-polarized- (a) and s-polarized wave (b), at an interface of two half spaces with $\epsilon = \mu = 1$ and $\epsilon = \mu = -1$ is depicted.

In Fig. 3.7 we depicted the situation of a p- (a) and s-polarized beam (b), coming from a vacuum half space and intersecting the half space of a material with negative index of refraction. By investigating this beam coming from the vacuum half space, $\epsilon_1 = \mu_1 = 1$ and impinging onto a surface of the negative index material with $\epsilon_2 = \mu_2 = -1$ under oblique incidence, one makes the curious observation that the light is refracted to the "wrong" side of the surface normal (compare Fig. 3.7). This can immediately be interpreted by Snell's law Eq.(2.15), which shows that the beam obviously is refracted with a negative angle measured relative to the surface normal. In addition the model system depicted in Fig. 3.7, shows no reflection at the surface, which is due to a perfect impedance matching $Z_1 = Z_2$. Therefore, one would only expect surface reflection by a mismatch of the impedance $Z = Z_0\sqrt{\frac{\mu}{\epsilon}}$, with the vacuum impedance $Z_0 = 377\Omega$ (compare Fig. 3.7).

The fields within the different half spaces for p- and (s-) polarization change their sign for the magnetic- and (electric-) or are mirrored at the plane of incidence for electric- and (magnetic) fields. Applying the boundary conditions for $\boldsymbol{E}$- and $\boldsymbol{B}$ fields at an interface between positive-and negative index material accompanied with Maxwell's equations we can extract the wave vector $\boldsymbol{k}$ and the Poynting vector $\boldsymbol{S}$ by

$$\boldsymbol{k} = \omega \boldsymbol{E} \times \boldsymbol{B} \quad \wedge \quad \boldsymbol{S} = \boldsymbol{E} \times \boldsymbol{H}. \tag{3.18}$$

Combining the assumptions made above, it shows that in the negative index material the wave vector $\boldsymbol{k}$ and the Poynting vector $\boldsymbol{S}$ are anti parallel to each other, leading to an astonishing phenomena of so-called backward waves [42], which have been experimentally presented by measuring the phase and group velocities of light in a negative index metamaterial [62].

3.4.3 The Perfect Lens

One curious, "possible" future application incorporating the effect of negative refraction is the perfect lens [1]. It has theoretically been shown by J. B. Pendry that a slab consisting of
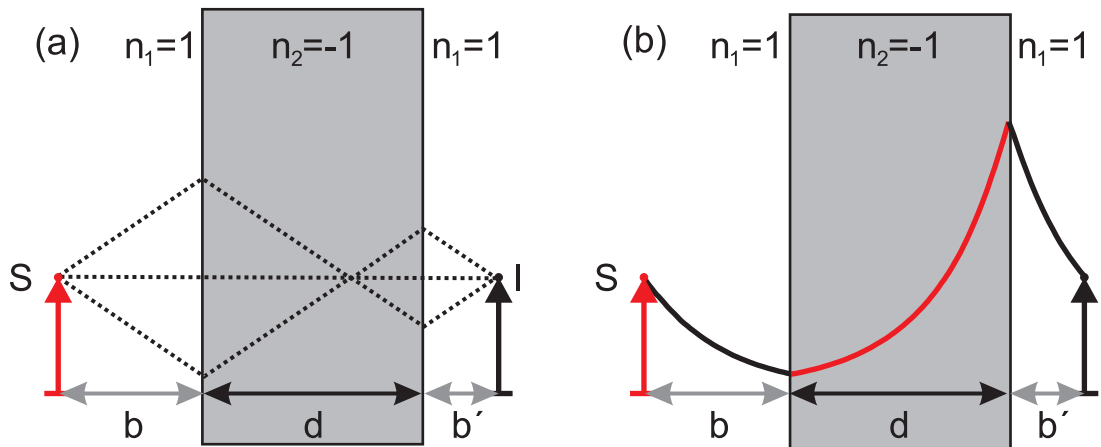
Figure 3.8: (a) A planar lens consisting of a material with $n = -1$, images the light of a point source S on the left hand side of the slab to its Image I on the right hand side. (b) Within this slab the evanescent modes of the image decaying in free space, are exponentially enhanced, which enables sub-wavelength or even perfect imaging [12].

negative index material forming a lens, which enables, under certain circumstances, a perfect image [12]. The setup discussed is graphically depicted in Fig. 3.8 for a material slab with thickness d and refractive index $n = -1$ surrounded by vacuum. Here, a point source is imaged by a slab with refractive index $n = -1$. Similar to conventional lenses, the image I is a reconstruction of the point source S mediated by the real valued wave vector components of light, which is geometrically depicted by the dashed black lines in Fig. 3.8 (a). In contrast to usual lenses, the imaginary valued components of the wave vector $\boldsymbol{k}$, also denoted as evanescent waves, do not vanish along the propagation within the lens. The evanescent modes experience an exponential amplification within the negative index medium and therefore suppress the lack of source information allowing a perfect reconstruction of the source S within the image I [compare Fig. 3.8 (b)].

However, it has to be noted, that the mechanism of perfect imaging is very sensitive to material losses, given by the imaginary part of the refractive index $\mathrm{Im}(n)$. For a real material system this seems to be highly nontrivial, because Kramers-Kronig relation requires $\mathrm{Im}(n) \neq 0$ for $\mathrm{Re}(n) \neq 1$ [89–91]. Even small losses lead to strong influences concerning the imaging behavior [63]. Inspired by this concept, works on sub wavelength resolution have been presented, using either the effect of enhancing evanescent modes by metallic material slabs [13, 92] or so-called hyperbolic lenses, which provide sub wavelength imaging [93, 94].

Chapter 4

Principles of Electrochemistry

Electrochemistry is a field between chemistry and physics connecting chemical reactions directly to a charge transfer within the occurring processes. The reaction partners typically consist of solvated, mobile chemical species and a solid electrode as counterpart. Therefore, the interaction zone can closely be localized to the vicinity of the electrodes surface, where all processes are mediated by charge displacement- or transfer effects. Thus, for most of our investigations, we can focus onto the intermediate region between the electrode and the electrolyte to describe the underlying processes.

The impact of electrochemistry is accompanied by a huge bundle of phenomena, e.g. electrophoresis, catalysis and corrosion. These effects are implemented in devices like batteries, fuel-cells or metal-plating techniques, which already permeated our daily life.

In the following we give a brief overview about surface effects occurring in electrochemical processes as far as those affect the underlying work. This is divided into capacitive- and chemical surface reactions, influencing the electronic structure of the electrode material and surface restructuring effects based on an enhanced electrode material mobility.

4.1   Structure of Metal-Electrolyte Interfaces

The entire investigation of capacitive and chemical reactions in electrochemistry can be simplified described as surface reactions and charge transfer phenomena, which occur at the intermediate region between the electrodes and the electrolyte, forming an electrochemical cell. Typically, this term denotes a system of a transfer medium, which usually consists of a liquid electrolyte phase and at least two electrodes, initiating the charge carrier flux. A simple model gives a surprisingly good phenomenological description of the electrode-, electrolyte interface and can be related to a plate capacitor. The plates of this capacitor are formed by the metal electrode surface with its surface excess charges on one side and the mobile solvated ions on the other side. The medium in between is given by solvated ions, which behave like a dielectric or a plasma, dependent on the external electric field strength. These assumptions form the fundamentals for the following descriptions.

4.1.1   The Double Layer Model

As discussed already, that the intermediate plane of an electrode on the one side and the electrolyte on the other side can be simplified described within a capacitor model suggested by Helmholtz [95, 96]. Therefore, the surface charges of the electrode are screened by the ions solvated in the electrolyte. By assuming the media in between the plates to be dielectric, the properties are given by the well known text book formula for the stored charge density of the plates [97]

$$\sigma = \frac{\epsilon\epsilon_0}{d} \cdot V, \tag{4.1}$$

with the potential difference V and the effective difference d between the plates. The capacitance is determined by

$$C_d = \frac{\partial\sigma}{\partial V} = \frac{\epsilon\epsilon_0}{d}. \tag{4.2}$$

The weak point of this model becomes obvious by regarding Eq. (4.2). The capacitance is assumed to be constant, which is a result of the naive assumption, that the dielectric properties of the intermediate plane ϵ, as well as the effective distance d do not depend on the applied potential and the charge carrier distribution within the media. This insufficiency has been fixed by Gouy and Chapman [98, 99]. They introduced a diffuse layer, consisting of capacitive slices with thickness dx, parallel to the electrode plane. These slices compensate the charge given on the electrode surface and can be understood as a series of capacitors. Therefore, the ionic concentration n_i is determined by a Boltzmann factor, with respect to the bulk concentration n_i^0 and the electrostatic potential Φ. This assumption can be written as [97]

$$n_i = n_i^0 \exp\left(\frac{-z_i e\Phi}{k_B T}\right), \tag{4.3}$$

where e denotes the electron charge, k_B the Boltzmann constant, T the absolute temperature and z_i the charge of the ion. The charge distribution can be expressed by adding the layers according to

$$\rho(x) = \sum_i n_i z_i e. \tag{4.4}$$

By using the charge distribution given by the Boltzmann equation and combining it with the Poisson equation from the electrostatic, we yield the Poisson-Boltzmann equation discribing the potential profile through the capacitor slices.
We present the results for the potential profile, while the derivations can be found in appendix A. This profile exponentially decreases over distance and is given according to the electrode potential Φ_0 and the dissipation constant κ as

$$\Phi = \Phi_0 \cdot \exp(-\kappa x). \tag{4.5}$$

The inverse $1/\kappa$ has the unit of length and is denoted as Debye length. Typical values for the Debye length are a few nm [97]. It decreases for increasing electrolyte concentrations.
The weakness of this theory is given by the assumption of point charge constituents within the electrolyte solution. Therefore, the distance between the electrode surface and the solvated constituents decreases towards zero separation. This really non-realistic assumption is fixed by Stern [100], who introduced a plane of closest approach, which is given by the ionic radii and the surrounding solvation shell. This leads to a linear behavior, for distances smaller than the the characteristic Debeye length scale. The results are depicted in Fig. 4.1 (b). This scale defines the outer Helmholtz plane (OHP), which gives the lowest boundary for unspecifically adsorped species[1] [compare Fig. 4.1 a)].
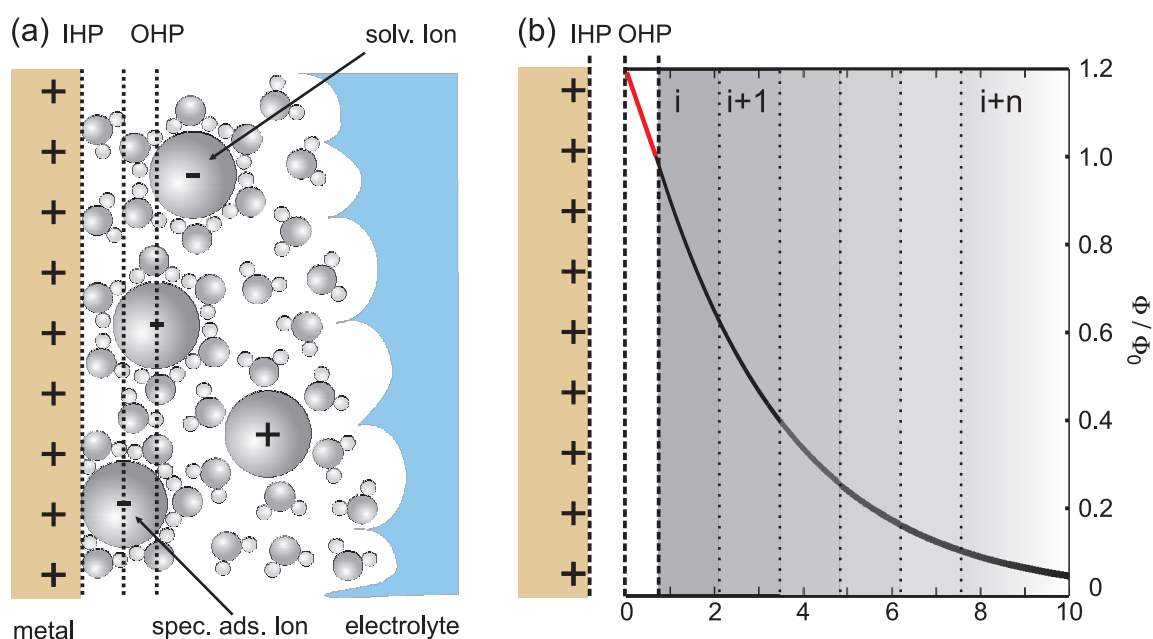
Figure 4.1: In (a), a sketch shows the double layer region, given by the electrode surface and the solvated- or specifically adsorbed ions. The radii of the solvated and the specifically adsorbed ions, defines the outer- and inner Helmholtz plane, respectively. The corresponding potential profile, for unspecifically adsorbed ions only, is given in (b). Where the Stern modification (red) is a continuous extension of the Gouy-Chapman potential profile depicted in black. The single density slices are displayed by the gray shaded areas. The profile with the connected values is adapted from [97], with $\Phi_0 = 100\,\text{mV}$, $1/\kappa = 3.04\,\text{nm}$ and relative dielectric value $\epsilon_r = 78.49$.

4.1.2 Chemical Surface Reactions

Solvated ions, interacting with the electrode surface by electrostatic forces only, are denoted as nonspecifically adsorped. These are usually cations or specific anions, for instance F^- which are strongly bound to their solvation shell. They form the OHP. Other ionic species,

---

[1]The emphasis by using the term "unspecifically adsorbance" is more on "unspecifically" than on "adsorbance". The first term is used to express that the specific chemical properties play no role and the binding caused by long range interactions is described with the term adsorbance.

mostly anions, e.g. Cl^-, Br^-, I^-, tend to partially strip off their solvation shell by increasing the given electrode potential and specifically adsorp at the electrode surface [101]. In general, this happens for positive and for negative potentials (measured relative to a standard reference electrode), dependent on the charge of the constituting ion and the strength of the applied electric field. The specific ion radii then define a new length scale, which is given by the inner Helmholtz plane (IHP) [compare Fig. 4.1 (a)].

For further increasing the potential, oxidation and reduction processes of the ionic species located at the interface appear with an accompanied charge transfer through the interface. These effects are expected at the positive end of region I within the cyclic voltammogram depicted in Fig. 4.2 (a). Furthermore, this process is schematically depicted in Fig. 4.2 (b). These effects are generally classified in faradaic- and non-faradaic processes. The term "faradaic" determines a processes, where the transfered charge carriers are proportional to the number of chemical reactions occurred. All other charge incorporated reactions are denoted as non-faradaic.

To investigate the occurring processes and their reproducibility, one has to explore measurements of the current flux, which give a characteristic fingerprint of the underlying processes. These techniques are discussed in the following section.

4.1.3 Electrochemical Voltammetry

In considering the reactions, occurring within an electrochemical cell, for instance oxidation and reduction processes, ad- and desorption of ionic species, capacitive surface charging and many more, we always have a strong relation to the applied potential, which determines the energy of all charge carrier species involved in the electrochemical processes. To investigate all these different effects, current and voltage measurements are of tremendous interest. Both quantities are well accessible and can be measured with high accuracy. In addition, they give a direct response about the occurring surface reactions. A typical method used for these investigations is the cyclic voltammetry (CV), where the given current between the electrodes is measured as a function of the applied potential, which is varied periodically. An important side aspect of this method is the investigation of the reversibility of the underlaying surface reactions. Such a CV is depicted in Fig. 4.2 (a). In this graph, the potential axis is divided into five different sections, where the occurring processes can be classified by the current characteristics. In section I the so-called oxygen region is depicted. In this interval oxygen evolution takes place and even oxidation processes are possible. These effects are typically incorporated by strong current gradients. Within the subsequent section a broadened increase peak of the current can be observed. This effect is related to the specific adsorption of OH^-. In the third section we see the desorption of OH^- species deposited on the electrode surface. This effect is accompanied with a localized and very strong current gradient. The fourth section displays the so-called double layer region, where the current shows no strong volatility. This is the region where typically nearly no chemical surface reactions takes place. The charge characteristics is given within the GCS capacitor model discussed in section 4.1.1. Section V shows the region of hydrogen evolution which is also accompanied by a strong current gradient. This method directly reveals the existence of irreversible surface reactions.
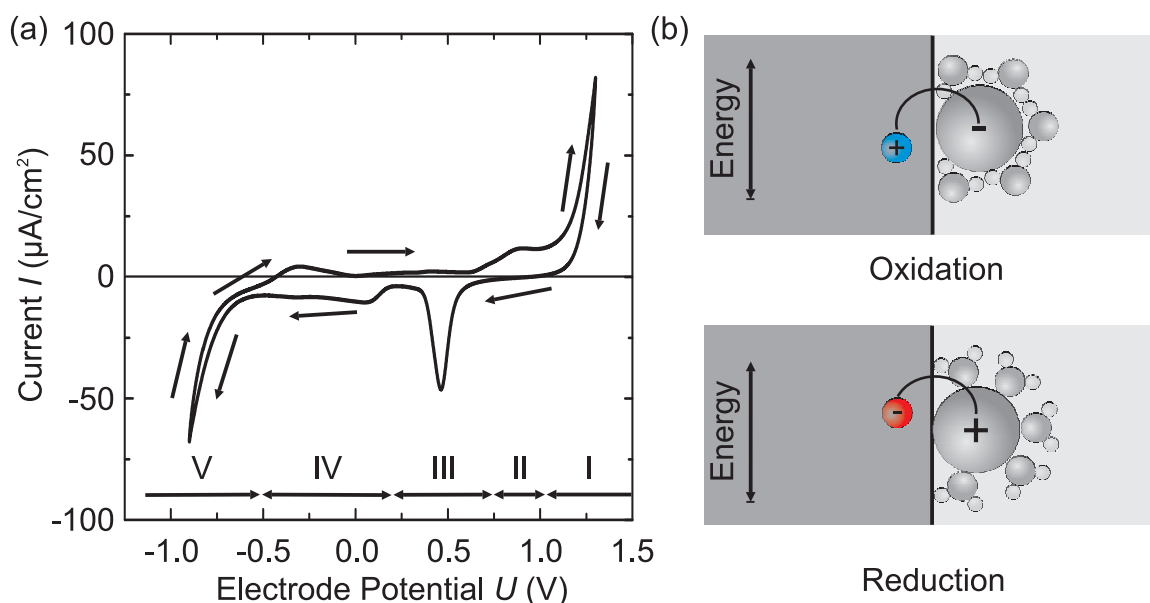
Figure 4.2: In (a), a cyclic voltammogram of a gold foil in 0.7 M solution of NaF is depicted. The used scanning rate is 20mV/s, which is quite low to ensure equilibrium conditions. The applied potential is measured relative to a Ag/AgCl reference electrode (compare section 6.2.1) and is varied in the interval from -0.9 V to 1.3 V. The potential variation is given according to the depicted arrows. Within this cycle five different processes can be distinguished, labeled in roman numbers: I: Shows the so-called oxygen region, where oxygen evolution takes place. In this region and beyond for more positive applied potentials, oxygen formation and adsorption as well as oxidation processes becomes possible. II: Shows the the region of OH^- adsorption. III: The region of OH^- desorption is depicted, accompanied with a locally strong increased current gradient. IV: In this potential interval nearly no chemical reaction takes place. It is the region, which can be well described within the GCS capacitor model, where we see the charge and discharge of the capacitor. Therefore, no charge transfer through the interface region occurs. V: In this potential region hydrogen evolution is generated [102, 103]. (b) depicts a schematic sketch of oxidation and reduction processes within the interaction zone.

This can nicely be investigated by non-matching graphs for different cycles (not shown). The defect structure of the metal electrode surfaces is of extraordinary importance. Therefore, a lot of effort is spent in order to create single crystal electrodes to reduce these deviations. For special purposes these charge induced surface modification effects are warmly appreciated, as they give the ability to improve the quality of metal surfaces. These effects and its mechanisms are briefly discussed in the following.

4.2 Surface Modifications

To determine specific surface reactions in reproducible measurements, the availability of well defined and defect free electrode surfaces are of tremendous importance. In the past this had been guaranteed by the use of mercury liquid metal electrodes, which perform a nearly perfect electrode surface [101]. As nowadays noble metals can be treated under ultra high vacuum conditions (UHV), this method loses its importance. Nevertheless, well controlled and reproducible surface treatment techniques, are very important to post process metallic

films, to generate surfaces with low defect rates and a high lattice symmetries. Several techniques are used to produce the surfaces conditions described, while three of them are discussed in the following.

4.2.1   Electrochemical Restructuring of Surfaces

The reconstruction of surfaces is usually connected to a lateral displacement of atoms, which occurs in the top surface layer. The surface kinetics of this atoms can be influenced by modifying the lattice binding energies, which are dependent on a spatial potential variation at the surface. This mechanism is denoted as potential-induced reconstruction and typically occurs for a negative surface charging, preferred in lattice defect rich areas of unreconstructed metal electrodes [104, 105]. For gold, the untreated surface is in a metastable state, where the reconstruction mechanism is suppressed for room temperatures by an activation barrier. By negatively charging the surface, this barrier can be lowered, which leads to reconstruction kinetics of the surface atoms even at room temperatures [104]. This effects can well be modeled within theoretical ab initio studies, taking into account the dipole moment of the defects and the surface charge densities induced by an external electric potential [106].

Another mechanism, which enhances the mobility of atoms at noble metal surfaces, is connected to a selective adsorption of ionic species. Several works show an enhanced mobility at corrugated steps at gold surfaces, induced by specifically adsorbed anions [107, 108]. These effects increase for increasing applied electrode potentials. The mobility activation also depends on the strength of the gold anion interaction, which is given for selected anions according to, $F^- < Cl^- < Br^- < I^-$ [101]. The restoring of electrode maltreatments and defects of noble electrode surfaces in solution, is a common technique [109, 110]. The underlying mechanisms are mainly based on the discussed anion-enhanced surface mobility and are usually denoted as electrochemical annealing or electrochemical reconstruction [101, 106].

Nevertheless, these procedures are very sensitive to the combination of process parameters, i.e. the metals used, the specific adsorbed anions and the applied potentials. Therefore, these conditions have to be chosen in a range of highest controllability, i.e. low electrode potentials and anions with low metal interaction properties.

Successfully reconstructed gold surfaces in Cl^- solutions have been presented in this manner [111, 112].

Beyond the scope of reconstructing closed macroscopic surfaces these techniques seem to be well capable to reconstruct microscopic metallic objects on nanometer scales, which is due to the typically smooth surface treatment [113, 114].

4.2.2   Other Reconstruction Techniques

In section 4.2.1 electrochemical surface reconstruction techniques are presented. Beside this, other techniques mainly based on thermal surface annealing procedures are established and used to remove surface defects. Two of these techniques are discussed in the following sections.

Sputtering, Thermal Evaporation and Annealing

One of the safest and best approved electrode surface reconstruction technique is performed by alternating cycles of sputtering and thermal annealing under UHV conditions [115]. Furthermore, also thermal evaporation under UHV conditions and post thermal annealing of noble metals, deliver very good results for connected large area metal surfaces [16, 116]. However, thermal post processing techniques are regrettably of limited benefit for a successful treatment of nano-structured metallic surfaces. Recent works show the thermal annealing of particular gold nano-antennae [18]. Structures with high aspect ratio and small feature sizes of less than $80 \, \mathrm{nm}$ suffer from enormous surface tension and stress caused by Rayleigh instabilities [18, 117, 118]. These surface tension phenomena can lead to a further structure segmentation or even to a complete destruction of the underlying metal objects [18].

Flame Annealing

An additional method used to process robust surfaces is given by the flame annealing procedure. This method works particularly for closed metallic surfaces [119] and even for metallic films, deposited on glass substrates [120]. The high temperatures given by the flame and mainly localized at the metals surface, leads to a melting of the upper metal surface layers and a subsequent controlled crystalisation. This method is widely used to prepare single crystal electrode surfaces with high quality and low effort.
The criticality of this method applied for nano-structured surfaces is expected to be similar to other thermal annealing techniques, or even worse. This is due to the fact that the high temperature gradients occurring at the metals surfaces might lead to nearly uncontrollable surface degeneration and the formation of metal drops. Thus, for the reconstruction of nano-structured surfaces, a more gentle technique should be acquired.

4.3 Modification of Optical Properties

In our work we investigate the optical properties of metallic nano-structures in general and the change of optical properties assisted by an electrochemical treatment in particular. Thus, the properties of light interaction with nano-structured materials are described in section 2 and 3. Beyond the already given scope, we want to summarize the described electrochemical effects and discuss the influences on the optical material properties, which form the background to understand the experimental results given in section 7 and 8.

4.3.1 Modification of the Electronic Properties of Metals

The optical properties of metals can be understood in good approximation within the notion of a free electron gas, which finds its classical analytical representation within the Drude model (compare section 2.2.2). By implementing the described metal surfaces in an electrochemical cell, it becomes possible to modify the electronic properties, with respect to its characteristics under ambient conditions.

Several experiments show a significant change even for the mechanical properties of metals in an electrochemical environment. This emphasizes the notion of a modified electron gas [121–123].

A characteristic feature describing this behavior is given by the considerably high capacity of the metal electrolyte interface which reaches values up to $50\mu\mathrm{Fcm}^{-2}$. This behavior can simply be understood within the GCS capacitor model (compare section 4.1.1).

By assuming a "plate distance" of $0.3\,\mathrm{nm}$, which corresponds to a mono layer of solvation water, surface charge densities up to $50\mu\mathrm{Ccm}^{-2}$, corresponding to surface charges up to 0.2 electrons per surface atom and extremely strong electric fields ($3 \times 10^7\mathrm{Vcm}^{-1}$) can be achieved [102]. Beyond the capacitive approach, all effects incorporating the excess charge densities, e.g. ad- and desorption, various forms of chemical surface reactions, oxidation and reduction processes induce a modification with respect to the unpersuaded metallic properties. These charge related modifications can be understood as an effective in- or decrease of the metals charge carrier density [69]. An alternative interpretation is given by an expansion or compression of the electron gas, due to a in- or decrease of the net free electrons within the metal [70, 124].

By interpreting the induced change of electrons in metals in terms of a modification within the charge carrier density, it becomes obvious that this change influences its optical properties (compare section 2.2.2).

This can be motivated by discussing a small metallic particle where an induced charge density change, e.g. within a electrochemical environment, leads to a modification within the plasmafrequency (compare section 2.2.2).

Following the derivation given in [69] we obtain for the real part of the Drude relation given in Eq. (2.33)

$$\epsilon'(\omega) = \epsilon_\infty - \frac{\omega_{\mathrm{pl}}^2}{\omega^2 + \gamma_c^2}. \tag{4.6}$$

Taking into account the plasma frequency

$$\omega_{\mathrm{pl}} = \sqrt{\frac{n_e e^2}{m_e \epsilon_0}}, \tag{4.7}$$

where n_e denotes the electron density, e the electron charge and m_e the electron mass. By increasing the charge density n_e by Δn_e one can see, that the plasmafrequency ω_{pl} shifts by $\Delta\omega_{\mathrm{pl}}$ up to higher values. By assuming a considerable small damping γ_c we obtain the altered Drude function, given by

$$\epsilon'(\omega) = \epsilon_\infty - \frac{\omega_{\mathrm{pl}}^2 + \Delta\omega_{\mathrm{pl}}^2}{\omega^2}. \tag{4.8}$$

The change in the dielectric function of the metal can be discussed in terms of a small metallic particle. According to the discussion of section 2.3.2 and [69], the absorption modes of a small metallic particle of arbitrary shape fulfill the relation

$$(1 - L_i)\epsilon_m + L_i\epsilon'(\omega) = 0. \tag{4.9}$$

Here, ϵ_m describes the dielectric background and L_i the geometry dependent depolarization factor. Combining Eq. (4.8) and Eq. (4.9) yields

$$(1 - L_i)\epsilon_m + L_i\epsilon_\infty - L_i\frac{\omega_{\mathrm{pl}}^2 + \Delta\omega_{\mathrm{pl}}^2}{\omega^2} = 0. \tag{4.10}$$

Introducing the plasmafrequency from Eq. (4.7) we can bring Eq. (4.10) to the following form

$$(1 - L_i)\epsilon_m + L_i\epsilon_\infty - L_i\frac{\omega_{\mathrm{pl}}^2}{\omega^2}\left(1 + \frac{\Delta n_e}{n_e}\right) = 0, \tag{4.11}$$

where ω is the peak central frequency of the plasmon excitation. Using for instance a gold particle we obtain a plasmafrequency of $\omega_{\mathrm{pl}} = 2\pi \times 2064 \times 10^{12}\,\mathrm{s}^{-1}$ [16]. We assume minute changes in the electron density only $\frac{\Delta n_e}{n_e} \ll 1$. Further simplifying leads to

$$\omega^2 = \omega_{\mathrm{pl}}^2\left(1 + \frac{\Delta n_e}{n_e}\right)\frac{1}{\epsilon_\infty + \left(\frac{1}{L_i} - 1\right)\epsilon_m}. \tag{4.12}$$

This relation directly links the central plasmon frequency to the charge density change and the geometry parameter. At this point it becomes obvious that a change in the charge density within this particle leads to a modified central frequency. To clarify this we write Eq. (4.12) in the form

$$\omega^2 = \omega_0^2\left(1 + \frac{\Delta n_e}{n_e}\right). \tag{4.13}$$

Here, ω_0 is a substitution given by

$$\omega_0^2 = \omega_{\mathrm{pl}}^2\frac{1}{\epsilon_\infty + \left(\frac{1}{L_i} - 1\right)\epsilon_m}, \tag{4.14}$$

describing the plasmon position within the unpersuaded state where no charge density occurred. The frequency shifts can be written as

$$\Delta\omega^2 = \omega^2 - \omega_0^2 = \frac{\Delta n_e}{n_e}\omega_{\mathrm{pl}}\frac{1}{\epsilon_\infty + \left(\frac{1}{L_i} - 1\right)\epsilon_m}. \tag{4.15}$$

In Eq. (4.15) one obviously finds that a shift in the plasmon resonance frequency $\Delta\omega$ is directly linked to a modification in the electron density Δn_e. Thus, we can extract from Eq. (4.12) that an increase in the electron density n_e leads to an increase in the central resonance frequency of the plasmon and *vice versa*. The charge dependent frequency shift can be reduced to the relation

$$\frac{\omega}{\omega_0} = \sqrt{1 + \frac{\Delta n_e}{n_e}}. \tag{4.16}$$

By taking into account the geometry parameter L_i one finds that a shift in the central resonance frequency is increased for increasing values of L_i (compare Eq. (4.15)). Therfore, elongated particles are supposed to exhibit a more pronounced shift of the central resonance frequency.

The discussed example is in good agreement to experimental observations incorporating elongated gold nano-particles [69].

4.3.2   Modification of the Intrinsic Damping

Influencing the electron density within a metal in contact to an electrochemical environment, is only one aspect of the interaction between both. Another aspect is related to the reversible and irreversible modification processes, changing the charge transport properties within the metals crystal structure (compare section 4.2.1). Therefore, reversible processes occur for instance by specific adsorption phenomena of certain ionic species onto the metals surface. These adsorbates alter the scattering properties of the free electrons in metals (compare section 2.2.2) and lead to a reversible contribution of electrons dissipation [114].
This can well be understood in terms of a small metallic spherical particle in an electrochemical environment and interacting with light. The optical properties can be described by its extinction crossection C_{ext}, given according to Eq. (2.52) in section 2.3.2.

$$C_{\mathrm{ext}} = 9\frac{\omega}{c}\epsilon_m^{\frac{3}{2}}V_{\mathrm{Sphere}}\frac{\epsilon_2}{\left(\epsilon_1 + 2\epsilon_m\right)^2 + \epsilon_2^2}.$$

Here, V_{Sphere} is the volume of the sphere ϵ_m the background dielectric function and the real- and imaginary part of the metal dielectric function $\epsilon = \epsilon_1 + \mathrm{i}\epsilon_2$ given by

$$\epsilon_1 = \epsilon_\infty - \frac{\omega_{pl}^2}{\left(\omega^2 + \gamma_c^2\right)} \qquad \epsilon_2 = \frac{\omega_{pl}^2 \gamma_c}{\omega\left(\omega^2 + \gamma_c^2\right)}, \tag{4.17}$$

where the plasma frequency is given by $\omega_{\mathrm{pl}} = \sqrt{\frac{n_e e^2}{m_e \epsilon_0}}$ and γ_c describes the damping.
Within the electrochemical environment ionic species can be specifically adsorped on a metal surface for a given electrode potential. As discussed in section 2.2.3, surface adsorbates and defects in general can influence the electron scattering properties within the metal. This typically leads to an increased resistivity ρ within the metal film. The change in resistivity can be directly linked to the damping within the Drude model. Following the derivation given in [114] we obtain

$$\gamma_c = \frac{v_f}{\rho}, \tag{4.18}$$

where v_f describes the Fermi velocity, i.e. the velocity for electrons at the Fermi energy. By changing the resistivity of the metal, one obviously influences the damping and the extinction of the particle. This is depicted in Fig. 4.3, where a change is the damping is displayed. The black graph describes the extinction for the Drude damping. By increasing the damping γ_c by $30\,\%$ (red) and $60\,\%$ (blue), one finds a decrease in the extinction height and a broadening of the resonance profile. Typically the specific adsorption of ionic species is a reversible process. Therfore, the related damping increase is prosumable reversible as well.

In contrast to the reversible adsorbance effects discribed, irreversible effects occur, which can be separated informally into desired and non desired phenomena. A desired effect, which leads to superior metal properties by reducing grain boundaries and crystal defects, is described in section 4.2.1. The discribed surface smoothening decreases the scattering dissipation of electrons at metals boundary planes and reduces the electron dissipation or damping. Undesired effects are for instance oxidation and reduction processes, which might lead to a
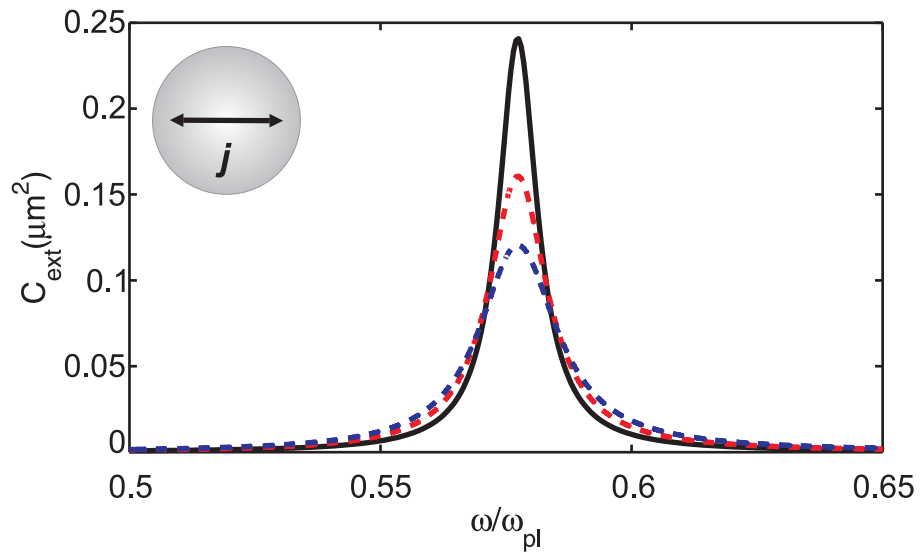
Figure 4.3: In this graph the extinction cross sections of a small spherical gold particle in vacuum for different damping values γ are depicted. The diameter of the assumed particle is $d = 100\,\text{nm}$. The values for the plasma frequency and the damping are given by $\omega_{\text{pl}} = 2\pi \times 2064 \times 10^{12}\,\text{s}^{-1}$ and $\gamma_c = 2\pi \times 19.4 \times 10^{12}\,\text{s}^{-1}$ [16]. The extinction for $\gamma = \gamma_c$ is depicted in black, for $\gamma = 1.5\gamma_c$ in red and for $\gamma = 2.0\gamma_c$ in blue. The value for ϵ_∞ is set to unity.

segmentation of the surface till to the point of destruction. These effects typically occur for high positive electrode potentials and can usually well be suppressed by a proper choice of process parameters.

Chapter 5

Fabrication

In this chapter, we describe the sample fabrication, starting with the template manufacturing performed by electron-beam lithography, which is crucial for the whole fabrication procedure. This technique has a superior resolution compared to other methods, for instance, optical lithography. Subsequently, we describe the pre- and post-processing steps, which are necessary to prepare the samples for lithography and to transfer the lithographical manufactured templates in a functional sample afterwards. The sample fabrication in general is a procedure, which is generically grown in our group and is adjusted to the individual experimental needs. The basic steps are very similar to each other, which explains the similarities in description. The interested reader finds fabrication details beyond the scope of our work in [55, 125, 126]. We close the chapter with a brief overview of two alternative lithographic fabrication techniques, focused-ion-beam and laser-interference lithography, in order to face the advantages and disadvantages of the specific methods.

5.1   Electron-Beam Lithography

One major advantage of electron-beam lithography, compared to other lithography techniques are the outstanding resolution properties of this method. The lithography process is performed by an accelerated, shaped and focused electron beam impinging onto a thin ($\approx 200\,\mathrm{nm}$) electron-beam-resist layer, which modifies the resist layer in a spatially localized region. The electron-beam-resist used for our purposes is the polymer polymethyl methacrylate (PMMA)[1]. The PMMA is a so-called positive tone resist, meaning that the exposed parts can be selectively dissolved in an etchant, we call the developer. The remaining template is a hole mask, which can be used for further post-processing steps. In our case, these steps include the evaporation of thin metallic or dielectric material layers with a subsequently performed lift-off procedure. In the lift-off procedure we dispose the non-functional parts of the template by dissolving the resist-mask and the thereon evaporated residues. We end up with the final functional structure remaining on the substrate surface. In this section, we also give a detailed discription of the sample pre- and post-processing technologies as well as the

---

[1]PMMA 950K A4 (4%-solution in anisole), MicroChem Corp. (USA)
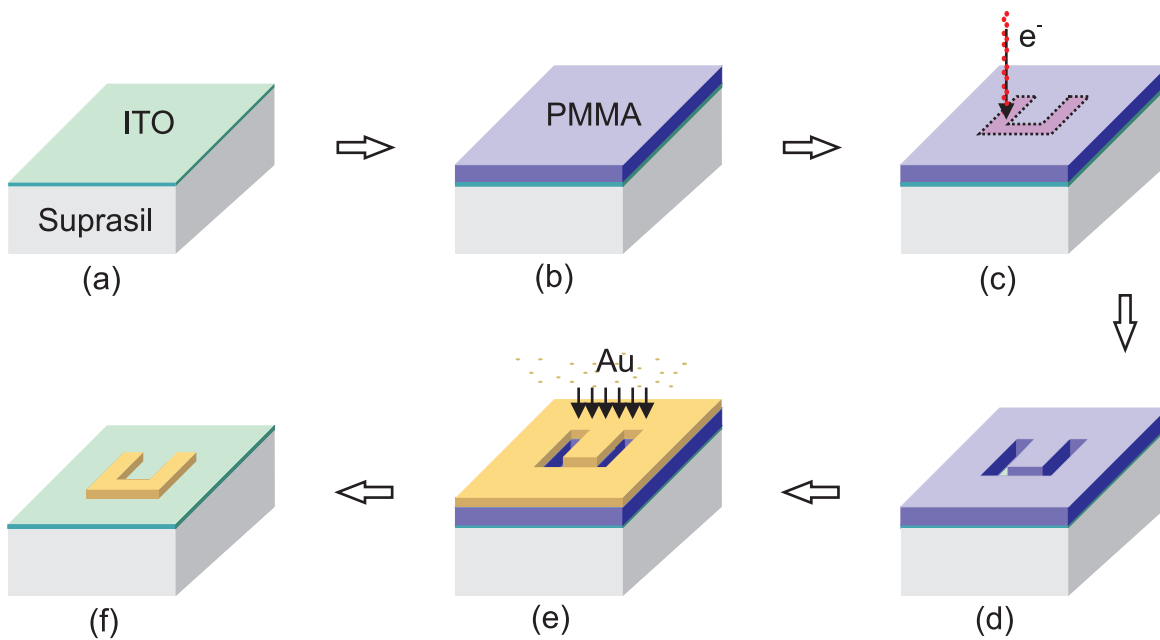
Figure 5.1: Sketch of the entire fabrication process cycle as explained in detail in the main text: we start with a clean, ITO-covered glass substrate (a), that is spin-coated with the electron-beam sensitive resist PMMA (b). The focused electron-beam modifies the resist (c), making it selectively soluble in the developer, with the consequence that the exposed parts are etched away (d). After the development, we evaporate metallic layers (e). The lift-off procedure removes the PMMA-mask with the non-functional residues on top and the functional nanostructure remains (f). Adapted from [125]

lithography used for our purpuses. The complete preperation cycle is sketched in Fig. 5.1. The principle of this serial fabrication technique is closely related to the one needed for focused ion beam lithography.

5.1.1 Pre-Processing: Sample Preparation

The substrate used for lithography is a slab of Suprasil[2]. It is of upmost importance, that the substrate surface roughness is well below the desired feature sizes of the functional structures. This can be guaranteed by a special surface polishing performed by the manufacturer. In addition, this material fulfills all requirements, which are necessary for transmittance spectroscopy at optical wavelength, namely a high transmittance over a broad spectral range. Due to the fact, that the electrons used for lithography impinge the surface of the sample substrate and cause local charging effects, we need a conductive substrate with comparable transmittance properties compared to bare suprasil. The constraints can be fulfilled by evaporating a $10\,\mathrm{nm}$-thin layer of indium tin oxide (ITO), which has a sufficient DC conductivity and is transparent for optical wavelength [128]. In addition this layer has also a functional role during the electro-optical measurements, as it is part of the working electrode (compare 6.2.1).

---

[2]Suprasil is a high-purity quartz glass. A slab of $2\,\mathrm{mm}$-thickness has about 90% transmittance between $0.2\,\mathrm{\mu m}$ and $2.5\,\mathrm{\mu m}$ wavelengths [127].

Cleaning the Substrates The cleaning procedure is substantial to guarantee the production of a good working and reproducible metamaterial samples. First of all, the non sticking residues are blown away with a strong nitrogen flow. Subsequently, the sample is immersed in a bath of $80°C$ hot acetone and cleaned in a ultrasonic bath for 10 minutes. After having taken the sample out of the acetone it is blown dry with the nitrogen flow and polished with an acetone soaked lens-cleaning paper. This procedure is repeated until all visible residues are removed. This can be easily checked with a strong light source irradiating the surface. The residues act as good scatterers on the sample surface. Thereafter, the sample is rinsed under isopropyl alcohol (IPA) and blown dry again with a strong nitrogen flow. After these cleaning steps the sample is ready for further pre-processing.

Covering with Indium Tin Oxide In the subsequent step, we evaporate a $10\,nm$-thin ITO-layer in an electron-beam evaporation system (see below) under an oxygen atmosphere with a partial pressure of $p_{O_2} = 1.2 \times 10^{-5}\,mbar$. After evaporation, the deposited ITO-layer looks only slightly transparent. This can be repaired with an annealing procedure following the evaporation. This procedure is performed under ambient conditions in a tube furnace with temperatures of $400°C$ for six hours [129, 130]. To avoid thermal induced tension, which might lead to cracks in the surface ITO-layer, heating and cooling of the oven is performed with a temperature gradient of $5°C\,min^{-1}$. After annealing, the ITO-layer is transparent and conductive. The requirements are needed for the electron-beam lithography as well as for the electro-optical experiments.

Spin-Coating and Developing the Electron-Beam Resist The PMMA photo-resist is now spin-coated on the clean ITO-covered substrate. The spin-coating process is a state-of-the-art coating technique, which allows to produce very reproducible and homogeneous films even on big areas, e.g. silicon wafers. Our process consists of two subsequent production steps: (i) three seconds at $300\,rpm$ to disperse the resist over the substrate and cover it homogeneously and (ii) 120 seconds at $6000\,rpm$ resulting in a final PMMA-layer thickness of about $200\,nm$. Finally, the resist is baked in a convection oven at $165°C$ for 45 minutes under ambient pressure in order to remove all solvent residues left in the PMMA.
For PMMA, the exposed regions are selectively etched by the developer [1 : 3-mixture of MIBK (methyl isobutyl ketone) and IPA (isopropyl alcohol)]. We develop the exposed PMMA under ambient conditions for six to ten seconds depending on the structure design and the lithography parameters. Finally, we immerse the sample in a bath of IPA to stop the etching.

5.1.2 Lithography

Lithographical Setup The electron-beam lithography system is based on a commercial scanning-electron microscope (SEM) that is specifically extended and only used for electron-
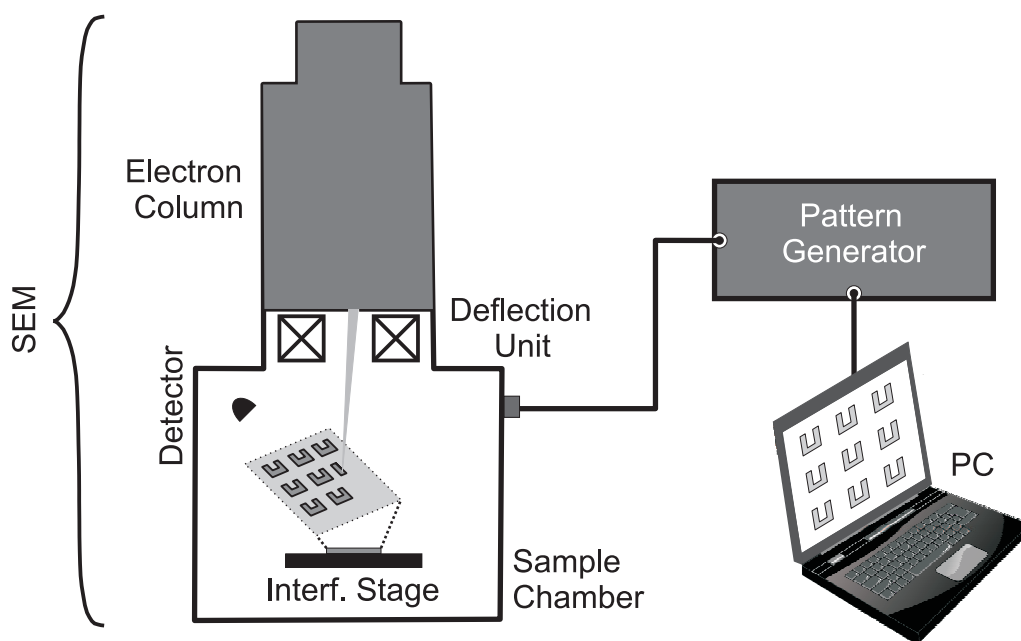
Figure 5.2: Sketch of an electron beam lithography system based on a SEM and a control unit consisting of a usual PC and a pattern generator. The trajectory of the electron beam is visualized by the grey-shaded areas. The interferometric positioning stage allows to align and re-align positions on the sample with an accuracy of 2 nm, a position repeatability below 40 nm and a total travel range of 100 mm × 100 mm. The exposed sample design is created by the computer aided design software e-LINE.

beam lithography. The system used is a RAITH e-LINE[3] consisting of two main components as sketched in Fig. 5.2: the column where the electron beam is generated, accelerated, shaped and focused onto the sample and the sample chamber containing the positioning stage with the specimen mount and the detectors delivering the information for imaging. For this lithography SEM the manufacturer claims 1.7 nm resolution at an acceleration voltage of 15 kV. A more detailed description of the SEM and its assembly is given in 6.1.1.

The deflection unit can be controlled externally by the so-called pattern generator as depicted in Fig. 5.2. The electron beam can be deflected in a way that it traces the constructed sample-design. Even a complete beam blank is possible, which is mandatory for a sequential exposure of the sample. Additionally, an ampere meter is added (not shown), measuring the electron-beam current. For the production of high quality samples it is important to have the ability to align and realign samples. In our case, this is performed by an interferometrically controlled stage allowing for positioning with an accuracy of 2 nm, a position repeatability below 40 nm and a total travel range of 100 mm × 100 mm. All values depend on manufacturer specifications.

For designing the structure we use a computer aided design software, provided with RAITH e-LINE. The structure is defined by geometrical shapes composed of areas, polygons and lines. The designed structure is discretized, *i.e.*, divided into squares of 4 nm edge length for areas and line elements of 2 nm for lines - the so-called step size - and then transfered to the

---

[3]Raith GmbH, Dortmund (Germany)

pattern generator.

Two different exposure modi within the e-line software can be distinguished: (i) The area mode where the electron beam meanders over the areas enclosed by the polygon boundaries and (ii) the line mode, where the beam only follows the line path defined in the computer aided design software. In the first case the deposited dose is dispensed over the whole area of the desired geometrical structure design, leading to well defined, nearly rectangular structures being as close as possible to the defined structure design. In the line mode the beam only follows the line path. By adapting the deposited dose one can control the exposed area caused by the line broadening (see below). This will lead to structures with more or less rounded edges. By decreasing the feature sizes of the geometrical objects and the lattice constant, meaning the displacement of one object to another, it is a challenge to achieve well defined and separated structures. This is due to the fact, that the impinging electrons scatter within the resist and back-scatter on the substrate surface, which will lead to an effective broadening of the exposed profile. This effect is betoken as proximity-effect, meaning that two neighbored beam profiles in close proximity overlap, which might lead till to the point of a merged structure design. For small and only slightly separated structures it is advantageous to use the line mode, as it minimizes the proximity-effect compared the the area mode for this regime. The exposed doses for line- and area mode are defined by relative dose factors. The relative dose factor is the tuning parameter, which is systematically varied to achieve a proper sample design. For instance, one should decrease the relative dose factors for decreasing structure- and line separations and *vice versa*. The dwell time depends on the resist sensitivity, the step size and the current of the electron beam. The resist sensitivity depends on the acceleration voltage and inherent resist properties. For the area design elements, we use $400\,\mu C\,cm^{-2}$ and for the line design elements $6000\,pC\,cm^{-1}$ as resist sensitivity for PMMA 950k A4[4] at $30\,kV$ acceleration voltage. The step size is set to $2\,nm$ or $4\,nm$, respectively . Before starting an exposure process, we measure the current, which is usually about $90\,pA$ and $4000\,pA$ for $20\,\mu m$ and $120\,\mu m$ aperture diameters, respectively. The lithography is performed at a working distance of about $12\,mm$ with a magnification of $1000\times$. With these settings, the electron beam can be deflected within an area of $100\,\mu m \times 100\,\mu m$. This is defined as write field. In a nutshell, this area defines the operating range of the electron beam, without shifting the sample by moving the stage. The evaluation of the relative dose factors is the most time consuming part in sample preparation. It leads to structures, which are as close to the theoretical parameters as possible. Thus, these parameters have to be adapted for each structure design to compensate the proximity effect, the fluctuations given by the setup itself and the pre-processing of the sample.

Resolution   The resolution of electron-beam lithography is limited by constraints given by the apparatus and the substrate as well as the intrinsic resolution capability of the photo resist. Three major effects can be distinguished:

(i) The lateral dimensions and the profile of the electron beam in the resist: the size has to be as small as allowed by hardware restrictions and the shape should be as close to

---

[4]PMMA 950k A4 in Anisol, MicroChem (USA)

circular as possible. Both are manually adjusted through the user by a procedure called contamination-spot-burning. Here, we directly spot the beam on a position of the resist surface for several seconds. This leads to a spatially confined contamination on the resist surface visible as a degenerated area in the SEM image. The electromagnetic lenses are adjusted in a way that the spot is circular and as small as possible.

(ii) Proximity effect [131]: within the PMMA resist and the substrate the electron beam is scattered. Furthermore, the electrons generate secondary electrons, which also have enough energy to expose regions of the resist that are delocalized from the primary electron beam trace. The influence of the proximity effect concerning the resolution depends on the acceleration voltage, the resist and the substrate material used. Scattering calculations as well as experienced knowledge show that an increase in the acceleration voltage leads to a decrease in the proximity effect. Therefore, we used the largest acceleration voltage available for this system, this is $30\,\mathrm{kV}$.

(iii) Intrinsic resolution of the resist: The manufacturer of the resist PMMA used for lithography specifies a resolution of less than $100\,\mathrm{nm}$. This is a quite pessimistic approximation, as in this work, we have fabricated structures with feature sizes well below $30\,\mathrm{nm}$ and in Ref. [132] feature sizes of $5\,\mathrm{nm}$ in PMMA have been manufactured.

5.1.3   Post-Processing: Creating Metallic Nano-Structures

For our purposes the polymer templates fabricated by electron-beam lithography are only used as an intermediate step in metamaterial production. These developed polymer templates are covered with thin metal or metal-dielectric composites. This is performed by an electron-beam evaporation system, where the beam is focused onto the desired material placed in a heat resistant crucible under vacuum conditions. The impinging electrons locally heat the material until evaporation. A schematic sketch is depicted in Fig.5.4 a). Due to the fact, that the material is only heated in a spatially confined area, this method has superior properties concerning the controllability and reproducibility of the process, the purity of the films and the directionality of the material beam, compared to other physical vapor deposition techniques. The highly directed material beam is a unique feature of this setup; it is crucial for fabricating high quality structures. The deposited material rate and thickness on the sample is monitored with two separated quartz crystals. The material beam in direction to the specimen can be sequentially intercepted by a shutter. For our purposes we cover the polymer template on the ITO covered substrate with a nominally $2\,\mathrm{nm}$ thick chromium (Cr) layer, that acts as an adhesion promoter. Subsequently, the functional layer of gold is deposited with varying film thicknesses. The process takes place at a pressure of about $5 \times 10^{-7}\,\mathrm{mbar}$ and an evaporation rate of $0.1\,\mathrm{nm\,s^{-1}}$. As already mentioned, the evaporation process of the ITO films works similarly. However, ITO is evaporated under an ambient oxygen atmosphere (see above).

In the following step the polymer mask with the metal residues on top are removed in the so-called lift-off procedure.
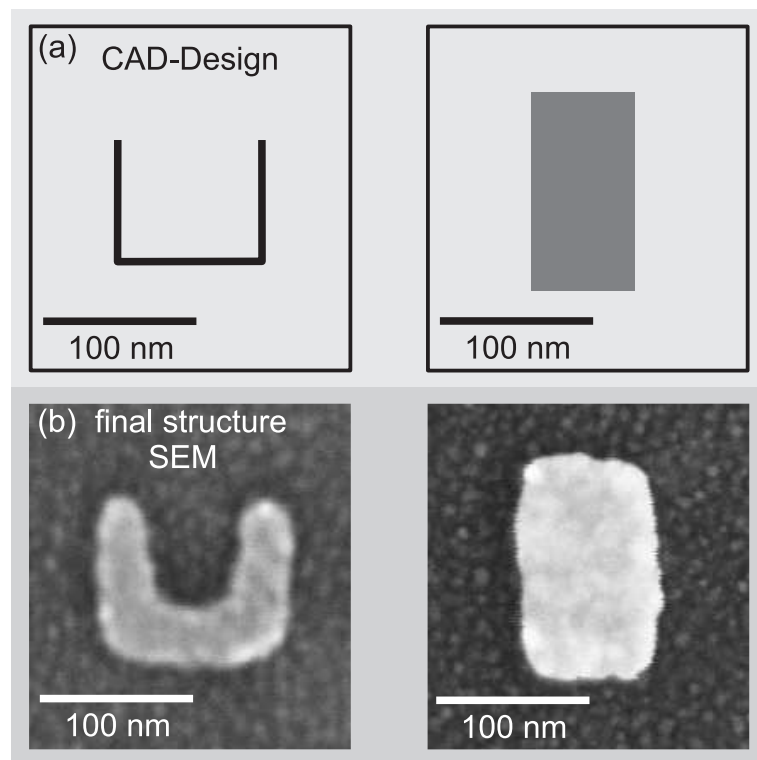
Figure 5.3: (a) A split-ring resonator and an antenna patch as designed in the e-LINE-software tool. Left: the design elements are lines. Right: the design elements are areas. (b) The corresponding scanning-electron micrographs of the finally processed structures consisting of a 2 nm thick chromium adhesion layer, 12 nm of gold for the left- and 11 nm of gold for the structure in the right column. For those structures designed with area design elements, the corners are sharper than for the line elements.

When exceeding accumulated layer thicknesses of about 15 nm, we obtain closed metallic films. Below 15 nm the metal forms islands resulting in a discontinuous, percolated film [see Fig.5.4 b)]. The production, investigation and restructuring of very thin metal layers, even below the percolation threshold is an essential part of this work. Therefore, we discuss the details in production seperately (see below).

After metal deposition we remove the polymer template in a hot solution of AR 300-70[5], a commercially available lift-off composition. This solvent is especially developed for metal-coated PMMA lift-off procedures. The liquid is filled in a glass beaker, placed on a hotplate at constant temperature of about 60 °C. The lift-off solution is agitated by a magnetic stir bar on the bottom of the beaker. This is important in order to prevent a sticking of diluted metal residues on the surface of the sample. The specimen is fixed by a pair of tweezers and immersed in the solution. After approximately 120 min all polymer and metal residues are removed from the surface. Subsequently, the sample is rinsed with IPA and dried carefully under a nitrogen flow.

---

[5] AR 300-70 Allresist GmbH (Germany)

(a)   E-VAP

Thickness Crystal

Specimen

Rate Crystal

Aperture

Shutter

Electron
Source

(b)   Gold Films on 2nm Chromium

Au:7.1 nm   Au:11.5 nm

100 nm   100 nm
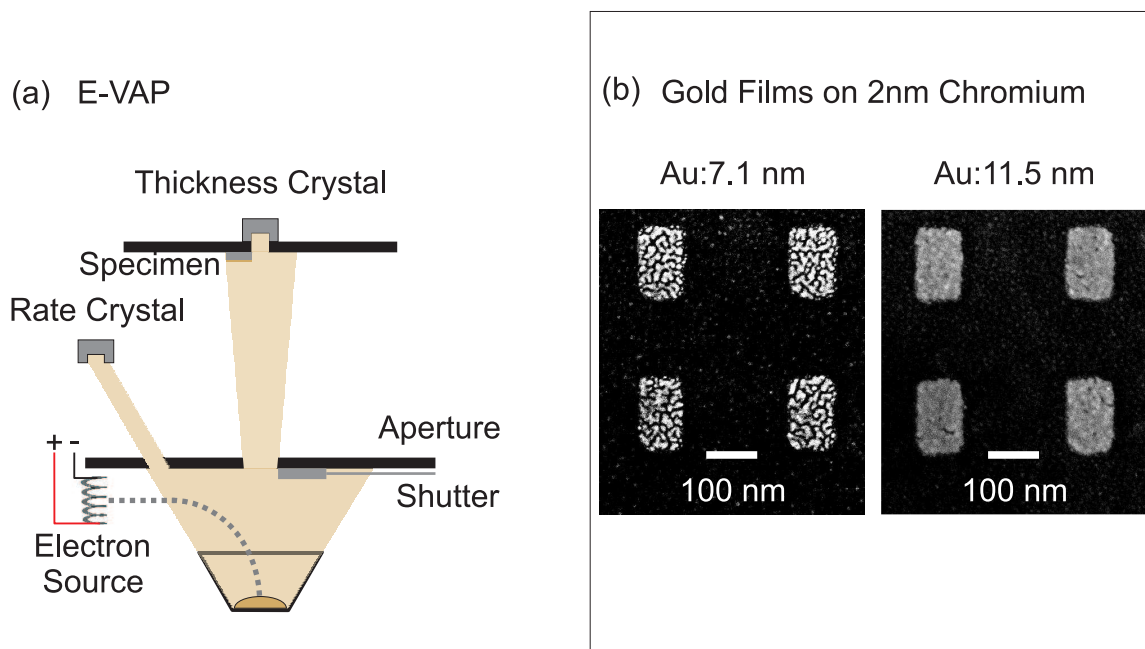
Figure 5.4: (a) Schematic sketch of the electron-beam evaporation system e-VAP. This system consists of a electron source, where the accelerated electrons are deflected on the material used for evaporation. The material is locally heated and the evaporation rate is controlled by a quartz crystal system, while the sample, placed upside down, is shaded by a shutter. When the desired rate is attained and stable, the shutter can be opened and the thickness crystal measures the deposited material thickness. This system is in close vicinity to the sample to avoid lateral rate changes. The spatial distribution of the beam is very low. This leads to a good directed, nearly perpendicular material evaporation, relative to the specimen surface. When the desired material thickness is achieved, the shutter closes to suppress further evaporation. (b) Two different arrays of metallic antennae are displayed. On the left hand side, there is depicted an electron micrograph of periodically arranged antennae on a ITO covered substrate. The structures consists of 2nm Cr as adhesion promoter and a gold layer of 7.1 nm. On the right hand side a nominally similar structure is depicted, with the same 2nm Cr adhesion promoter, but with layer of 11.5 nm gold. The thickness values are investigated by AFM measurements. One can clearly see the percolated film forming metal islands, on the left hand side and the much better film with less surface corrugation on the right hand side.

Ultra-Thin Metallic Layers   The production of thin metal layers is of utmost importance in our experiments. The surface to volume ratio of the metallic objects forming the metamaterial is a relevant value. The optical properties can be influenced by scaling the lateral dimensions as well as the height of the plasmonic objects (compare chapter 3.3). These parameters are varied to maximize the surface to volume ratio and therefore maximize the investigated electrochemically induced effects in the optical measurements. Simultaneously, these parameters also influence the optical properties and the resonance positions of the underlying metamaterial structures. The variations of these parameters are obviously a very delicate procedure as there are several constraints which have to be taken into account.

For instance, there is a lower boundary limiting the scaling options at optical frequencies (see chapter 3.3), which is given by the limit of size scaling [19]. The aqueous electrolyte solution, used for the optical experiments, describes the upper boundary, which is opaque for wavelengths exceeding $1.4\,\mu m$. Therfore, one has to balance the lateral dimensions as well

as the height of the plasmonic objects to fulfill both, i.e. a maximized surface to volume ratio and a good metamaterial response within the given frequency range.

As mentioned in section 5.1.3, there is an additional restriction to the system given by the metal film percolation of evaporated thicknesses below $15\,\text{nm}$. To bypass these fabrication restrictions, it is mandatory to produce thin and reproducible metal layers and of tremendous importance to post-process these insufficient films, to achieve a high-quality thin-film metamaterial sample (see section 8).

The layers are manufactured as described in section 5.1.3, but differ so far, that the thickness monitoring by the quartz crystals works insufficiently for thin material layers. This might be due to the fact, that the thickness measuring crystal is not in thermal equilibrium for the first seconds during the evaporation (compare Fig.5.4). Therefore, a calibration sample of different thicknesses and materials (chromium and gold) has been manufactured with a constant rate of $0.1\,\text{nm}\,\text{s}^{-1}$ and measured over time. These samples are measured by atomic force microscopy afterwards to determine the real layer thicknesses (see section 6.1.2). This method gives fairly reproducible results as the fluctuations of the rate crystals are very moderate.

5.2 Focused-Ion-Beam Lithography

Focused-ion-beam milling is a material treatment method, which allows to directly remove material in confined areas. From this point of view, this method has a big advantage compared to electron-beam lithography, caused by the direct surface treatment without fabricating a template mask first. Typical feature sizes are smaller than $100\,\text{nm}$ [133], which is also comparable to the e-beam resolution in polymer photo resists. The apparatus used is very similar to an SEM as well. The major difference is, that ions (usually Ga^+-ions) are accelerated and focused onto the surface of the sample, instead of the electrons. The Ga^+-ions impinge onto the material surface and remove surface atoms. This is possible because the momentum and energy transfered is much bigger, compared to electrons. The disadvantage of this method is that the decelerated Ga^+-ions are partly embedded in the crystal matrix of the remaining material. This leads to impurities influencing the material properties. In addition, parts of the removed material redeposit on the surface of the material, which further lead to contaminations.

Nevertheless, with this method several photonic metamaterials have been fabricated [54, 87]. Unfortunately, when patterning metals like gold [87] or silver [54], the optical quality of the material is influenced by the Ga^+-ions embedded in the metal lattices. These impurities in the crystal matrix act as further scatterers for the conductance electrons, increasing the material inherent or ohmic damping. Therefore, the optical merit suffers significantly. These specific disadvantages can be hardly compensated by the fact, that post-processing steps equal to the ones used for e-beam lithography are dispensable.

5.3   Laser-Interference Lithography

The excellence in laser-interference lithography is due to the fact, that it is possible to expose large areas of cm^2 with single features on the nanometer scale at once. The working principle contains two or more interfering laser beams leading to a well determined intensity pattern [134]. This takes place in a photo sensitive material, which is chemically altered in the regions of high intensity. After exposure, the photo resist can be selectively etched and usually forms a template for post-processing.

For a one-dimensional (1D) periodic intensity variation two interfering beams are required, whereas three interfering beams lead to a periodic 2D intensity pattern. Both methods have been used for the fabricating planar metamaterial arrays [50, 68, 135]. Furthermore, three-beam interference lithography has been applied for the fabrication of planar metamaterial slabs [68].

The major drawback of this technique is a nearly static, hardly modifiable setup, leading to limitation in design freedom.

Chapter 6

Characterization

In this chapter, we discuss the experimental methods useed for investigating optical- and surface properties of metamaterial structures in air as well as in a fluidic electrolyte influenced by an external electric field. We start with the presentation of two surface analysis techniques used for pre- and post surface inspection. A description of the optical transmittance measurements and the setup used in its different variants follows.

6.1 Surface and Topography Characterization

For the optical effects discussed in this context both, constitution and morphology of the underlying nano-structures play an important role. To characterize these conditions, it is crucial to have the possibility to investigate the geometrical- as well as the surface-conditions before and equally important after the electrochemical treatment. This is mandatory to monitor reversible and irreversible effects. The methods of investigation used are briefly discussed in the following sections.

6.1.1 Scanning Electron Microscopy

The scanning electron microscope (SEM) is a special type of an electron microscope, which images the surface of a specimen by moving an electron beam in a well-defined scan pattern. The strongly accelerated electrons interact with the surface atoms of the specimen leading to signals, which contain information about e.g. surface topography, conductivity, or even material compositions. The invention of the first functional electron microscope has been reported in [136]. In our case, we use a Zeiss Ultra[1] electron microscope, which is schematically depicted in Fig. 6.1. It consists of two main components:

- The ultra high vacuum column, where the electron beam is generated, accelerated, shaped and deflected.

- The high vacuum chamber where the specimen is mounted on a positioning stage and the detectors deliver the signals for imaging.

---

[1]Carl Zeiss SMT AG, Oberkochen (Germany)
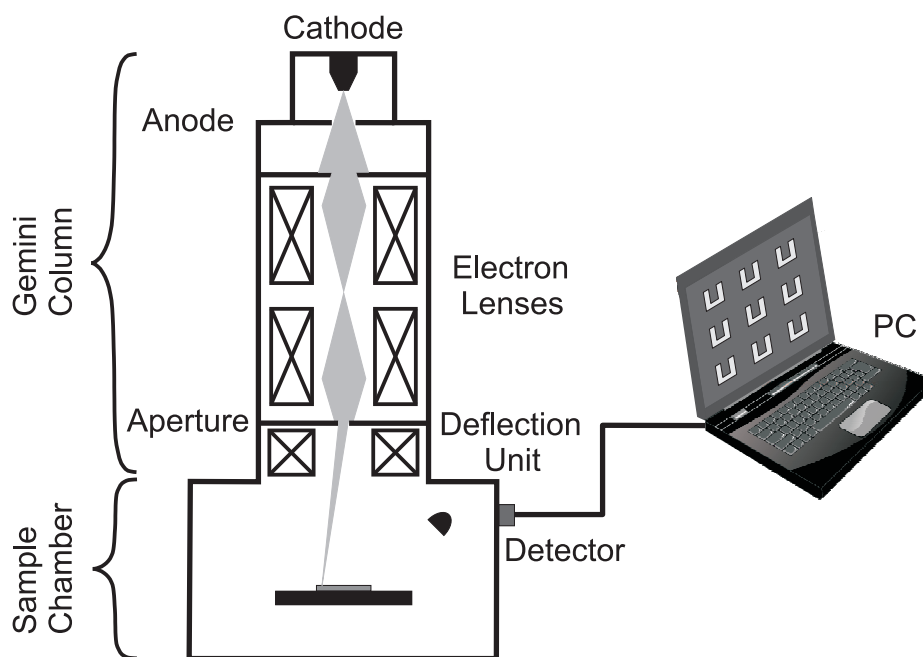
Figure 6.1: Sketch of a SEM consisting of the column and the sample chamber. The trajectory of the electron beam is visualized by the gray-shaded areas. A series of electron lenses provide a proper focussing and a nearly circular beam profile. The deflection unit scans the beam over the sample surface. The backscattered- and generated secondary electrons are collected by detectors, giving the information used to create an image.

The electrons used for high resolution microscopy are usually generated by field emitter sources. The major drawback of this method is the relatively low extracted current flux of electrons. The emitting unit used in our case, is placed on the top of the ultra high vacuum column Zeiss GEMINI[2]. It is a Schottky field emitter source, made of a heated ZrO reservoir and a Wolfram tip, the so-called filament. This source is based on the principle of thermally assisted field emission, where the advantages of a simple field emitter source, namely a very low energy distribution of electrons, is combined with an increased electron flux caused by the Schottky effect [137]. After having left the filament, the electrons are accelerated by an adjustable potential difference between cathode and anode. The subsequent electrostatic and magnetostatic electron-lenses in combination with an aperture lead to a well shaped and focused beam on the sample. Controlled by the deflection unit, the electron-beam can be rastered over the sample surface. Two detectors are available collecting the electrons coming form the specimen surface. The first detector is located within the beam column and is denoted as in-lens detector. This detector mainly collects the electrons that are scattered elastically at the specimen surface. Another so-called SE2 detector collects the secondary electrons generated by inelastic scattering processes. This detector is placed within the sample chamber. The desired image is generated by the delivered signal of the detectors, combined with the beam position given by the deflection unit. A special feature of this machine is an air lock system, which accelerates the workflow tremendously. It is possible to lock in one sample within minutes. Moreover, the sample chamber remains

---

[2]Carl Zeiss SMT AG, Oberkochen (Germany)
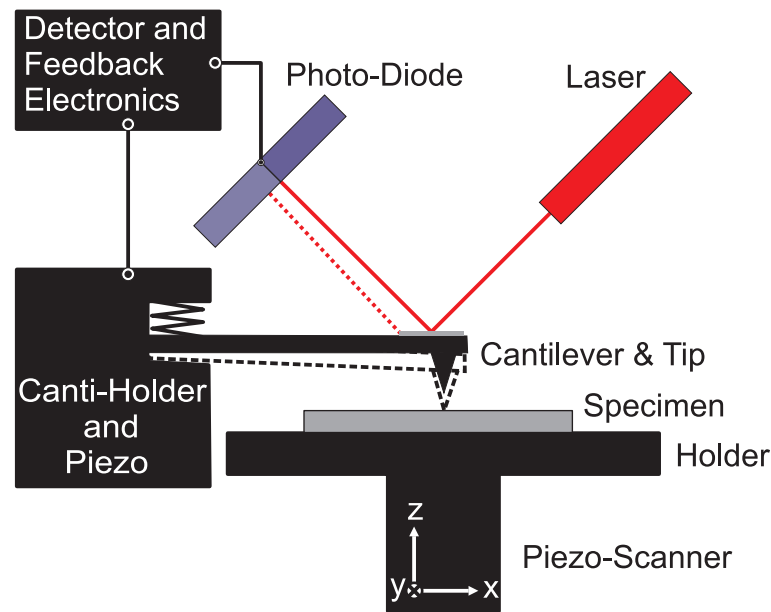
Figure 6.2: Sketch of an AFM consisting of the tube scanner, performing the lateral scans. The tip-holder with the piezo-unit where the tip is mounted and stimulated. The metal-coated backside of the tip reflects the laser beam of a solid state laser. The topography information detected by the tip, is translated in an angular beam shift, detected by a four quarter photo-diode.

very clean, which reduces carbon contaminations during the imaging process. In addition, a charge compensator system is installed, which enables to investigate non-conductive substrates.

This can be performed by a positively charged nitrogen jet, which locally compensates charged areas.

Comparable to usual optics, the resolution of electron optics is also restricted by imaging insufficiencies, i.e. diffractive-, chromatic and spherical aberrations, as well as astigmatism. The starting point for the outstanding resolution capability is the filament. The ZrO approximately forms a point source on the filament tip and the energy distribution of the emitted electrons is very low, which decreases chromatic aberrations. Spherical aberrations are minimized by a suitable choice of apertures and electron lenses along the beam column. The astigmatism can be influenced and corrected by a magnetic quadrupole field. Further details and more sophisticated beam-shape correction techniques can be found in [138–140]. Therefore, the total resolution capability of an electron optical system is much higher compared to usual optics. This is due to the typically much smaller de Broglie wavelength of electrons. Values smaller than one nanometer have been reported [141]. For our system, a resolution of 0.8 nm by an applied acceleration voltage of 15 kV is specified by the manufacturer.

6.1.2   Atomic Force Microscopy

The atomic force microscopy (AFM) is a high resolution imaging technique which allows to map the 3D topography information of a surface. The big advantage of this method compared to the scanning electron microscopy (SEM), discussed in the previous section, is a realistic true to scale three dimensional image of the surface. A schematic sketch of a typical AFM is given in Fig. 6.2. It mainly consists of a small Si-chip the so-called cantilever with a very fine tip on its one end, a piezo-scanner which performs the lateral scans, a laser source and a four segment photo-diode. By scanning over the specimen surface, the tip as well as the cantilever follows the surface corrugation. The laser spot reflected from the cantilevers back-side translates the movement in z-direction and the torsion of the cantilever to the four-segment diode. With the given signals, the topography information and the lateral-force or friction can be extracted. Three different working modi can be distinguished:

(i) The contact mode, where the cantilever is in contact with the surface. The topography information is generated either by the deflection signal at constant z-position of the piezo-scanner or vice versa. The cantilever used has a relatively low spring constant, which is necessary to have a good sensitivity for the deflection signal and to avoid surface damages caused by the tip.

(ii) The non-contact mode, where the cantilever does not touch the specimen. It is held in close proximity to the surface and performs externally driven oscillations near its free resonance frequency. The typical amplitudes are less than 10 nm in z-direction. The Van der Waals force, which contributes in this regime the strongest short range interaction, causes a distant dependent decrease of the cantilever oscillations. By pinning the cantilever frequency and amplitude, the tip-to-sample distance can be adjusted *via* a feedback mechanism. Therfore, the topography information can be extracted for every pair of lateral coordinates.

(iii) The so called tapping-mode, in which the cantilever also performs driven oscillations in z-direction. The working principle is similar to the non-contact mode, with the major differences, that the oscillation amplitude is about one order of magnitude higher and the tip touches the surface for a full elongation. The background for this modification is due to the fact, that nearly every kind of surface forms a thin water film on top under ambient conditions. The result for non-contact measurement techniques is, that the tip only images the surface of the top layer water film. The contact mode undergoes this undesired effect by penetrating this water meniscus and contacting the sample surface.

For our investigations we use the AFM Nanoscope Multimode[3]. The AFM is used in the tapping mode, on the one hand to avoid the surface modification by the cantilever tip and on the other hand to get reproducible and comparable measurements, before and after the electrochemical procedures. The cantilevers used are the Si-tips NSC15[4] where the backside is coated with Al to get a better reflectivity for the laser spot. For this cantilevers an averaged tip radius of 10 nm, a free eigenfrequency of 325 kHz and a spring constant of 40 N/m, are specified by the manufacturer. The piezo-scanner performing the lateral oscillations, is a vertical engage tube scanner with a maximum scanning range of 150 µm. For the AFM

---

[3]Digital Instruments: now Veeco Instruments (USA)
[4]MicroMash (USA)

measurement procedure the sample is placed on top of the piezo scanner. Subsequently, the tip mounted in its holder is fixed over the specimen face to face. The sample can now be approximated to the oscillating tip, until it touches the surface. The approximation works completely automized to preserve the tip geometry as well as the sample surface. Far away from the sample, the tip performs free oscillations. Close to the sample, the tip oscillations are influenced by the Van der Waals force (mentioned above). This can be used to adapt the approximation velocity by a feedback mechanism. The imaging capabilities are mainly restricted due to the geometry and the radius of the scanning tip. Therefore, the absolute resolution of the nano-structures scanned, is also limited. This might be the reason, why sub-structural resolution - on atomic scales - of the metamaterials topography has not been possible for this method under present conditions. Hence, structural surface investigation has been performed by SEM imaging with a nominally better- and more reproducible resolution. Nevertheless, it is possible to obtain a very good 3D topography map of several plasmonic objects and to get superior informations about geometrical conditions, especially the sample height which is a crucial geometrical parameter for our investigations.

6.2 Optical Characterisation

6.2.1 Optical Transmittance Spectroscopy

For the optical characterization of the metamaterial samples we use a normal incidence transmittance spectroscopy setup which has been built up in our group [142]. This setup offers a very small half opening angle for incident light of about 5° and the opportunity to perform angle-resolved as well as polarization-resolved measurements. It is an open coverage type setup, making it easy to modify the components and to adapt it to the required experimental needs. In Fig. 6.3 the measurement setup is sketched. The white light is delivered by a 100 W tungsten halogen bulb, emitting blackbody radiation with a surface temperature of about 3000 K. The lens L1 couples the light into a IR/VIS optical fiber with a 200 μm core. The lens L2 collimates the light emerging at the other end of the optical fiber. A Glan Thompson polarizer GT controls the linear polarization state of incident light and the subsequently arranged microscope objective ML1[5] focuses the light onto the sample. For measurements in air, the sample is mounted on a goniometer stage SH, which allows a strictly perpendicular alignment to the optical axis of the setup. Furthermore, it is possible to measure the sample under different incident angles. This sample mount can be replaced by a holder for the quartz glass cuvette, which is necessary to perform the transmittance measurements in the liquid electrolyte (compare section 6.2.2). By closing the aperture in front of the first microscope objective A1, it is possible to reduce the half opening angle of incident light to roughly 5°. The following microscope objective ML2, which is identical in construction to the former one, collects the light from the sample and collimates it again. Lens L3 in combination with the objective ML2 is used to image the sample to an intermediate image plane, where knife-edges KE are placed to spatially select the desired area of the sample surface. The

---

[5]Zeiss Achroplan LD 20x KO, NA=0.4
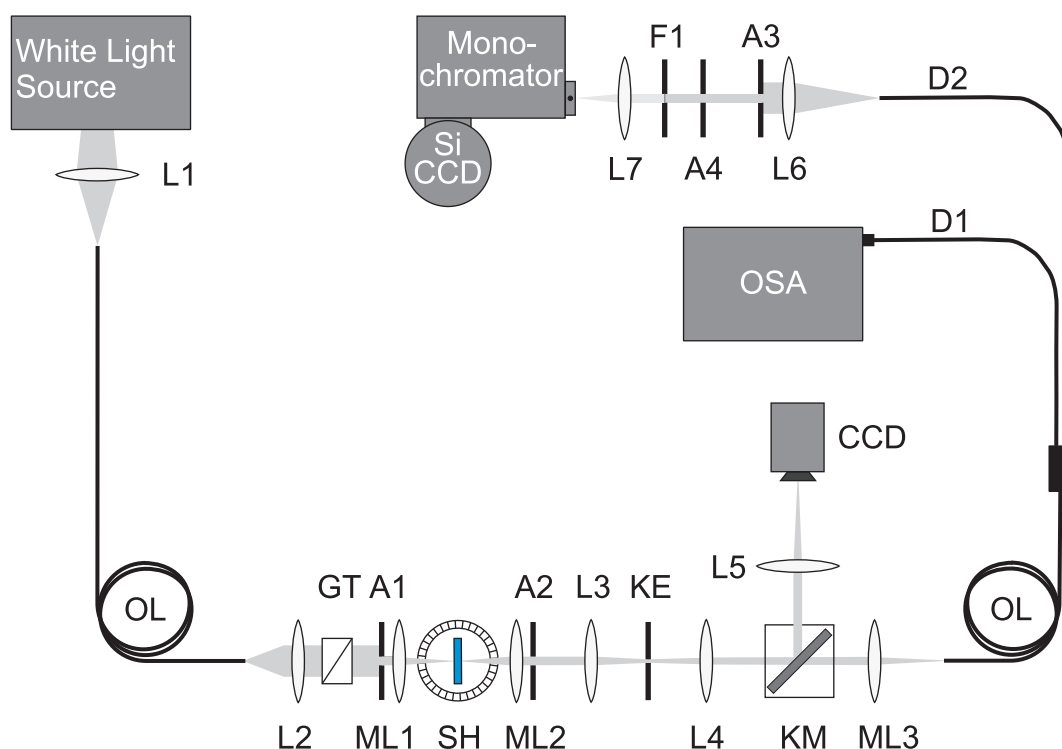
Figure 6.3: The setup for normal incidence and polarization-resolved transmittance measurements is illustrated. Light is focused onto the specimen with a fairly small opening angle. The transmitted light is re-imaged onto an intermediate image plane where knife-edges can be adjusted to select the sample area. This can be monitored by a CCD camera. For spectrally resolved detection, either an optical spectrum analyzer or a grating spectrometer connected to a CCD camera is used. L1: lens with f=50.2 mm; L2: lens with f=25.4 mm; GT: Glan-Thompson polarizer; A1, A2: apertures; ML1, ML2: microscope objectives (NA=0.4); L3, L4: lenses with f=150 mm; KE: knife-edge aperture; KM: kinematic mirror; ML3: microscope objective (NA=0.25); detection path D1: OSA: optical spectrum analyzer; L5: detection path D2: lens with f=500 mm; CCD: CCD camera; L6: lens with f=25.0 mm; A3, A4: apertures; filter F1: NG1, 1 mm; L7: lens with f=50.2 mm; monochromator; CCD (Si): silicon CCD camera.

selected area is finally imaged onto an IR/VIS optical fiber with a $200\,\mu m$ core using lens L4 and the microscope objective ML3[6]. The fiber is connected to the detection system, which is usually the commercially available optical spectrum analyzer OSA[7] with a spectral detection range from 500 nm to 1750 nm. An additional detection system is initialized to perform a long time optical monitoring, where a detailed description can be found in section 6.2.2. In order to align the sample with respect to the foci of the microscope objectives ML1 and ML2 and to adjust the knife-edge apertures in the intermediate image plane, the kinematic mirror KM can be placed into the optical path, to image the intermediate plane via lens L5 onto an infrared CCD camera [8].

---

[6]Newport M-10x, NA=0.25

[7]Ando AQ 6315 B (USA)

[8]Panasonic (USA)
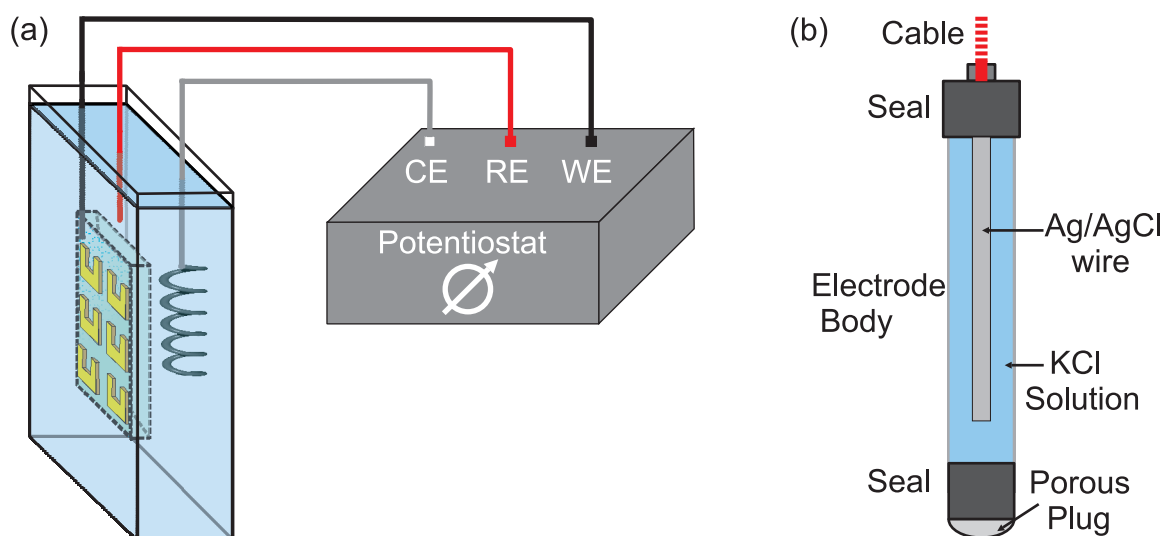
Figure 6.4: (a) Schematic Sketch of the fluid cell filled with a 0.7 M solution of NaF in ultra pure 18.2 MΩ cm grade water. In the electrolyte, the ITO coated suprasil substrate with the metamaterial structures on top, is immersed. The ITO surface combined with the gold metamaterial structures form the working electrode. The counter electrode is established by a macroscopic gold spiral. The reference electrode is immersed in the electrolyte solution close to the sample. All three electrodes are connected to a potentiostat which acts as a voltage source. (b) Schematic picture of the reference electrode consisting of a Ag wire coated with AgCl. This wire is placed in a slim and long capillary tube and immersed in KCl. A porous plug forms the contact to the environment with an extremely low leakage of KCl.

6.2.2 Optical Characterisation in electrolyte solution

To study the optical properties of the metamaterial samples in the electrochemical environment *in-situ*, it is necessary to modify the optical transmittance setup described in section 6.2.1. The sample holder with the goniometer is replaced by a liquid filled glass cuvette, which is the mount and the electrochemical environment for the metamaterial sample. To accommodate the fact, that the liquid in the cuvette changes the optical path, it is mandatory to realign the sample and the microscope objective ML1 along the optical axis. The metamaterial sample is immersed in the electrolyte solution and its potential is measured relative to a standard reference electrode (RE), which is controlled by a potentiostat (see Fig. 6.4). In this fashion we can reproducibly control the electrode potential and specify its value on an absolute scale. Optical spectra are recorded at constant potential, after the decay of the initial charging current transient. For this measurement we use detection line D1 with the optical spectrum analyzer OSA. The counter electrode is represented by a macroscopic gold spiral within the electrolyte. The aqueous solution is opaque in the near-infrared (i.e., for wavelengths larger than $1.4\,\mu m$, equivalent to frequencies below $214\,THz$). Hence, we have chosen the lateral dimensions of the single elements of the metamaterial such, that the resonances of interest are in the near-infrared part of the electromagnetic spectrum. In this case, this leads to side lengths for the used split-ring resonators on the order of $100\,nm$.

The Fluid-Cell   is the specimen mount and the electrochemical environment for the experiments. In Fig. 6.4 (a), the cell, the potentiostat and the connected electrodes are schematically sketched. The cell consists of a quartz glass body of the special spectroscopy glass BK 7[9]. A small mount on the bottom of the cell fixes the sample and the contact wire for the working electrode as well. The cell being open to the air is filled with a 0.7 M solution of NaF [10] in ultra pure 18.2 MΩ cm grade water[11]. This electrolyte composition is used for all electro-optical experiments discussed.

The Potentiostat   is the voltage source in our electrochemical experiments. The used equipment is the commercially available system Voltalab 50[12] with the control and analysis software VoltaMaster 4. This system is especially designed for electrochemical voltammetry (see section 4.1.3), the method we also use for investigation. This system is connected to three different electrodes, namely the so-called working electrode, the counter electrode and the reference electrode. The sample surface with the thin layer of ITO and the metamaterial structures on top forms the working electrode (compare 5.1.1). The ITO film on the surface of the glass sample is connected to a thin gold wire, which is trapped between the PTFE inset of the cuvette and the ITO layer on top of the sample. The counter electrode is represented by a macroscopic gold spiral, which delivers the flux of the charge carriers within the electrolyte. The reference electrode[13] is a commercially available slim and long capillary tube electrode filled with a saturated solution of KCl and a Ag wire coated with AgCl, surrounded by the electrolyte solution. The interior of the electrode is connected to the environment by a nano-porous plug on the bottom side. The manufacturer specifies an extremely low electrolyte leakage[14] for this device. This is important in order to prevent contamination of the fluid-cell by the reference electrode during the measurements. The configuration of the mentioned three electrodes is necessary to guarantee a geometrical independent and therefore reproducible measurement setup.

6.2.3   Time Resolved Optical Characterization in Electrolyte Solution

To understand the surface effects happening during the electrochemical procedure it is of utmost importance, to measure the spectral changes over the applied electrode potential and time. A slightly modified detection setup has been used for this measurement. This method allows a distinct investigation of reversible- and irreversible effects *in-situ* .

Extended Optical Transmittance Setup   Two different detection lines are used for the optical spectroscopy: line D1 with the optical spectrum analyzer OSA and a second line

---

[9]Ultra pure quartz glass with superior optical transmittance over the whole visible and infrared spectral range combined with excellent chemical resistivity properties

[10]Suprapur, Merck (Germany)

[11]Arium 611, Sartorius (Germany)

[12]PST050 Radiometer Analytical (France)

[13]Dry-Ref electrode, WPI (Germany)

[14]leakage less than $5.7 \cdot 10^{-8}$ ml/hr

D2 with a monochromator and a liquid nitrogen cooled Si-CCD camera. These detection lines are strictly used independently. Line D1 is actuated in a static mode. The spectra are taken after having applied a constant potential and the decay of the initial charging current transient. Line D2 is a monitoring system, tracking the spectral changes by a given externally applied potential over time. This detection method is of utmost importance to study the reversible as well as the irreversible effects occurring during the electrochemical procedures. As depicted in Fig. 6.3, this detection line is composed of the lens L6 collimating the light coming from the optical fiber. The following apertures A3 and A4 act as an alignment appliance for the optical beam path. The filter F1[15] reduces the incoming signal to prevent the CCD camera from an overload. Lens L7 focuses the light on the entrance slit of the monochromator (the slit aperture is set to $40 \, \mu$m). The grating used in the monochromator (300 lines per cm, blazed at $1.0 \, \mu$m) allows the resolution of the spectral range between 700 nm and 900 nm wavelength.

---

[15]NG3, Schott (Germany)

Chapter 7

Electrochemical Modulation

The field of metamaterials and photonics in general, is a very promising part of research putting forth novel technological concepts [6, 12]. How and whether these technologies will find their way into our daily lives, depends largely on making use of the properties these new kind of materials deliver and in transforming them into an application. Beside loss-compensation strategies (compare chapter 8), large scale manufacturing techniques [68] and the ability to control, tune or even modulate the optical material properties are of essential importance.

The astonishing properties delivered by metamaterials rely on resonances of typically metallic building blocks. A famous representative is the split-ring resonator [2] that can give rise to an effective magnetic response even at optical frequencies [14, 15]. As already discussed in chapter 3 the spectral characteristic of the underlying resonances are determined by the geometry of the resonators, the optical properties of the metal the metamaterial building blocks typically consist of and the composition of the dielectric environment in which the metamaterial is embedded.

To tune or even modulate the resonance characteristics, one must have the ability to change the above discussed factors, ideally by an external signal. Several different approaches following this goal have recently been discussed. Concerning the environmental change approaches using liquid-crystals [143–145], drops of silicon-nanospheres in ethanol solution [146], optically pumped silicon at THz frequencies [147], phase transitions in VO_2 [148, 149], and phase-change materials [150], have been presented.

Another approach is a structural tunability of split-ring resonators mediated by MEMS (Micro-Electro-Mechanical Systems), which has been presented for THz frequencies [151, 152].

An elegant way to affect the resonance properties of specifically metallic metamaterials is given by a direct modification of the metal's charge carrier density, influencing the optical properties of the constituting metals (compare section 2.2.2). Along these lines, field-effect-transistor like structures designed for far-infrared frequencies [20, 21], as well as for optical frequencies [153] have recently been discussed. A different approach suitable to induce charge carrier density changes in a metal, is simply given by a metallic electrode in an electrolyte (compare chapter 4). This phenomenon is well known in the electrochemistry community and has been investigated by reflectance measurements on bulk Au, Ag, and Cu

single-crystal surfaces [154–156].

Furthermore, optical modulation effects have been reported by a corresponding change of the charge carrier density influencing surface plasmon polaritons, excited within thin Au films [23]. Even particle plasmon resonance changes of about 4 % relative to its central resonance frequency within gold nano-crystals have been observed [22]. However, for bulk Au single-crystal surfaces, presented for instance in Ref. [156], the resulting optical modulation of the reflectance has been less than 1 %. The observed spectral shifts in case of surface plasmon polaritons have been similarely small [23]. In contrast, the optical modulation effects, which have been shown for chemically synthesized Au nano-crystals, manifest themselves by an impressive color change, which can be observed with the naked eye in dark-field microscopic images [22]. Considering these examples, the question arises, in which extent these modulation effects are related to the size scales of the underlying metallic nano- or bulk crystals. If there is a dependency, one has to figure out the relevant scaling parameters. Thus, it has not been clear at all whether an optical modulation induced by an electrochemical approach could be adapted to lithographically fabricated metallic metamaterials designed for optical frequencies, where the relevant feature sizes tend to be between the size for bulk-crystals on the one end and nano-crystals on the other end.

Moreover, the results obtained imply, that the surface-to-volume ratio plays a special role. This ratio can well be tailored by the geometrical conditions of the metamaterial building blocks, which also has been done in our case. These aspects distinguish our work on electro-modulation of photonic metamaterials reported in Ref. [70] from experiments incorporating Au nano-crystals or Au metal films. Moreover, we show that the resulting electrochemical modulation is surprisingly large and can well be controlled by both, the geometrical and the electrochemical conditions. Hence, the summary of the promising features presented, makes this approach very attractive for applications.

7.1   Experimental Results

Within this chapter we connect the findings given by the systematical analysis of irreversible gold surface restructuring presented in chapter 8 with reversible modulation effects of metallic metamaterials in a NaF-based electrolyte solution. The method of surface pre-processing is a crucial step for thin metal films, which exhibit significantly better modulation properties compared to thicker metal films. Thus, the pre-processing has been of utmost importance for the success of our work. The electrochemical modulation effects also show a partially irreversible character, which has been investigated. As an important result of the analysis we find, that the modulation amplitude scales reciprocal with the metal layer thickness d, reinforcing the assumption of surface charging effects as the relevant mechanism for the spectral modulations observed.
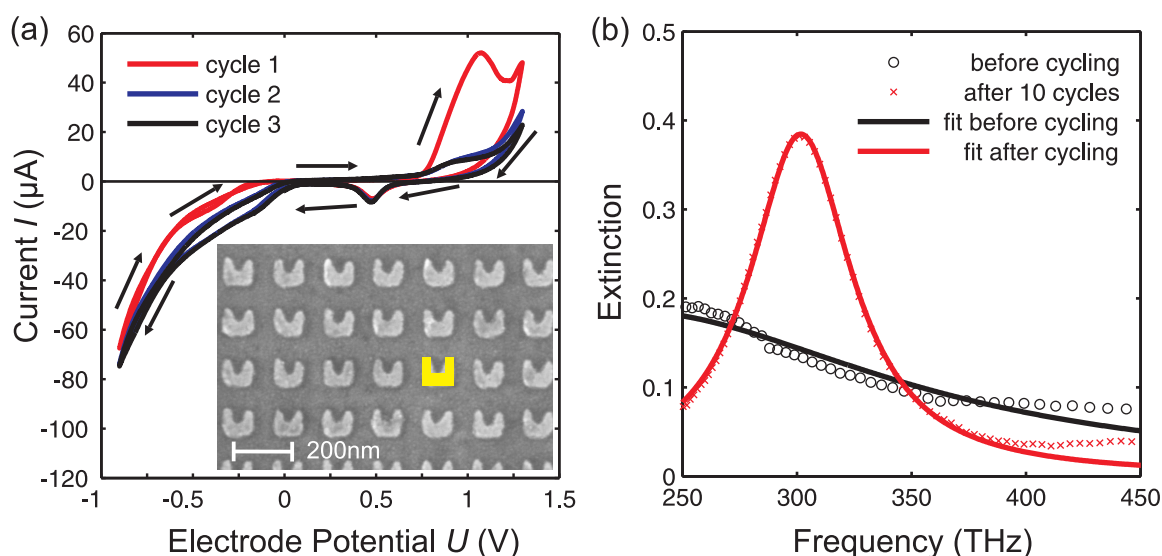
Figure 7.1: In (a) typical cyclic voltammograms of an array of 10-nm thin gold split-ring resonators in a NaF-based aqueous electrolyte for electrode potentials ranging from - 0.9 to + 1.3 V, are depicted. Scanning electron micrograph of the investigated structure is shown as inset. The artificial yellow resonator depicted, gives the dimensions used for numerical modeling. The first cycle is shown in red, the second in blue, and the third in black. Further cycles exhibit only minute changes and coincide within the line width of the curves. (b) Corresponding normal-incidence extinction spectra for vertical incident linear polarization of light and for open-circuit conditions before (black symbol) and after N=10 are depicted. One can see the enormous change of the line-width and resonance height which implies a significant reduction of damping. These results are qualitatively similar to the ones shown for nano-antennae in chapter 8 and [113].

7.1.1 Experimental Setup

We employ arrays of gold split-ring resonators in our electrochemical experiments [3]. Each array has a footprint of $80\,\mu m \times 80\,\mu m$. An example of a $10\,nm$ thin gold structure is shown in the inset in Fig. 7.1 (a). The split-ring resonator arrays have been fabricated using standard electron-beam lithography [3] on suprasil substrates coated with a $10\,nm$ thin film of indium tin oxide (ITO). The ITO avoids surface charging effects during the lithography and is additionally part of the working electrode within the electrochemical cell. After producing the template by lithography and a subsequent development process, a Cr layer of 2 to $3\,nm$ has been evaporated using a high-vacuum electron-beam evaporation chamber, which acts as adhesion promoter. Subsequently, the functional layer of Au has been evaporated. One obtains the final structure after a lift-off procedure. The average film thicknesses are determined by atomic-force microscopy. All relevant parameters and important intermediate steps in fabrication, not described in this short summary, can be found in chapter 5. The Cr adhesion promoter is necessary to guarantee reproducible results over long time electrochemical processing. Additional findings obtained from samples without Cr layer show results consistent to the ones obtained for the structures with Cr adhesion promoter. The major drawback of the samples without Cr adhesion layer are the insufficient durability of the samples, which tend to detach after repeated electrochemical cycling.

The electrochemical cell is a quartz glass cuvette filled with a NaF-based electrolyte, which

is open to air. The metamaterial sample is immersed in the solution and its potential is measured relative to a standard reference electrode (RE), which is controlled by a potentiostat. In this fashion we can reproducibly control the electrode potential and specify its value on an absolute scale. Optical spectra were recorded at constant potential after a transient decay of the initial charging current. We use a macroscopic gold spiral as the counter electrode within the electrolyte. Further information about parameters and the devices used, can be found in chapter 6. The aqueous electrolyte solution is opaque in the near-infrared (i.e. for wavelengths larger than $1.4\,\mu$m, equivalent to frequencies below $214\,$THz). Hence, we have chosen the split-ring resonator sizes such that the resonances of interest lie in the near-infrared part of the electromagnetic spectrum. This leads to split-ring resonator side lengths on the order of $100\,$nm [see inset in Fig. 7.1 (a)].

7.1.2   Measurements and Discussion

The electrochemical processes at the gold surface under the conditions, summarized in the short section given above, can be characterized based on cyclic voltammograms, which display the current I versus the electrode potential U, during cyclic potential scans [compare Fig. 7.1 (a)]. For comparison, the graph depicted in section 4.1.3 and the corresponding discussion, should be taken into account, as it facilitates to comprehend the following explanations. The most distinctive feature of the cyclic voltammogram is a peak at the positive end of the applied potential range that occurs only during the first scan [compare Fig. 7.1 (a)]. This peak does not appear for structures without the Cr adhesion layer (not depicted). Thus, this specific effect can be associated to a partially dissolution of Cr. In the subsequent cycles peaks in the potential range $U > 0$ correspond to oxidation and reversible adsorption and desorption of OH^- species, not exceeding one adsorbed monolayer. The large current appearing at $U < 0$ indicates Faraday reactions related to oxygen trace contaminants.

The corresponding extinction spectra are shown in Fig. 7.1 (b). The extinction is defined as the negative logarithm of the intensity transmittance. Thus, unity extinction corresponds to a suppression of the transmittance by one order of magnitude. The obtained extinction values within this experiment have been recorded with a transmittance setup under normal incidence of incoming light (described in section 6.2.1). The obtained spectra are normalized with respect to the bare ITO-coated suprasil substrate, i.e. without the Cr/Au nanostructures, in the same electrochemical cell. Hence, the optical properties of the electrochemical cell drop out and do not influence the optical investigations. The transmittance of the entire electrochemical cell is about 50 % and nearly constant over the entire investigated spectral range. This implies that the electrolyte absorption does not significantly affect the plasmonic damping.

The fully processed samples with the adhesion promoter and a 10-nm thin gold layer on top show only a very broad plasmonic resonance - in air as well as in the electrolyte solution (depicted in Fig. 7.1 (b) in black). In considering significantly high intrinsic electron scattering/damping within the evaporated metal layers, due to their expected large surface roughness and the influence of grain boundaries, these characteristics do not surprise.

However, after 10 electrochemical cycles over a range from - 0.9 V to +1.3 V a much more pronounced and sharper plasmonic resonance appears (compare Fig. 7.1 (b) red curve). These

findings are in very good agreement with the results presented in chapter 8, where the underlying nano-structures have a slightly different shape. However, it has to be noted again, that this procedure is especially pronounced for very thin metal films near or even below the percolation limit. For thicker gold films, the underlying plasmonic resonances exhibit lower damping even without initial electrochemical surface restructuring [3]. Nevertheless, even for thick gold films surface improvements accompanied by damping reductions of up to 30 % are possible [113].

For the case of split-ring resonators the measured extinction resonance centered at around 300 THz frequency in Fig. 7.1 (b) corresponds to a higher-order resonance of the split-ring resonators that can be excited for vertical incident linear polarization of light [3]. The measured extinction spectra can be well fitted by Lorentzians, providing us with the resonance position with an accuracy of ± 0.5 THz and the resonance damping given by the half-width-at-half-maximum. In Fig. 7.1 (b) the extracted damping reduces from more than 100 THz to 27 THz. We similarly follow the discussion presented in chapter 8 and tentatively assign the surface restructuring, to an enhanced mobility of gold atoms associated with a transient increase in surface diffusivity during lifting of the oxygen related adsorbate layer [103, 157] at the positive end of the potential scale. In the same manner, the pre-processed structures also reproducibly persist their improved optical properties after a removal from the electrolyte bath. This is a further evidence for the restructuring mechanism and implies, that this pre-processing also works for structures with extremely small feature sizes, which are given in this case down to approximately 32 nm.

Optical spectra are recorded for different potential values and after a constant transient-decay current. The resulting extinction spectra for three selected potential values, recorded within a complete cycle and for the largest electrode-potential window investigated ranging from - 0.9 V to + 1.3 V, are shown in Fig. 7.2 (a). For positive potential values the resonance exhibits a distinct red shift with respect to zero bias and a blue shift for negative potentials. The absolute spectral shift of the extinction peak, given for the most positive and negative potential value within one complete cycle, is as much as 55 THz, which is about 18 % of the center frequency or more than twice the damping for zero electrode potential given by 24 THz. Additional to the spectral shift, the resonance damping also varies for different applied potentials. It increases from 24 THz at $U = 0.05$ V to 31 THz at $U = +1.3$ V and to 36 THz at $U = -0.9$ V. Further extinction data for two complete cycles are shown as a false-color plot in Fig. 7.2 (b), where the corresponding potential profile is depicted on the left hand side. One can nicely follow the spectral resonace shifts by the given potential variation.

While the modulation of the gold surface-charge density is expected to be a reversible effect, the electrochemical surface restructuring as described above is clearly irreversible. It is also obvious from Fig. 7.2 (b) that the resonance position after two complete cycles does not exactly come back to its original position. This raises the question, which fraction of the 55 THz frequency shift in Fig. 7.2 (a) is reversible and which fraction is irreversible. To address this important question, we cycle the electrode potential several times for two smaller electrode-potential windows while observing the extinction spectra for similar samples. The resulting resonance positions, extracted from the Lorentzian fitting, are summarized in the
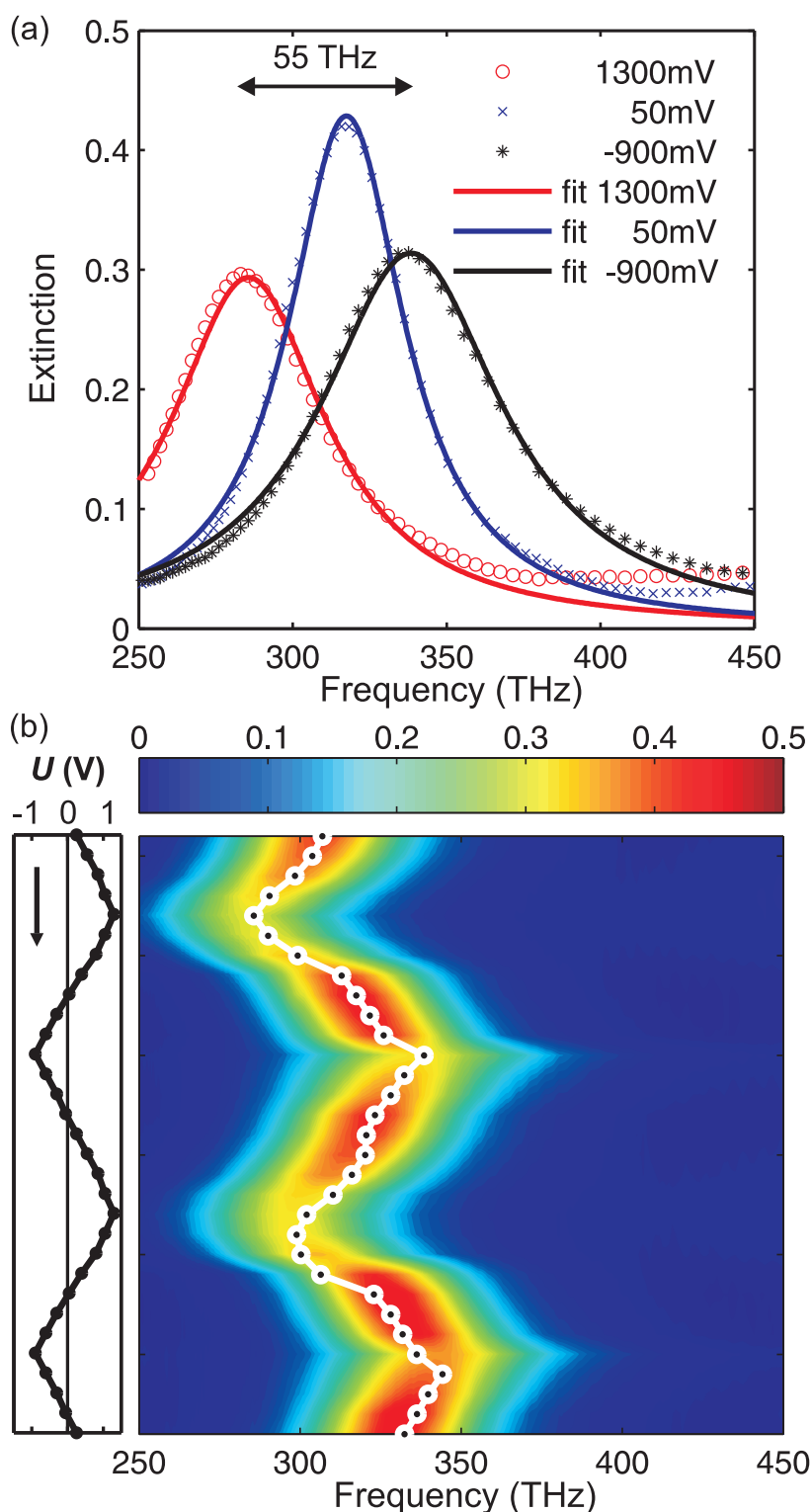
Figure 7.2: The electrode potential is varied within a window ranging from -0.9 to $+1.3$ V [compare Fig. 7.1 (a)]. (a) Three selected extinction spectra from one electrochemical cycle taken after N=10 cycles of pre-processing are depicted. The solid curves are Lorentzian fits to the data, the observed peak-to-peak frequency shift of 55 THz is indicated. (b) Further extinction spectra plotted on a false-color scale for two complete electrochemical cycles (2 hours acquisition time, time runs from top to bottom) under the same conditions as (a). The electrode potential varies as shown on the left-hand side; the dots correspond to the actually measured values. The white dots in the false-color plot indicate the resonance center frequencies as obtained from the Lorentzian fits.

left-hand side column of Fig. 7.3. The damping evolution is given in the right-hand side column. Subsequent to the usual 10-cycles of sample pre-processing, we start with a small electrode-potential window, ranging from - 0.5 V to + 0.9 V as shown in Fig. 7.3 (a). The three depicted complete cycles show only very small if any irreversible effects. Next, the electrode-potential window is increased to - 0.9 V to + 0.9 V in Fig. 7.3 (b). Obviously, the modulation shows a slightly hysteretic characteristic and exhibits a drift towards higher frequencies i.e., the resonance does not quite come back to the same position after one cycle. However, this irreversible part essentially saturates after another 100 cycles under the same conditions as shown in Fig. 7.3 (c). Here, we obtain reversible frequency shifts as large as 25 THz, still comparable to the resonance damping for zero electrode potential given by 35 THz for this sample. We assign the irreversible contributions to structural changes similar to those during the initial pre-processing procedure.

Furthermore, a qualitatively reversible modulation of the damping can be observed for the different displayed potential ranges. The amplitude of this modulation is most prominent for positive potential values compared to equilibrium. This effect can be explained with the desorption of, e.g. OH^- species occurring in the corresponding potential range. The desorption of these species tends to increase the electron scattering effects at the surface and therefore leads to an increase of the damping. This assumption is consistent with observations on chemisorption experiments of metallic nano-colloids [114].

To further test our interpretation of the effects observed, we have performed additional experiments, in which the gold film thicknesses of the split-ring resonators are varied systematically. Following our interpretations, we expect smaller reversible frequency shifts caused by surface-charge effects for thicker Au films due to the less favorable surface-to-volume ratio. Results of corresponding experiments are shown in Fig. 7.4. As expected, for a given voltage modulation within the reversible regime, the observed frequency shift decreases with increasing gold thickness d of the split-ring resonator, approximately proportional to $1/d$, describing the proportionality of the surface-to-volume ratio. Finally, the experimental observations are in good agreement with simple numerical modeling presented in section 7.1.3. Following the assumption, that the extra electronic charge is accomodated on the metal side of the double layer region (compare section 4.1.1), we modelled a charge increase as an increment of metal by maintaining the metal's free charge carrier density and *vice versa*.

7.1.3 Numerical Consistency Check

A recent density-functional-theory study of charged gold surfaces suggests that the potential variation affects the electron density exclusively within the topmost atomic layer at the surface [124]. Furthermore, the position of the image plane changes in good agreement with the notion of an electron liquid, in which the charge density is a constant and the extra charge is accommodated by an outward shift of the electron liquid. This motivates us to view the modulation of the metal's surface charge, naively, as an effective change of the split-ring resonators metal-film thickness. To support this reasoning and to investigate further influence factors, Sabine Essig has performed numerical calculations based on a scattering-matrix ap-
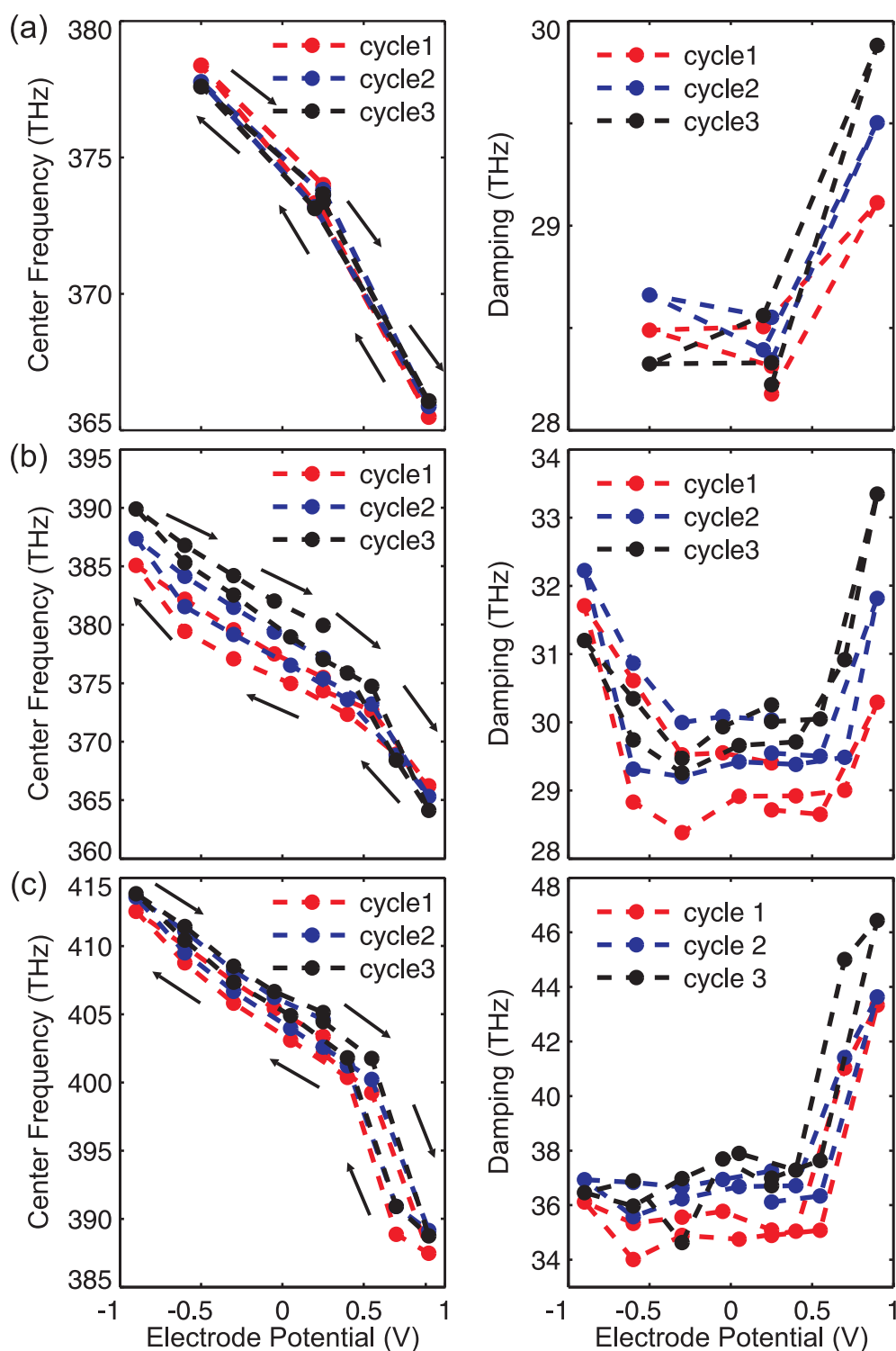
Figure 7.3: Split-ring-resonator resonance center frequency positions, left-hand side column, and damping given in the right-hand side columns, as obtained from Lorentzian fits to the measured data as depicted in Fig. 7.2 for three complete electrode-potential cycles in each sub-panel, (a) - (c) are depicted. The gold film thickness is 10 nm. (a) Electrode-potential window ranging from -0.5 V to +0.9 V and are recorded immediately after the original N=10 pre-processing cycles. (b) Following the measurements shown in (a) and for a larger electrode-potential window ranging from -0.9 V to +0.9 V. (c) Following (b) and an additional 100 cycles, i.e., N=110. Note that, for the conditions of (a) and (c) very nearly reversible electrochemical modulation of the optical resonance positions is obtained.
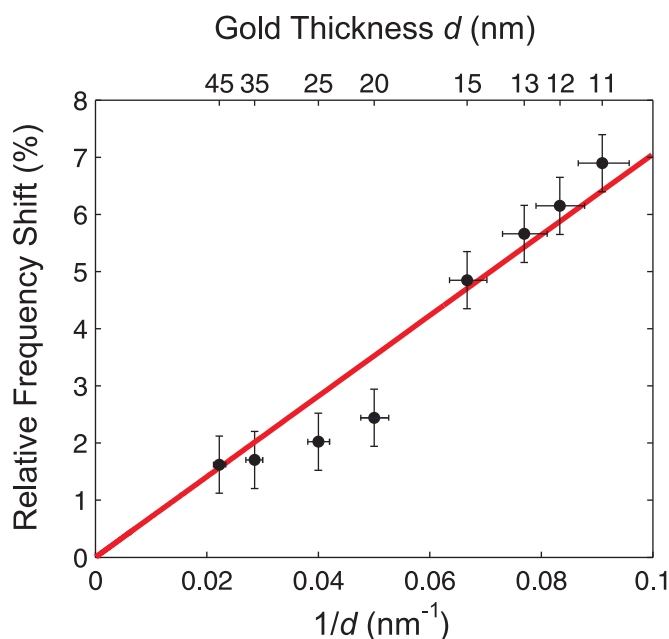
Figure 7.4: In this figure the relative split-ring-resonator resonance frequency modulation, i.e. the ratio of frequency shift and center frequency for zero electrode potential as obtained from Lorentzian fits to the measured data as in Fig. 7.2 versus the inverse, $1/d$ of the gold thickness, is depicted. In all cases, after the initial electrochemical pre-processing, the electrode-potential is varied in the range from - 0.9 V to + 0.9 V following N=100 electrochemical cycles. Obviously, the reversible modulation is more pronounced for thin gold structures due to their larger surface-to-volume ratio. The red graph is a straight line of best fit $1/d$.

proach, also known as Fourier Modal Method (FMM) or Rigorous Coupled Wave Analysis (RCWA). To allow for quantitatively reliable results for only minute changes in the system parameters, great care regarding convergence of the numerical results has to be exerted. As a matter of fact, we find that even for grid-aligned split-ring resonator structures only the use of adaptive coordinates, either in analytical form [158] or automatically generated [159], leads to converged results [70]. Within these calculations, the gold is described by the free-electron Drude model with a plasma frequency $\omega_{\mathrm{pl}} = 1.37 \times 10^{16} \mathrm{s}^{-1}$ and damping $\gamma_c = 1.2 \times 10^{14} \mathrm{s}^{-1}$. For simplicity, the ITO film and the Cr adhesion layer are neglected. The glass substrate refractive index is taken as 1.45.

The lateral dimensions of the split-ring resonators, as indicated in yellow within the inset of Fig. 7.1 (a), are given by the split-ring resonator footprint $110\,\mathrm{nm} \times 95\,\mathrm{nm}$, a side line width of $32\,\mathrm{nm}$, a bottom line width of $40\,\mathrm{nm}$ and a lattice constant of $180\,\mathrm{nm}$. The gold film thickness is $d = 10\,\mathrm{nm}$.

Based on these parameters, we find numerically, that a change in the split-ring resonators thickness by $1\,\mathrm{nm}$ (i.e., from $10\,\mathrm{nm}$ to $11\,\mathrm{nm}$) leads to a blue shift of the resonance of $12.3\,\mathrm{THz}$. The relative frequency shift decreases for thicker split-ring resonators like $1/d$. This behavior qualitatively reproduces our experimental observations.

In order to obtain the same blue shift of $12.3\,\mathrm{THz}$ for a fixed thickness of d=10 nm, the refractive index of the entire electrolyte would have to exhibit a large change from 1.33 to 1.24. Similarly, by modulating the index only within a 1-nm thin surface layer within the

electrolyte, the local index of this surface layer would need to decrease from 1.33 to 0.35. The refractive index can be modified for instance by changes in the pH-value of the electrolyte, which can be a result of the oxygen reduction reaction at the negative end of the potential scale. However, effects of this magnitude are hardly realistic in our experiments. Hence, these alternative mechanisms might play a certain role but they are quite unlikely to dominate in our experiments. A more detailed theory would have to treat the electrochemical processes at the gold surface on the atomic scale. This investigation might be within the scope of future work.

7.2 Conclusions

In conclusion we have shown that reversible tuning and modulation of plasmonic resonances in optical metamaterials is possible by an electrochemical approach. The reversible modulation- and irreversible tuning effects have well been cultivated and can be controlled by both, the electrochemical environment and the size parameters of the underlying metamaterial structures. Large frequency shifts of up to $55\,\mathrm{THz}$ have been gained. Systematic studies of the applied electrode potential allow for distinguishing between the irreversible fraction caused by the enhanced atomic surface diffusivity and the reversible fraction induced by charge carrier injections, leading to an increase of net electrons. This can be interpreted as an effective increase of the metal thickness. The assumption made has been suggested by density-functional-theory studies [124]. The reversible fraction of the frequency shift achieves a considerable value of $25\,\mathrm{THz}$, which is in the order of the resonance damping. Depending on the applied potential, the irreversible fraction is nearly absent for small potential variations and tends to decrease transiently for moderate applied potentials within a potential range of $-0.9\,\mathrm{V}$ to $+0.9\,\mathrm{V}$. This is in good agreement with the findings of chapter 8, where the surface diffusivity and the accompanied irreversible frequency shift also decays transiently for a similar potential range. It has been experimentally shown, that the relative frequency shift depends on the surface-to-volume ratio, which makes this effect scalable by the metamaterial thickness d. This trend has also been confirmed by numerical calculations. In addition, a qualitatively reversible damping modulation can be observed, which can be addressed to an enhanced electron scattering at surface adsorbates. This effect is present for all investigated potential ranges used. Moreover, further influence factors have been investigated within theoretical studies performed by an in-house FMM code. These studies have been done by Sabine Essig working in the group of Prof. Kurt Busch. Within these investigations we find, that influence factors given by a local refractive index change of the surrounding dielectric environment play a minor role. This aspect further confirms the assumption of charge carrier transfer to the split-ring surface as the underlying mechanism. The reversibility and the significant exhibitions of the effects observed make these assumptions very attractive for possible future applications concerning an actively tunable plasmonic device.

Chapter 8

Electrochemical Restructuring

The field of plasmonics and metallic photonic metamaterials is a very fast growing research area, and an important stimulus for the whole field of optics and nano-fabrication [2, 3, 8, 26, 54, 160]. However, important challenges have to be faced on the one hand given by technological fabrication limitation, but more importantly, on the other hand based on fundamental limitations. The most extensive fundamental limitation of these materials, is probably given by the intrinsic losses which are related to the metals the metamaterials typically consists of. Moreover, planar metamaterials designed for optical wavelength consist of metallic building blocks with typical thicknesses of less than $50\,\mathrm{nm}$. The electronic properties of these thin metal films differ from metal bulk properties. Here, a further loss increase mainly caused by electron scattering at grain boundaries and other finite size effects (compare section 2.2.3) is expected [39]. The investigation of the underlying loss mechanisms and the ambitious efforts to develop compensation strategies are an important part of research. Currently, two promising approaches are being pursued, which can be divided into two main routes:

  (i) Active loss reduction by introducing gain-materials.

  (ii) Passive loss reduction by improving the metal quality.

Regarding (i) several approaches have been published, generally aiming at a reduction of the losses by introducing gain-materials. By giving a selection only, works on using PbS quantum dots covering an array of split-ring resonators [161], introducing dye's as filling material within a fishnet-structure [17] and coupling arrays of split-ring resonators to an InGaAs single-quantum-well [162] have been presented. Concerning the approach of direct loss compensation by improving the quality of the metal films, experimental work comprises studies on metal alloys [163] and post-tempering of metal nano-structures [18] have been presented. Another route might be inspired by electrochemical processing of bulk metal electrodes, being a state of the art post-processing technique in electrochemistry [101, 109–112]. However, it is an enormous challenge to adopt this procedure to nano-scale metal objects, which has been presented for single gold nano-particles [164]. Electrochemical post-processing has also appeared as a side aspect in our work on electrochemical modulation experiments of

gold split-ring resonator arrays, presented in chapter 7 and [70]. Moreover, works on electrochemically mediated gold crystallization of nano-discs has been presented recently [165]. In this chapter we describe the systematical investigation of this aspect in terms of a post-processing procedure for gold nano-structures, that reduces the intrinsic losses under ambient conditions after electrochemical processing, compared to before. Within this investigation arrays composed of rectangular gold antennae have been used. We observe huge effects for film thicknesses near the percolation threshold and significant effects for typical gold-film thicknesses on the order of 20 - 30 nm [113]. It has to be noted, that post-processing of this kind is mainly expected to reduce excessive Ohmic (or non-radiative) damping. Small effects on the radiative damping may arise though, due to changes of the metal nano-structure shape. By assuming only minute changes of the antennae geometries, the intrinsic loss reduction is expected to be the dominating effect.

8.1 Experimental Results

In our electrochemical experiments on gold-based photonic metamaterials we have shown optical modulation. These effects are characterized by spectral- shifts and line-shape changes of the plasmonic resonances, which can be reversibly modulated by an external bias voltage (compare chapter 7 and [70]). In addition irreversible phenomena occurred leading to, inter alia, a reduction of the plasmonic damping. Here, we systematically study the latter aspect as a possible method of post-processing plasmonic gold nano-antennae arrays aiming at reduction of intrinsic losses in thin-metal nano-structures. We characterize the samples by optical spectroscopy, electron microscopy and atomic-force microscopy (compare chapter 6). For sub-10 nm gold thicknesses, the measured damping decreases by factors exceeding three. Even for 20 to 30- nm thin structures, the obtained loss reductions are still up to about 30 % (compare Fig. 8.3).

8.1.1 Setup Description

The gold nano-antennae arrays have been fabricated using standard electron-beam lithography on suprasil substrates coated with a 5- nm thin film of indium tin oxide (ITO) (compare section 5.1.1). As already discussed in chapter 5, the ITO film is crucial to avoid charging effects in the fabrication process. More importantly, the ITO combined with the nano-antennae arrays serve as the working electrode in our electrochemical experiments. In addition, we use a nominally 2- nm thin layer of Cr as adhesion promoter. All materials are deposited by standard high-vacuum electron-beam evaporation. Gold has been deposited at a rate of 0.1 nm/s. All quoted thicknesses have been measured by atomic-force microscopy (AFM). Each nano-antennae array has a footprint of $80\,\mu$m $\times$ $80\,\mu$m. Our electrochemical experiments have been performed in a quartz-glass cuvette filled with a 0.7 M solution of NaF in ultrapure $18.2\,\mathrm{M\Omega\,cm}$ grade water and open to air. All sample and electrode cleaning procedures can be found in more detail in chapter 6 and Ref. [122]. The sample is immersed in the solution and its potential is measured relative to a standard reference electrode (RE)
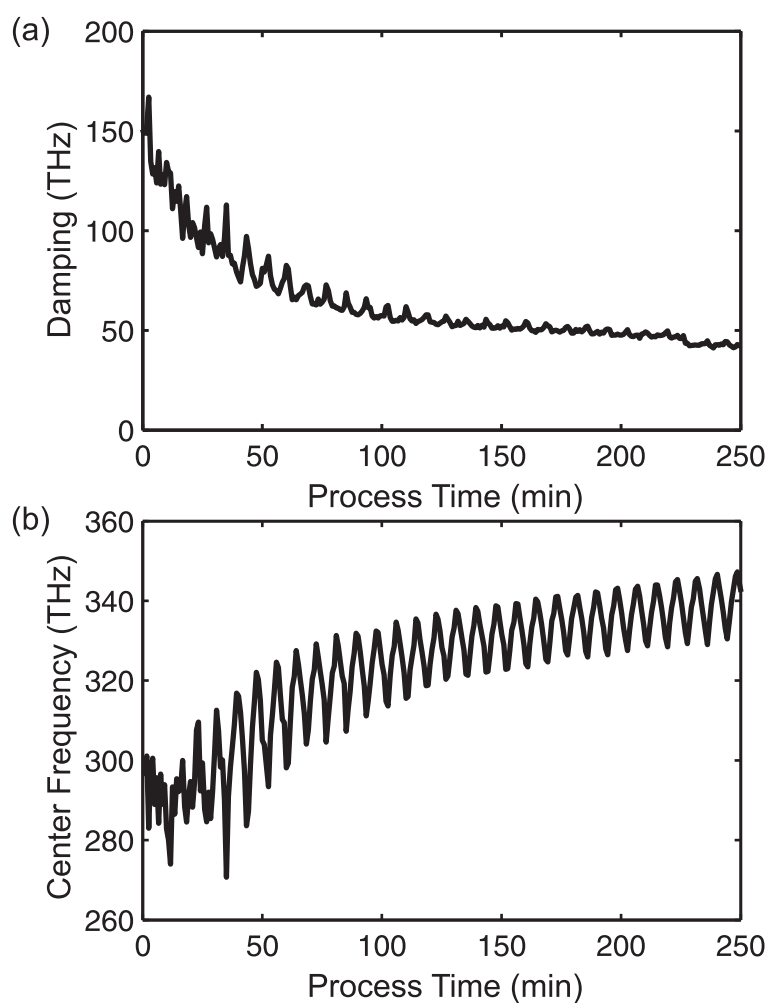
Figure 8.1: Plasmonic damping (a) and resonance center frequency (b) versus time as derived from Lorentzian fits to the measured extinction spectra taken under normal incidence with horizontal polarized light inside the electrolyte during periodic electrochemical cycling in the potential window from -0.9 V to +1.0 V and a cycling time of about 8 min per cycle. Note the beneficial reduction of damping (i.e., losses) versus time. The sample consists of an array of gold antennae with dimensions 145 nm × 95 nm, a lattice constant of 300 nm and an average gold film thickness of 7.9 nm.

Ag/AgCl in saturated KCl solution, which is controlled by a commercial potentiostat. A macroscopic gold spiral serves as the counter electrode in our setup. For the restructuring procedure the applied electrode potential has been varied between -0.9 V and +1.0 V for 30 complete cycles. This potential window includes the reversible adsorption/desorption of about one monolayer of oxygen on the gold surface.

8.1.2 Measurements and Discussion

To monitor the process in situ, we measure the normal incidence transmittance spectra as described in chapter 6 and [70]. The extinction spectra are the negative logarithm of the measured transmittance. All spectra (see Ref. [70] or right column of Fig. 8.2) can nicely be

fitted by Lorentzians. The resulting fit parameters (during cycling within the electrolyte), i.e., the damping and the resonance center frequency are depicted in Fig. 8.1. Clearly, the damping gradually decreases and the center frequency gradually shifts towards the blue. This effect can be phenomenologically explained by a decrease of the resistance and capacitance of the gold nano-structures due to surface restructuring. This can simply be understood in terms of a capacitor represented by the metal antennae. A decrease in surface corrugation leads to an increase of conductance caused by reduced elecron scattering within the antennae. Furthermore, a decrease of the capacitor surface reduces the capacitance. Superimposed on these trends, we again find electrochemical modulation of the transmittance within each cycle as previously discussed in chapter 7 and Ref. [70]. In terms of an electrochemical post-processing procedure, the comparison of the corresponding extinction spectra in air (rather than in the electrolyte) before and after the complete cycling are more relevant. Corresponding data are exhibited in the right column of Fig. 8.2 for the two orthogonal linear incident polarizations of light and for five different gold film thicknesses Fig. 8.2 (a)-(e). In each of these cases we find a substantial sharpening of the plasmonic resonances. As expected for any harmonic-oscillator resonance, this sharpening due to loss reduction is accompanied by an increase of the extinction peak height.

It is now interesting to ask whether these beneficial optical trends are accompanied by signatures in the electron micrographs or atomic-force micrographs (AFM) before (left column of Fig. 8.2) and after (center column) the complete electrochemical cycling.

To allow for a direct comparison and to obtain good image contrast, we have adjusted the gray levels in the electron micrographs such that the substrate on average appears black, whereas the gold antennae on average appear white. The resulting effects in Fig. 8.2 are most pronounced for thin "films" near or even below the percolation threshold. For example, a nominal gold film thickness of 7.1 nm, the disconnected islands of gold "before" cycling transforms into a film "after" the cycling. This trend is also accompanied by a slight reduction in the lateral extent of the metal pads. In contrast, the gold thickness as observed in the AFM data hardly changes between "before" and "after".

To emphasize this aspect, we show an AFM line scan through the center of the pad in each case. Note that the films after cycling appear much smoother in the SEM data. The AFM tip is obviously not able to reach into the steep valleys seen in the electron micrographs, which might be due to its large opening angle.

It has been reported that transient roughening, accompanied by an increase in surface diffusivity, accompanies the oxidation/reduction treatment of noble metal electrodes [112, 166]. In our experiments the "smoothening" only happened when we included oxidation/reduction potential window, and from the Lippmann equation it is known that in this potential window the gold-electrolyte surface tension is reduced [167]. The reduction of the surface tension of the gold-electrolyte interface favors wetting of the substrate by gold and, therefore, promotes a smoothening of the surface.

We conclude that the change in the optical properties is accompanied by a clear restructuring of the gold atoms within the antennae that is most pronounced for very thin films. This effects obviously the electron scattering processes within the metal antennae and leads to a reduction of dissipation which can be observed within the spectra by a change in the line
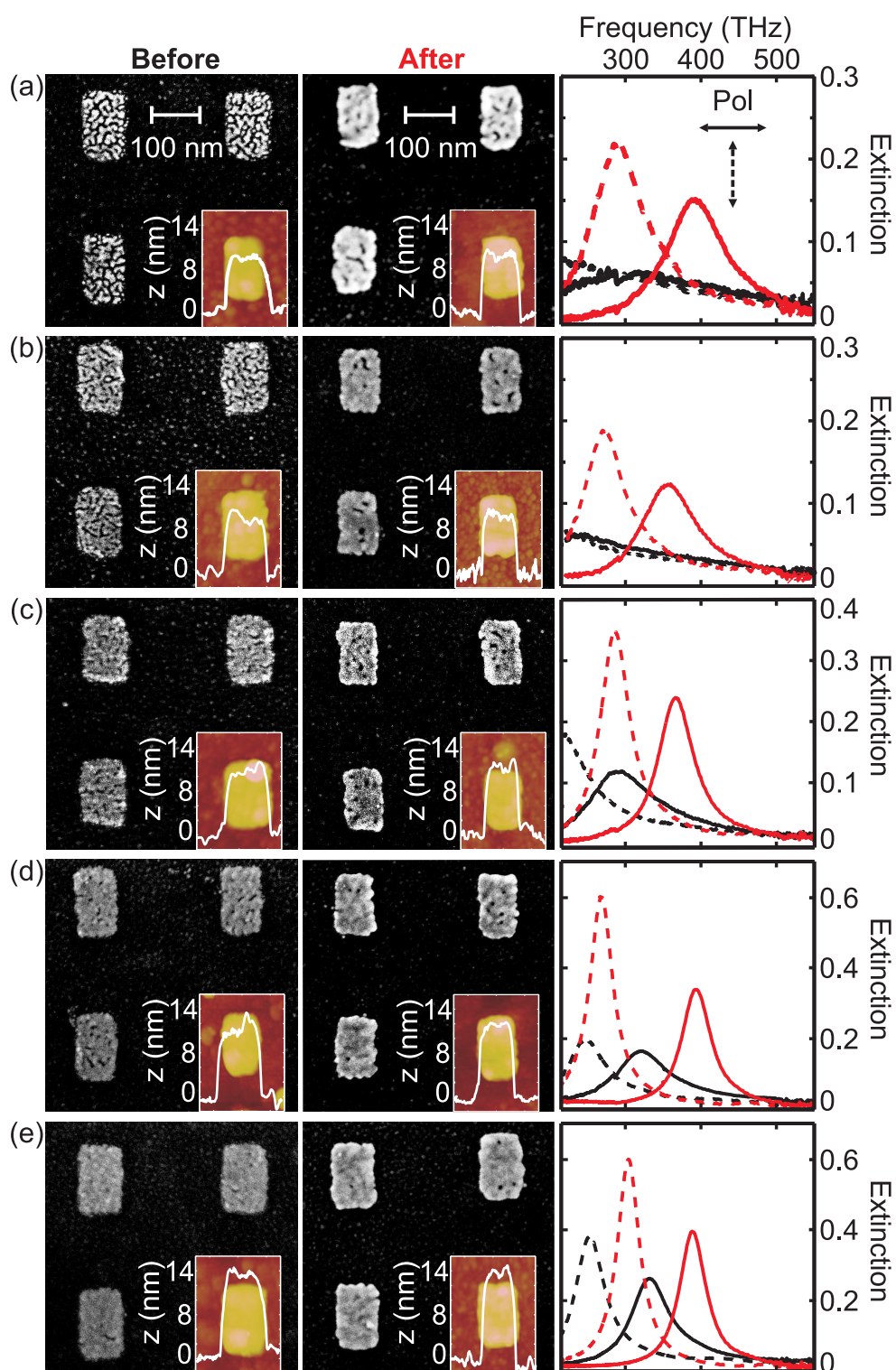
Figure 8.2: Gold nano-antennae arrays of different average gold film thickness (increasing from (a) to (e) with 7.1 nm, 7.9 nm, 8.6 nm, 9.8 nm, 11.5 nm) before and after electrochemical cycling (see Fig. 8.1). All data are taken under ambient conditions, i.e., outside of the electrolyte. The left column exhibits electron micrographs "before" cycling as well as AFM data on one antenna with an AFM line scan profile. The center column depicts corresponding data "after" cycling. Note the distinct changes in the spectra that are especially pronounced for thin gold structures. The right column reveals corresponding measured normal-incidence extinction spectra before (black curves) and after (red curves) cycling for vertical (dashed) and horizontal (solid) incident linear polarization of light.
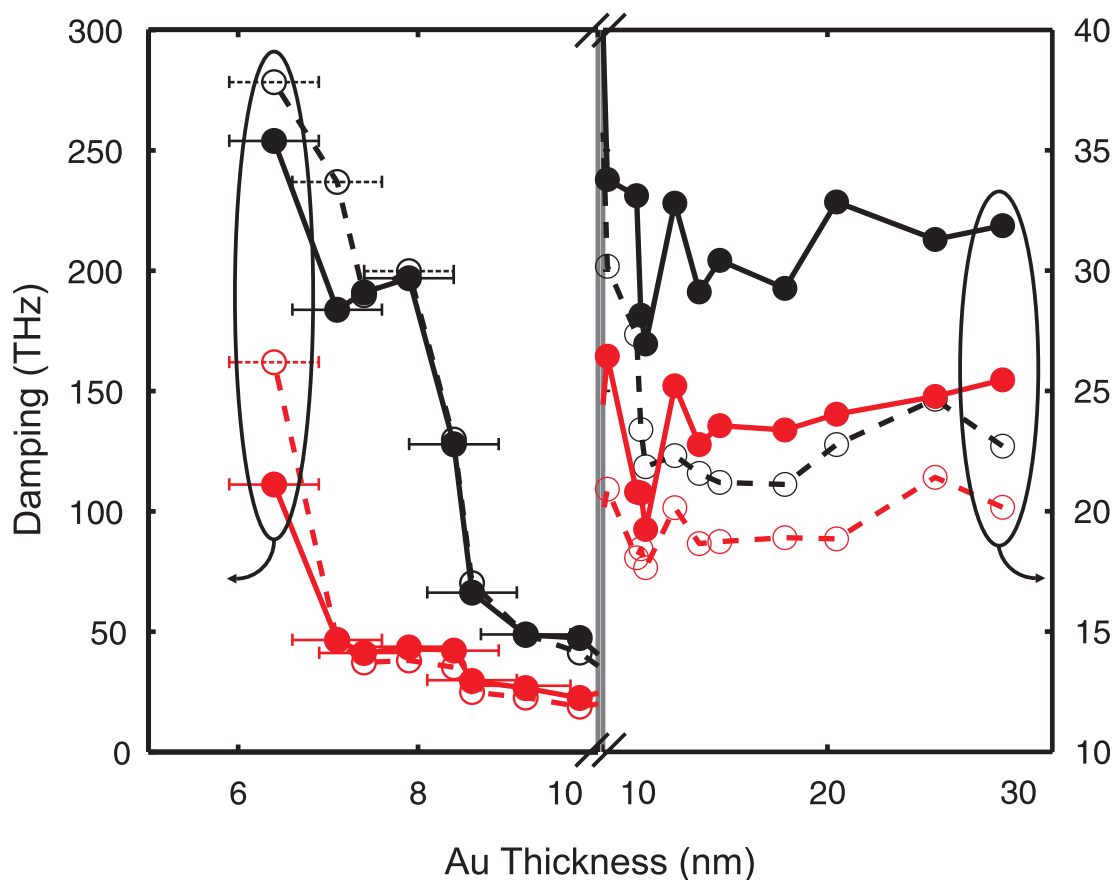
Figure 8.3: Plasmonic damping as derived from Lorentzian fits to measured extinction spectra like the ones shown in Fig. 8.2 "before" (black curves) and "after"(red curves) electrochemical cycling versus the average gold film thickness given in two different ranges: 6 nm to 10 nm in (a) and 10 nm to 30 nm in (b). Full symbols and solid lines correspond to horizontal linear polarization of the incident light, open symbols are connected with dashed lines to vertical polarization.

width of the resonance.

To give an overview on the results of our post-processing study, Fig. 8.3 summarizes the deduced damping values before and after the electrochemical cycling for all samples shown in Fig. 8.2 as well as for several others, especially others with much larger gold film thicknesses. Here, we find only insignificant changes within the electron micrographs. We estimated ± 0.5 nm for the errors of the AFM thickness measurement. The errors occurring for the Lorentzian fitting of the plasmonic resonances are assumed to be ± 0.5 THz and are within the line width of the graph. Obviously, the damping reduction decreases with increasing gold-film thickness. This trend is expected as one easily gains closed thick films by evaporation. However, we still get a damping reduction as large as 30 % even for 20 - 30 nm thick gold films. Such films are quite typical of photonic metamaterials [15]. These effects can be understood within the framework discussed in section 2.2.3. The metal thicknesses of 20 - 30 nm are in a regime, where surface improvements lead to prosumably significant changes within the electron scattering characteristics of the underlying metal film. By further increasing the metal film thicknesses far beyond the scale of the electron mean free path

in gold (estimated in 2.2.3 and [39]), the surface defect restructuring plays probably a minor role.

Much larger improvements can be reached for gold films below 10-nm thickness, since the fraction of unrestructured surface defects obviously increases for decreasing film thicknesses.

For completeness it must be noted that even for thick gold films the structure beneath the topmost gold layer, being in direct contact to the electrolyte, is not a completely homogeneous film. It consists of connected gold grains with typical grain sizes of about $15\,\mathrm{nm}$ [168]. These grain boundaries affect the electron scattering characteristics within the metal film. It is not expected, however, that this layer significantly influences the observed effect, since the direct contact to the electrolyte is not available.

8.2 Conclusions

In conclusion, we have presented electrochemical cycling as an alternative procedure of post-processing metallic photonic metamaterial samples. This approach aiming at loss reduction of plasmonic resonances is complementary to the recently discussed thermal annealing of photonic metamaterials [18]. Concerning a post-processing of thin metal films or nano-structures in general, this method is of conceptual advantage compared to state of the art thermal assisted post-processing techniques. This is due to the smooth surface treatment which is well controllable by the process parameters of the electrochemical treatment. Furthermore, different electrolytes can be used to adjust the surface diffusivity of the metals used within the electrochemical treatment (compare section 4.2.1 and [104]). In addition, extensive thermal stress phenomena, i.e. Rayleigh instabilities [117, 118], which have been observed in [18] for high aspect ratio structures, are presumably absent for this post-processing technique. By summarizing the obtained facts, it can be stated that the electrochemical post-processing is a universal and preservable method to increase the quality of nano-structures of presumably arbitrary shape and size.

Chapter 9

Conclusions and Outlook

In this thesis, we investigated electrochemically induced surface restructuring- and spectral modulation effects of planar metallic metamaterials. Our experiments contribute to the investigation of restructuring phenomena occurring on metal electrolyte interfaces, aiming a metal surface improvement with a corresponding reduction of metal intrinsic electron damping. Furthermore, the studies of charge transfer onto metallic photonic metamaterial structures, exhibiting astonishing optical modulation and tuning effects, which represent an important contribution to already established works in adjacent areas of research [20–23]. In the context of electrochemically manipulating the optical properties of metamaterials, new phenomena have been presented and the relevant mechanisms have been investigated within both, experimental and numerical studies.

The metamaterial samples have been fabricated using state-of-the-art electron beam lithography on functionalized quartz substrates. Subsequently, the resulting nano-structured templates have been metalized by evaporating gold layers of varying thicknesses under high-vacuum conditions. Before, an ultra thin layer of chromium has been evaporated under the same conditions to improve the adhesion of the gold layer within the electrochemical environment. A subsequent lift-off procedure provides us with high-quality metallic nano-structures with very small feature sizes down to $30\,\mathrm{nm}$ and varying metal layer thicknesses. The metamaterial structures have been investigated experimentally using electron-beam microscopy and atomic-force microscopy as well as optical transmittance spectroscopy in air and in a NaF-based aqueous electrolyte solution.

Within the field of metallic photonic metamaterials, a lot of effort has been spent on developing successful loss compensation strategies. This can be merged into two main routes following the concept of gain-material mediated, i.e. indirect loss compensation of metallic nano-structures on the one hand [17, 161, 162] and a direct strategy of loss compensation based on improving the optical properties of metal on the other hand [18, 163]. Promising work on using thermal annealing of gold nano-structures, leading to an improved morphology of the metal with accompanied positive effects on the optical properties, have been presented [18].

Inspiration for a new approach can be received within the field of electrochemistry and material sciences, where potential assisted and chemisorptive surface restructuring phenomena

are well known concerning bulk noble metal electrodes [101, 109–112]. To adopt a state-of-the-art restructuring technique, working for macroscopic bulk metal electrodes onto a system of periodically arranged metal objects with dimensions on the nanometer scale, is not self-evident.

Works on surface restructuring gold nano-spheres show encouraging surface improvements with a corresponding reduction of the extinction linewidth, implying a decrease of the intrinsic electron damping [164]. Our work deals with electrochemical induced surface restructuring phenomena of lithographically fabricated nano-structures. These metamaterials can be produced with a very high reproducibility and, concerning their expansion, they close the gap between single metal particles on the one end and bulk metal films on the other end. The surface improvement technique, presented in this thesis, gives the opportunity to restructure thin evaporated metal films even below the percolation threshold with very poor optical properties and to transform them into a closed metal film after the electrochemical treatment, accompanied by astonishing improvements within the optical properties. We reported damping improvements up to a factor of three for sub $10\,\mathrm{nm}$-thin gold films and even for thicker gold films of $30\,\mathrm{nm}$ the reduction of damping reaches remarkable values up to $30\,\%$. The damping reductions, based on optical extinction spectra measured within a transmittance spectroscopy setup and detected by a Si-CCD camera, can well be linked to structural modifications of the single metal objects, which have been investigated by electron-beam microscopy and atomic-force microscopy. The underlying restructuring meachanisms are consistent with those discribed for bulk metal electrodes [101] and the assumptions made have also been in line with theoretical works on metal restructuring phenomena [106]. Recently, similar observations, concerning nano-discs and holes have been presented, qualitatively confirming our work and presenting further interesting aspects [165].

It has to be noted, that the developed restructuring method has been of utmost importance for the electromodulation experiments, that has also been presented within this thesis. This is due to the fact, that the performance of the electrochemical modulation effects presented are sensitively dependent on the metamaterial layer thicknesses used for investigation.

This work incorporates itself as an important contribution into the overall context of actively manipulating the optical properties of plasmonic metamaterials. The astonishing optical effects, delivered by plasmonic metamaterials, typically rely on spectrally localized plasmonic resonances. The ability to tune or even modulate these resonances is an important step towards future applications.

Several different approaches concerning this topic have been presented recently. This includes the use of liquid-crystals [143–145], drops of silicon-nanospheres in ethanol solution [146], optically pumped silicon at THz frequencies [147], phase transitions in VO_2 [148,149] and phase-change materials [150]. These works rely on the concept of changing the resonance properties of the metal nano-structures by changing the surrounding dielectric environment.

Moreover, mechanical manipulating approaches have been presented [151, 152].

Another approach is a direct externally induced change of the materials optical properties by changing its charge carrier density. Works following this approach have shown significant effects even for optical frequencies [153]. In addition, metal semiconductor compounds

forming a field-effect-transistor like structures designed for far-infrared frequencies have been presented. Their working principle is based on a charge variation within the semiconductor influencing the optical properties of the compound [20, 21].

The goal to externally induce a charge carrier density change even within the metal, can be fulfilled by using an electrochemical approach as done in our case. The general feasibility of this method has been proven on a macroscopic scale by reflectance measurements on bulk Au, Ag and Cu single-crystal surfaces [154–156]. An influence on surface plasmon polaritons, excited within thin Au films, has also been reported [23]. On the other end of the size scale impressive color change phenomena, occurring for chemically synthesized Au nano-crystals, can be observed [22]. Our work, which is based on lithographically manufactured samples, is intermediate in size compared to these material systems. Therfore, it fulfills both, a completion by filling the size-gap and a clear distinction compared to already existent work.

The electromodulation experiments have been performed with samples of split-ring resonators immersed in a NaF-based aqueous electrolyte. Similar to the electrochemical restructuring measurements, a slightly different optical transmittance setup has been used. By investigating the obtained extinction spectra, we observed spectral shifts of the resonance center frequencies of up to $55\,\mathrm{THz}$, which is about $18\,\%$ of the center frequencies absolut values or more than twice the damping for zero electrode potential. Variations of different system parameters made it possible to distinguish between the reversible modulation effect, which we attribute to reversible surface charge density variations. In addition, an irreversible component has been observed, which can be connected to the context of electrochemical restructuring. The irreversible fraction of the spectral modulation decayed over time and we still obtained reversible spectral modulation reaching values up to $25\,\mathrm{THz}$. Furthermore, potential dependent qualitatively reversible damping variations have been observed. They are most prominent for positive potential values. These observations are qualitatively well consistent to chemisorption experiments incorporating nano-sized metal particles [114]. Here, the increase of damping has been addressed to surface adsorbates, being in our case most pronounced for the positive end of the used potential ranges.

The assumption, that the reversible spectral modulation depends on the surface-to-volume ratio of the underlying metal objects, was also confirmed by variing the metal thicknesses of the nano-structures.

Corresponding numerical calculations have been performed to review our interpretations. Within these calculations we approved the measured surface-to-volume dependency of the modulation effect by varying the gold layer thickness. A variation of the dielectric environment parameters implies, that the surface charging of the metal is presumably the relevant parameter mainly effecting the observed spectral modulation effects [70].

In summary, it can be stated, that the restructuring effect occurring to lithographically manufactured nano-structures is an important contribution, concerning the goal of reducing intrinsic metal losses by improving the surface properties. This method can be applied in terms of a post-processing technique for in principle arbitrarily shaped and ordered gold nano-structures. The works on metal electrode restructuring imply [101], that this method can also be extended to other materials, e.g. copper or silver, which are important for metamate-

rials, plasmonics and beyond [66, 92, 93]. Corresponding experiments on different materials should be investigated in further works.

The observed electrochemically induced spectral effects performed within an aqueous electrolyte exhibited encouraging reversible spectral tuning and modulation of the resonance frequency. The reversibility and the remarkable huge effects make this method interesting for an application. To further expand our method, works on replacing the aqueous electrolyte by solid electrolytes should be performed. This might be a step important for paving the way to create an optical device. This way can be assisted by applying other electrolytes. The influence of ionic species different from the ones used in our case, mediating the electro-modulation effects within metallic metamaterials, is still an open question.

Appendix A

Derivation of the Potential-Profile According to the GCS Theory

As briefly discussed in section 4.1.1 and following the derivations given in [97], the charge carrier population ratio within different slices i are given according to the Boltzmann equation by

$$n_i = n_i^0 \exp\left(\frac{-z_i e \Phi}{k_B T}\right).$$ (A.1)

With the population for all slices, we receive the charge distribution

$$\begin{aligned}
\rho(x) &= \sum_i n_i z_i e \\
&= \sum_i n_i^0 z_i e \exp\left(\frac{-z_i e \Phi}{k_B T}\right).
\end{aligned}$$ (A.2)

In electrostatics, the charge distribution is connected to the potential according the Poisson equation. By combining both, one obtains the Poission-Boltzmann equation given by

$$\begin{aligned}
\frac{d^2\Phi}{dx^2} &= -\frac{1}{\epsilon\epsilon_0}\rho(x) \\
&= -\frac{e}{\epsilon\epsilon_0}\sum_i n_i^0 z_i \exp\left(\frac{-z_i e \Phi}{k_B T}\right).
\end{aligned}$$ (A.3)

By using the identity

$$\frac{d^2\Phi}{dx^2} = \frac{1}{2}\frac{d}{d\Phi}\left(\frac{d\Phi}{dx}\right)^2,$$ (A.4)

we receive

$$d\left(\frac{d\Phi}{dx}\right)^2 = -\frac{2e}{\epsilon\epsilon_0}\sum_i n_i^0 z_i \exp\left(\frac{-z_i e \Phi}{k_B T}\right)d\Phi.$$ (A.5)

Integrating both sides, yields

$$\left(\frac{d\Phi}{dx}\right)^2 = -\frac{2k_BT}{\epsilon\epsilon_0}\sum_i n_i^0 \exp\left(\frac{-z_ie\Phi}{k_BT}\right) + \text{const.} \tag{A.6}$$

For distances far from the electrode surface we receive the constraints $\Phi = 0$ and $d\Phi/dx = 0$. This leads to

$$\left(\frac{d\Phi}{dx}\right)^2 = -\frac{2k_BT}{\epsilon\epsilon_0}\sum_i n_i^0 \left[\exp\left(\frac{-z_ie\Phi}{k_BT}\right) - 1\right]. \tag{A.7}$$

This relation can be simplified by assuming only one cationic and one anionic species. According to this assumption, one yields

$$\left(\frac{d\Phi}{dx}\right) = -\left(\frac{8k_BTn^0}{\epsilon\epsilon_0}\right)^{1/2}\sinh\left(\frac{ze\Phi}{2k_BT}\right), \tag{A.8}$$

while n^0 describes the ion concentration in the bulk solution and z the magnitude of the charge.
We obtain the potential profile along the given slices in x-direction by integrating Eq. (A.8) with the lower boundary Φ_0 for $x = 0$

$$\int_{\Phi_0}^{\Phi}\frac{d\Phi}{\sinh\left(\frac{ze\Phi}{2k_BT}\right)} = -\left(\frac{8k_BTn^0}{\epsilon\epsilon_0}\right)^{1/2}\int_0^x dx. \tag{A.9}$$

We end up with the final result given by

$$\frac{\tanh(ze\Phi/4k_BT)}{\tanh(ze\Phi_0/4k_BT)} = \exp\left(-\kappa x\right), \tag{A.10}$$

with

$$\kappa = \left(\frac{2n^0z^2e^2}{\epsilon\epsilon_0k_BT}\right)^{1/2}. \tag{A.11}$$

For large Φ_0, the potential decreases rapidly. For smaller Φ_0 the decrease becomes more gradual. Thus, we can make the assumption that for sufficiently small values of Φ_0, the approximation $(ze\Phi_0/4k_BT) < 0.5$ is valid. Then $\tanh(ze\Phi/4k_BT) \approx ze\Phi/4k_BT$. The potential drop is then given by the already stated relation (compare Eq. (4.3))

$$\Phi = \Phi_0 \cdot \exp(-\kappa x). \tag{A.12}$$

With respect to the finite dimension of the solvated ions, we have to extend the Gouy-Chapman derivation with a small but important modification made by Stern [100]. This is due to the fact, that the closest approximation of the ions to the electrode surface is given

by the radii of the solvated ions. Therefore we have to modify the boundaries of the integrals (compare Eq. (A.9)) to

$$\int_{\Phi_2}^{\Phi} \frac{d\Phi}{\sinh\left(\frac{ze\Phi}{2K_BT}\right)} = -\left(\frac{8k_BTn^0}{\epsilon\epsilon_0}\right)^{1/2} \int_{x_2}^{x} dx.$$

(A.13)

By integrating the former equation one obtains

$$\frac{\tanh(ze\Phi/4k_BT)}{\tanh(ze\Phi_0/4k_BT)} = \exp\left(-\kappa(x - x_2)\right).$$

(A.14)

where x_2 defines the plane of closest approach, which is in other words the outer Helmholtz plane (OHP). According to x_2, Φ_2 defines the potential at the same point. While the charge density in the region between the electrode surface and the OHP is zero, we receive a linear profile within this layer. The total potential drop across the double layer region is then given by

$$\Phi_0 = \Phi_2 - \left(\frac{d\Phi}{dx}\right)_{x=2} x_2.$$

(A.15)

Bibliography

[1] V. G. Veselago, *The Electrodynamics of Substances with Simultaneously Negative Values of ϵ and μ.*, Sov. Phys. Usp. **10**, 509 (1968).

[2] J. B. Pendry, A. J. Holden, D. J. Robbins, and W. J. Stewart, *Magnetism from Conductors and Enhanced Nonlinear Phenomena*, IEEE Trans. on Microwave Theory Tech. **47**, 2075 (1999).

[3] S. Linden, C. Enkrich, M. Wegener, J. F. Zhou, T. Koschny, and C. M. Soukoulis, *Magnetic Response of Metamaterials at 100 Terahertz*, Science **306** (5700), 1351 (2004).

[4] G. Dolling, M. Wegner, C. M. Soukoulis, and S. Linden, *Negative-Index Metamaterial at 780 nm Wavelength*, Opt. Lett. **32**, 53 (2007).

[5] U. Leonhardt, *Optical Conformal Mapping*, Science **312** (5781), 1777 (2006).

[6] J. B. Pendry, D. Schurig, and D. R. Smith, *Controlling Electromagnetic Fields*, Science **312** (5781), 1780 (2006).

[7] D. Schurig, J. J. Mock, B. J. Justice, S. A. Cummer, J. B. Pendry, A. F. Starr, and D. R. Smith, *Metamaterial Electromagnetic Cloak at Microwave Frequencies*, Science **314** (5801), 977 (2006).

[8] W. Cai, U. K. Chettiar, A. V. Kildishev, and V. M. Shalaev, *Optical Cloaking with Metamaterials*, Nature Photon. **1**, 224 (2007).

[9] J. Valentine, J. Li, T. Zentgraf, G. Bartal, and X. Zhang, *An Optical Cloak made of Dielectrics*, Nat. Mater. **8**, 568 (2009).

[10] L. H. Gabrielli, J. Cardenas, C. B. Poitras, and M. Lipson, *Silicon Nanostructure Cloak Operating at Optical Frequencies*, Nature Photon. **3**, 461 (2009).

[11] Y. G. Ma, C. K. Ong, T. Tyc, and U. Leonhardt, *An Omnidirectional Retroreflector Based on the Transmutation of Dielectric Singularities*, Nat. Mater. **8**, 639 (2009).

[12] J. B. Pendry, *Negative Refraction Makes a Perfect Lens*, Phys. Rev. Lett. **85**, 3966 (2000).

[13] N. Fang, H. Lee, C. Sun, and X. Zhang, *Sub–Diffraction-Limited Optical Imaging with a Silver Superlens*, Science **308** (5721), 534 (2005).

[14] V. M. Shalaev, *Optical Negative-Index Metamaterials*, Nature Photon. **1** (1), 41 (2007).

[15] C. M. Soukoulis, S. Linden, and M. Wegener, *Negative Refractive Index at Optical Wavelengths*, Science **315** (5808), 47 (2007).

[16] P. B. Johnson and R. W. Christy, *Optical Constants of the Noble Metals*, Phys. Rev. B **6** (12), 4370 (1972).

[17] S. Xiao, V. P. Drachev, A. V. Kildishev, X. Ni, U. K. Chettiar, H.-K. Yuan, and V. M. Shalaev, *Loss-free and active optical negative-index metamaterials*, Nature **466** (7307), 735 (2010).

[18] K.-P. Chen, V. P. Drachev, J. D. Borneman, A. V. Kildishev, and V. M. Shalaev, *Drude Relaxation Rate in Grained Gold Nanoantennas*, Nano Lett. **10** (3), 916 (2010).

[19] M. W. Klein, C. Enrich, M. Wegener, C. M. Soukoulis, and S. Linden, *Single-Slit Split-Ring Resonators at Optical Frequencies: Limits of Size Scaling*, Opt. Lett. **31**, 1259 (2006).

[20] H.-T. Chen, W. J. Padilla, J. M. O. Zide, A. C. Gossard, A. J. Taylor, and R. D. Averitt, *Active Terahertz Metamaterial Devices*, Nature **444** (7119), 597 (2006).

[21] H.-T. Chen, W. J. Padilla, M. J. Cich, A. K. Azad, R. D. Averitt, and A. J. Taylor, *A metamaterial solid-state terahertz phase modulator*, Nature Photon. **3** (3), 148 (2009).

[22] C. Novo, A. M. Funston, A. K. Gooding, and P. Mulvaney, *Electrochemical Charging of Single Gold Nanorods*, Journal of the American Chemical Society **131** (41), 14664 (2009).

[23] J. C. Abanulo, R. D. Harris, P. N. Bartlett, and J. S. Wilkinson, *Waveguide Surface Plasmon Resonance Sensor for Electrochemically Controlled Surface Reactions*, Appl. Opt. **40** (34), 6242 (2001).

[24] J. D. Jackson, *Classical Electrodynamics* (John Wiley & Sons, Inc., 1998), 3$^{\text{rd}}$ edition.

[25] C. E. Kriegler, M. S. Rill, S. Linden, and M. Wegener, *Bianisotropic Photonic Metamaterials*, Selected Topics in Quantum Electronics, IEEE Journal of DOI - 10.1109/JSTQE.2009.2020809 **16** (2), 367 (2010).

[26] M. Decker, M. Ruther, C. E. Kriegler, J. Zhou, C. M. Soukoulis, S. Linden, and M. Wegener, *Strong optical activity from twisted-cross photonic metamaterials*, Opt. Lett. **34** (16), 2501 (2009).

[27] L. Novotny and B. Hecht, *Principles of Nano-Optics* (Cambridge University Press, 2007).

[28] J. Kästel and M. Fleischhauer, *Quantum Electrodynamics in Media with Negative Refraction*, Laser Phys. **15**, 135 (2005).

[29] E. Hecht, *Optik* (Oldenbourg Verlag, 2005).

[30] L. D. Landau and E. M. Lifschitz, *Elektrodynamik der Kontinua* (Akademie-Verlag Berlin, 1985).

[31] H. A. Lorentz, *Über die Beziehung zwischen der Fortpflanzungsgeschwindigkeit des Lichtes und der Körperdichte*, Ann. Phys. **9**, 641 (1880).

[32] M. Born and E. Wolf, *Principles of Optics* (Cambridge University Press, 1999), 7$^{\text{th}}$ edition.

[33] P. Drude, *Zur Elektronentheorie der Metalle*, Ann. Phys. **306**, 566 (1900).

[34] N. E. Christensen and B. O. Seraphin, *Relativistic Band Calculations and the Optical Properties of Gold*, Phys. Rev. B **4**, 3321 (1971).

[35] P. G. Etchegoin, E. C. Le Ru, and M. Meyer, *An analytic model for the optical properties of gold*, J. Chem. Phys. **125** (16), 164705 (2006).

[36] C. Kittel, *Einführung in die Festkörperphysik* (Wiley&Sons, Inc., 2005), 14$^{\text{th}}$ edition.

[37] N. W. Ashcroft and D. N. Mermin, *Festkörperphysik* (Oldenbourg Wissenschaftsverlag, 2007), 3$^{\text{rd}}$ edition.

[38] A. Sommerfeld, *Zur Elektronentheorie der Metalle auf Grund der Fermischen Statistik*, Zeitschrift für Physik A Hadrons and Nuclei **47**, 43, 10.1007/BF01391055 (1928).

[39] E. H. Sondheimer, *The mean free path of electrons in metals*, Advances in Physics **50** (6), 499 (2001).

[40] A. Kaser and E. Gerlach, *Scattering of conduction electrons by interface roughness in semiconductor heterostructures*, Z. Phys. B **98**, 207, 10.1007/BF01324526 (1995).

[41] S. A. Maier, *Plasmonics: Fundamentals and Applications* (Springer Science, 2007).

[42] L. Solymar and E. Shamonina, *Waves in Metamaterials* (Oxford University Press, 2009).

[43] A. Otto, *Excitation of Nonradiative Surface Plasma Waves in Silver by the Method of Frustrated Total Reflection*, Z. Phys. **216**, 398 (1968).

[44] E. Kretschmann and H. Raether, *Radiative Decay of Nonradiative Surface Plasmons Excited by Light*, Z. Naturforsch. A **23**, 2135 (1968).

[45] R. B. Pettit, S. Silcox, and R. Vincent, *Measurement of Surface-Plasmon Dispersion in Oxidized Aluminum Films*, Phys. Rev. B **11**, 3116 (1975).

[46] U. Kreibig and M. Vollmer, *Optical Properties of Metal Clusters*, Springer Series in Materials Science 25 (Springer-Velag, 1995).

[47] R. Ruppin, *Plasmon Frequencies of Cube Shaped Metal Clusters*, Z. Phys. D **36**, 69 (1996).

[48] H. S. Zhou, I. Honma, H. Komiyama, and J. W. Haus, *Controlled Synthesis and Quantum-Size Effect in Gold-Coated Nanoparticles*, Phys. Rev. B **50**, 12052 (1994).

[49] R. D. Averitt, D. Sarkar, and N. J. Halas, *Plasmon Resonance Shifts of Au-Coated Au_2S Nanoshells: Insight into Multicomponent Nanoparticle Growth*, Phys. Rev. Lett. **78**, 4217 (1997).

[50] S. Zhang, W. J. Fan, N. C. Panoiu, K. J. Malloy, R. M. Osgood, and S. R. J. Brueck, *Experimental Demonstration of Near-Infrared Negative-Index Metamaterials*, Phys. Rev. Lett. **95** (13), 137404 (2005).

[51] C. F. Bohren and D. R. Huffman, *Absorption and Scattering by Small Particles* (John Wiley & Sons, Inc., 1983).

[52] G. Mie, *Beiträge zur Optik trüber Medien, speziell kolloidaler Metallösungen*, Ann. Phys. **25**, 377 (1908).

[53] G. Dolling, M. Wegener, and S. Linden, *Realization of a Three-Functional-Layer Negative-Index Photonic Metamaterial*, Opt. Lett. **32**, 551 (2007).

[54] J. Valentine, S. Zhang, T. Zentgraf, E. Ulin-Avila, D. A. Genov, G. Bartal, and X. Zhang, *Three-Dimensional Optical Metamaterial with a Negative Refractive Index*, Nature **455**, 376 (2008).

[55] G. Dolling, *Design, Fabrication, and Characterization of Double-Negative Metamaterials for Photonics*, Ph.D. thesis, University of Karlsruhe (TH) (2007).

[56] Y. Zhang, B. Fluegel, and A. Mascarenhas, *Total Negative Refraction in Real Crystals for Ballistic Electrons and Light*, Phys. Rev. Lett. **91** (15), 157404 (2003).

[57] X. L. Chen, M. He, Y.-X. Du, W. Y. Wang, and D. F. Zhang, *Negative refraction: An intrinsic property of uniaxial crystals*, Phys. Rev. B **72** (11), 113111 (2005).

[58] P. S. J. Russell, *Interference of integrated Floquet-Bloch waves*, Phys. Rev. A **33** (5), 3232 (1986).

[59] R. Zengerle, *Light Propagation in Singly and Doubly Periodic Planar Waveguides*, Journal of Modern Optics **34** (12), 1589 (1987).

[60] H. Shin and S. Fan, *All-Angle Negative Refraction for Surface Plasmon Waves Using a Metal-Dielectric-Metal Structure*, Phys. Rev. Lett. **96** (7), 073907 (2006).

[61] J. Chen, Y. Wang, B. Jia, T. Geng, X. Li, L. Feng, W. Qian, B. Liang, X. Zhang, M. Gu, and S. Zhuang, *Observation of the inverse Doppler effect in negative-index materials at optical frequencies*, Nat Photon **advance online publication**, (2011).

[62] G. Dolling, C. Enkrich, M. Wegener, C. M. Soukoulis, and S. Linden, *Simultaneous Negative Phase and Group Velocity of Light in a Metamaterial*, Science **312** (5775), 892 (2006).

[63] R. Merlin, *Analytical Solution of the Almost-Perfect-Lens Problem*, Appl. Phys. Lett. **84**, 1290 (2004).

[64] J. B. Pendry, A. J. Holden, W. J. Stewart, and I. Youngs, *Extremely Low Frequency Plasmons in Metallic Mesostructures*, Phys. Rev. Lett. **76**, 4773 (1996).

[65] R. A. Shelby, D. R. Smith, and S. Schultz, *Experimental Verification of a Negative Index of Refraction*, Science **292**, 77 (2001).

[66] G. Dolling, C. Enkrich, M. Wegener, C. M. Soukoulis, and S. Linden, *Low-Loss Negative-Index Metamaterial at Telecommunication Wavelengths*, Opt. Lett. **31** (12), 1800 (2006).

[67] S. Linden, M. Decker, and M. Wegener, *Model System for a One-Dimensional Magnetic Photonic Crystal*, Phys. Rev. Lett. **97**, 083902 (2007).

[68] N. Feth, C. Enkrich, M. Wegener, and S. Linden, *Large-Area Magnetic Metamaterials via Compact Interference Lithography*, Opt. Express **15**, 501 (2007).

[69] P. Mulvaney, J. Perez-Juste, M. Giersig, L. M. Liz-Marzan, and C. Pecharroman, *Drastic Surface Plasmon Mode Shifts in Gold Nanorods Due to Electron Charging*, Plasmonics **1** (1), 61 (2006).

[70] L.-H. Shao, M. Ruther, S. Linden, S. Essig, K. Busch, J. Weissmüller, and M. Wegener, *Electrochemical Modulation of Photonic Metamaterials*, Adv. Mater. **22** (45), 5173 (2010).

[71] J. Zhou, T. Koschny, M. Kafesaki, E. N. Economou, J. B. Pendry, and C. M. Soukoulis, *Saturation of the Magnetic Resonance of Split-Ring Resonators at Optical Frequencies*, Phys. Rev. Lett. **95**, 223902 (2005).

[72] A. Ishikawa, T. Tanaka, and S. Kawata, *Negative Magnetic Permeability in the Visible Light Region*, Phys. Rev. Lett. **95** (23), 237401 (2005).

[73] J. Schneider, H. and P. Dullenkopf, *Slotted tube resonator: A new NMR probe head at high observing frequencies*, Rev. Sci. Instrum. **48** (1), 68 (1977).

[74] W. N. Hardy and L. A. Whitehead, *Split-ring resonator for use in magnetic resonance from 200–2000 MHz*, Rev. Sci. Instrum. **52** (2), 213 (1981).

[75] B. T. Ghim, G. A. Rinard, R. W. Quine, S. S. Eaton, and G. R. Eaton, *Design and Fabrication of Copper-Film Loop-Gap Resonators*, Journal of Magnetic Resonance, Series A **120** (1), 72 (1996).

[76] W. J. Padilla, A. J. Taylor, C. Highstrete, M. Lee, and R. D. Averitt, *Dynamical Electric and Magnetic Metamaterial Response at Terahertz Frequencies*, Phys. Rev. Lett. **96** (10), 107401 (2006).

[77] H. Tao, A. C. Strikwerda, K. Fan, W. J. Padilla, X. Zhang, and R. D. Averitt, *Reconfigurable Terahertz Metamaterials*, Phys. Rev. Lett. **103** (14), 147401 (2009).

[78] N. Katsarakis, G. Konstantinidis, A. Kostopoulos, R. S. Penciu, T. F. Gundogdu, M. Kafesaki, E. N. Economou, T. Koschny, and C. M. Soukoulis, *Magnetic response of split-ring resonators in the far-infrared frequency regime*, Opt. Lett. **30** (11), 1348 (June 2005).

[79] C. Enrich, M. Wegener, S. Linden, S. Burger, L. Zschiedrich, F. Schmidt, J. Zhou, T. Koschny, and C. M. Soukoulis, *Magnetic Metamaterials at Telecommunication and Visible Frequencies*, Phys. Rev. Lett. **95**, 203901 (2005).

[80] S. Linden, C. Enrich, G. Dolling, M. W. Klein, J. Zhou, T. Koschny, C. M. Soukoulis, M. Burger, F. Schmidt, and M. Wegener, *Photonic Metamaterials: Magnetism at Optical Frequencies*, IEEE J. Sel. Top. Quantum Electron. **12**, 1097 (2006).

[81] T. P. Meyrath, T. Zentgraf, and H. Giessen, *Lorentz Model for Metamaterials: Optical Frequency Resonance Circuits*, Phys. Rev. B **75**, 205102 (2007).

[82] M. Husnik, M. W. Klein, N. Feth, M. König, J. Niegemann, K. Busch, S. Linden, and M. Wegener, *Absolute Extinction Cross-Section of Individual Magnetic Split-Ring Resonators*, Nature Photon. **2**, 614 (2008).

[83] S. Rill, M. C. Plet, M. Thiel, I. Staude, G. von Freymann, S. Linden, and M. Wegener, *Photonic metamaterials by direct laser writing and silver chemical vapour deposition*, Nat Mater **7** (7), 543 (2008).

[84] M. S. Rill, *Three-Dimensional Photonic Metamaterials by Direct Laser Writing and Advanced Metallization Techniques*, Ph.D. thesis, Karlsruhe Institute of Technology (KIT) (2010).

[85] G. Dolling, C. Enrich, M. Wegener, J. F. Zhou, and C. M. Soukoulis, *Cut-Wire Pairs and Plate Pairs as Magnetic Atoms for Optical Metamaterials*, Opt. Lett. **30**, 3198 (2005).

[86] T. D. Corrigan, P. W. Kolb, A. B. Sushkov, H. D. Drew, D. C. Schmadel, and R. J. Phaneuf, *Optical plasmonic resonances in split-ring resonator structures: an improved LC model*, Opt. Express **16** (24), 19850 (2008).

[87] C. Enrich, F. Pérez-Willard, D. Gerthsen, J. Zhou, T. Koschny, C. M. Soukoulis, M. Wegener, and S. Linden, *Focused-Ion-Beam Nanofabrication of Near-Infrared Magnetic Metamaterials*, Adv. Mater. **17**, 2547 (2005).

[88] T. J. Yen, W. J. Padilla, N. Fang, D. C. Vier, D. R. Smith, J. B. Pendry, D. N. Basov, and X. Zhang, *Terahertz Magnetic Response from Artificial Materials*, Science **303**, 1494 (2004).

[89] C. F. Klingshirn, *Semiconductor Optics* (Springer-Verlag, 2005), 2nd edition.

[90] M. I. Stockman, *Criterion for Negative Refraction with Low Optical Losses from a Fundamental Principle of Causality*, Phys. Rev. Lett. **98**, 177404 (2007).

[91] P. Kinsler and M. W. McCall, *Causality-Based Criteria for a Negative Refractive Index Must Be Used With Care*, Phys. Rev. Lett. **101**, 167401 (2008).

[92] Z. Liu, S. Durant, H. Lee, Y. Pikus, N. Fang, Y. Xiong, C. Sun, and X. Zhang, *Far-Field Optical Superlens*, Nano Letters **7** (2), 403 (2007).

[93] Z. Liu, H. Lee, Y. Xiong, C. Sun, and X. Zhang, *Far-Field Optical Hyperlens Magnifying Sub-Diffraction-Limited Objects*, Science **315** (5819), 1686 (2007).

[94] E. E. Narimanov and V. M. Shalaev, *Optics: Beyond diffraction*, Nature **447** (7142), 266 (2007).

[95] H. Helmholtz, *Über einige Gesetze der Verteilung elektrischer Ströme in körperlichen Leitern*, Ann. Phys. Chem. **89**, 211–233 (1853).

[96] H. Helmholtz, *Studien über elektrische Grenzschichten*, Ann.Phys. **7**, 337 (1879).

[97] A. J. Bard and L. R. Faulkner, *Electrochemical Methods: Fundamentals and Applications* (John Wiley & Sons, Inc, 2001), 2nd edition.

[98] G. Gouy, *Sur la constitution de la charge electrique ala surface d'un electrolyte*, J. Phys. Radium **9**, 457–468 (1910).

[99] D. L. Chapman, *A contribution to the theory of electrocapillarity*, Philosophical Magazine Series 6 **25** (148), 475 (1913).

[100] O. Stern, *Zur Theorie der elektrolytischen Doppelschicht*, Z. Elektrochem. **30**, 508 (1924).

[101] D. M. Kolb, *Reconstruction phenomena at metal-electrolyte interfaces*, Prog. Surf. Sci. **51** (2), 109 (1996).

[102] D. M. Kolb, *An atomistic view of electrochemistry*, Surf. Sci. **500** (1-3), 722 (2002).

[103] B. E. Conway, *Electrochemical oxide film formation at noble metals as a surface-chemical process*, Prog. Surf. Sci. **49** (4), 331 (1995).

[104] D. M. Kolb and J. Schneider, *Surface reconstruction in electrochemistry*, Electrochimica Acta **31** (8), 929 (1986).

[105] J. Schneider and D. M. Kolb, *Potential-induced surface reconstruction of Au(100)*, Surf. Sci. **193** (3), 579 (1988).

[106] M. Giesen, G. Beltramo, S. Dieluweit, J. Müller, H. Ibach, and W. Schmickler, *The thermodynamics of electrochemical annealing*, Surf. Sci. **595** (1-3), 127 (2005).

[107] R. J. Nichols, O. M. Magnussen, J. Hotlos, T. Twomey, R. J. Behm, and D. M. Kolb, *An in-situ STM study of potential-induced changes in the surface topography of Au(100) electrodes*, Journal of Electroanalytical Chemistry and Interfacial Electrochemistry **290** (1-2), 21 (1990).

[108] O. M. Magnussen, J. Hotlos, G. Beitel, D. M. Kolb, and R. J. Behm, *Atomic structure of ordered copper adlayers on single-crystalline gold electrodes*, in *J. Vac. Sci. Technol. B*, volume 9 (AVS, Boston, Massachusetts (USA), 1991).

[109] G. J. Cali, G. M. Berry, M. E. Bothwell, and M. P. Soriaga, *Electrochemical regeneration of clean and well-ordered Pd(111) surfaces*, Journal of Electroanalytical Chemistry **297** (2), 523 (1991).

[110] J. L. Stickney, I. Villegas, and C. B. Ehlers, *In situ restoration of atomically well-ordered copper single-crystal electrode surfaces*, Journal of the American Chemical Society **111** (16), 6473 (1989).

[111] L. B. Goetting, B. M. Huang, T. E. Lister, and J. L. Stickney, *Preparation of Au single crystals for studies of the ECALE deposition of CdTe*, Electrochimica Acta **40** (1), 143 (1995).

[112] M. H. Hölzle, T. Wandlowski, and D. M. Kolb, *Structural transitions in uracil adlayers on gold single crystal electrodes*, Surf. Sci. **335**, 281 (1995).

[113] M. Ruther, L.-H. Shao, S. Linden, J. Weissmuller, and M. Wegener, *Electrochemical restructuring of plasmonic metamaterials*, Appl. Phys. Lett. **98** (1), 013112 (2011).

[114] P. Mulvaney, *Surface Plasmon Spectroscopy of Nanosized Metal Particles*, Langmuir **12** (3), 788 (1996).

[115] D. M. Kolb, *UV techniques in the study of electrode surfaces*, Z. Phys. Chem. N.F. **154**, 179 (1987).

[116] R. Gupta, M. J. Dyer, and W. A. Weimer, *Preparation and characterization of surface plasmon resonance tunable gold and silver films*, J. Appl. Phys. **92** (9), 5264 (2002).

[117] L. Rayleigh, *On the equilibrium of liquid conducting masses charged with electricity*, Phil. Mag. **14**, 184 (1882).

[118] C. Novo and P. Mulvaney, *Charge-Induced Rayleigh Instabilities In Small Gold Rods*, Nano Lett. **7** (2), 520 (2007).

[119] N. Batina, A. S. Dakkouri, and D. M. Kolb, *The surface structure of flame-annealed Au(100) in aqueous solution: An STM study*, Journal of Electroanalytical Chemistry **370** (1-2), 87 (1994).

[120] W. Haiss, D. Lackey, J. K. Sass, and K. H. Besocke, *Atomic resolution scanning tunneling microscopy images of Au(111) surfaces in air and polar organic solvents*, J. Chem. Phys. **95** (3), 2193 (1991).

[121] J. Weissmüller, R. N. Viswanath, D. Kramer, P. Zimmer, R. Wurschum, and H. Gleiter, *Charge-Induced Reversible Strain in a Metal*, Science **300** (5617), 312 (2003).

[122] M. Smetanin, R. N. Viswanath, D. Kramer, D. Beckmann, T. Koch, L. A. Kibler, D. M. Kolb, and J. Weissmüller, *Surface Stress-Charge Response of a (111)-Textured Gold Electrode under Conditions of Weak Ion Adsorption*, Langmuir **24** (16), 8561 (2008).

[123] H.-J. Jin, X.-L. Wang, S. Parida, K. Wang, M. Seo, and J. Weissmüller, *Nanoporous Au–Pt Alloys As Large Strain Electrochemical Actuators*, Nano Lett. **10** (1), 187 (2010).

[124] Y. Umeno, C. Elsässer, B. Meyer, P. Gumbsch, and J. Weissmüller, *Reversible relaxation at charged metal surfaces: An ab initio study*, EPL (Europhysics Letters) **84** (1), 13002 (2008).

[125] C. Enkrich, *Metamaterials for Photonics*, Ph.D. thesis, University Karsruhe (TH) (2006).

[126] N. A. Feth, *Nonlinear Optics of Planar Metamaterial Arrays and Spectroscopy of Individual "Photonic Atoms"*, Ph.D. thesis, Karlsruhe Institute of Technology (KIT) (2010).

[127] *Data Sheet Heraeus Suprasil 3001 and 3002 .*

[128] C. Guillen and J. Herrero, *Comparison Study of ITO Thin Films Deposited by Sputtering at Room Temperature onto Polymer and Glass Substrates*, Thin Solid Films **480**, 129 (2005).

[129] D. C. Paine, T. Whitson, D. Janiac, R. Beresford, C. O. Yang, and B. Lewis, *A study of low temperature crystallization of amorphous thin film indium–tin–oxide*, J. Appl. Phys. **85** (12), 8445 (1999).

[130] J. George and C. S. Menon, *Electrical and optical properties of electron beam evaporated ITO thin films*, Surface and Coatings Technology **132** (1), 45 (2000).

[131] P. Rai-Choudhury (ed.), *SPIE Handbook of Microlithography, Micromachining, and Microfabrication* (SPIE, 1980).

[132] S. Yasin, D. G. Hasko, and H. Ahmed, *Fabrication of $< 5nm$ - Width Lines in Poly(methymethacrylate) Resist Using a Water: Isopropyl Alcohol Developer and Ultrasonically-Assisted Development*, Appl. Phys. Lett. **78**, 2760 (2001).

[133] A. A. Tseng, *Recent Developments in Micromilling Using Focused Ion Beam Technology*, J. Micromech. Microeng. **14**, R15 (2004).

[134] S. R. J. Brueck, *Optical and Interferometric Lithography – Nanotechnology Enablers*, Proc. IEEE **93**, 1704 (2005).

[135] S. Zhang, W. Fan, B. K. Minhas, A. Frauenglass, K. J. Malloy, and S. R. J. Brueck, *Midinfrared Resonant Magnetic Nanostructures Exhibiting a Negative Permeability*, Phys. Rev. Lett. **94**, 037402 (2005).

[136] M. Knoll and E. Ruska, *Das Elektronenmikroskop*, Zeitschrift für Physik **78**, 318 (1932).

[137] S. Kasap and P. Capper, *Handbook of Electronic and Photonic Materials* (Springer-Velag, 2006).

[138] G. F. Rempfer, *A theoretical study of the hyperbolic electron mirror as a correcting element for spherical and chromatic aberration in electron optics*, J. Appl. Phys. **67** (10), 6027 (1990).

[139] J. Zach and M. Haider, *Aberration correction in a low voltage SEM by a multipole corrector*, Nuclear Instruments and Methods in Physics Research Section A: Accelerators, Spectrometers, Detectors and Associated Equipment **363** (1-2), 316 (1995).

[140] E. Munro, J. Rouse, H. Liu, and L. Wang, *Aberration correction for electron beam inspection, metrology, and lithography*, volume 26 (AVS, 2008).

[141] Y. Zhu, H. Inada, K. Nakamura, and J. Wall, *Imaging Single Atoms Using Secondary Electrons with an Aberration-Corrected Electron Microscope*, Nat. Mater. **8**, 808 (2009).

[142] M. Deubel, *Three-Dimensional Photonic Crystals via Direct Laser Writing: Fabrication and Characterization*, Ph.D. thesis, University Karlsruhe (TH) (2006).

[143] D. H. Werner, D.-H. Kwon, I.-C. Khoo, A. V. Kildishev, and V. M. Shalaev, *Liquid crystal clad near-infrared metamaterials with tunable negative-zero-positive refractive indices*, Opt. Express **15** (6), 3342 (2007).

[144] X. Wang, D. H. Kwon, D. H. Werner, I. C. Khoo, A. V. Kildishev, and V. M. Shalaev, *Tunable optical negative-index metamaterials employing anisotropic liquid crystals*, Applied Physics Letters **91** (14), 143122 (2007).

[145] F. Zhang, L. Kang, Q. Zhao, J. Zhou, X. Zhao, and D. Lippens, *Magnetically tunable left handed metamaterials by liquid crystal orientation*, Opt. Express **17** (6), 4360 (2009).

[146] T. Driscoll, G. O. Andreev, D. N. Basov, S. Palit, S. Y. Cho, N. M. Jokerst, and D. M. Smith, *Tuned permeability in terahertz split-ring resonators for devices and sensors*, Applied Physics Letters **91** (6), 062511 (2007).

[147] H.-T. Chen, J. F. O'Hara, A. K. Azad, A. J. Taylor, R. D. Averitt, D. B. Shrekenhamer, and W. J. Padilla, *Experimental demonstration of frequency-agile terahertz metamaterials*, Nature Photon. **2** (5), 295 (2008).

[148] M. J. Dicken, K. Aydin, I. M. Pryce, L. A. Sweatlock, E. M. Boyd, M. Walavalkar, J. Ma, and H. A. Atwater, *Frequency tunable near-infrared metamaterials based on VO2 phase transition*, Opt. Express **17** (20), 18330 (2009).

[149] T. Driscoll, H.-T. Kim, B.-G. Chae, B.-J. Kim, Y.-W. Lee, N. M. Jokerst, S. Palit, D. R. Smith, M. Di Ventra, and D. N. Basov, *Memory Metamaterials*, Science **325** (5947), 1518 (2009).

[150] Z. L. Samson, K. F. MacDonald, F. De Angelis, B. Gholipour, K. Knight, C. C. Huang, E. Di Fabrizio, D. W. Hewak, and N. I. Zheludev, *Metamaterial electro-optic switch of nanoscale thickness*, Applied Physics Letters **96** (14), 143105 (2010).

[151] H. Tao, A. Strikwerda, K. Fan, W. Padilla, X. Zhang, and R. Averitt, *MEMS Based Structurally Tunable Metamaterials at Terahertz Frequencies*, Journal of Infrared, Millimeter and Terahertz Waves , 110.1007/s10762-010-9646-8 (2010).

[152] X.-J. He, Y. Wang, J.-M. Wang, and T.-L. Gui, *MEMS switches controlled multi-split ring resonator as a tunable metamaterial component*, Microsystem Technologies **16**, 1831, 10.1007/s00542-010-1126-5 (2010).

[153] E. Feigenbaum, K. Diest, and H. A. Atwater, *Unity-Order Index Change in Transparent Conducting Oxides at Visible Frequencies*, Nano Lett. , (2010).

[154] D. M. Kolb and R. Kötz, *Electroreflectance spectra of Ag(111) electrodes*, Surface Science **64** (1), 96 (1977).

[155] R. Kötz, D. M. Kolb, and J. K. Sass, *Electron density effects in surface plasmon excitation on silver and gold electrodes*, Surf. Sci. **69** (1), 359 (1977).

[156] R. Kötz and D. M. Kolb, *Electroreflectance of copper, silver, and gold single crystal electrodes*, Z. Phys. Chem. N.F. **112**, 69 (1978).

[157] C. M. Vitus and A. J. Davenport, *In Situ Scanning Tunneling Microscopy Studies of the Formation and Reduction of a Gold Oxide Monolayer on Au(111)*, Journal of The Electrochemical Society **141** (5), 1291 (1994).

[158] T. Weiss, G. Granet, N. A. Gippius, S. G. Tikhodeev, and H. Giessen, *Matched coordinates and adaptive spatial resolution in the Fourier modal method*, Opt. Express **17** (10), 8051 (2009).

[159] S. Essig and K. Busch, *Generation of adaptive coordinates and their use in the Fourier Modal Method*, Opt. Express **18** (22), 23258 (2010).

[160] M. A. Noginov, G. Zhu, A. M. Belgrave, R. Bakker, V. M. Shalaev, E. E. Narimanov, E. Herz, T. Suteewong, and U. Wiesner, *Demonstration of a Spaser-Based Nanolaser*, Nature **460**, 1110 (2009).

[161] E. Plum, V. A. Fedotov, P. Kuo, D. P. Tsai, and N. I. Zheludev, *Towards the lasing spaser: controlling metamaterial optical response with semiconductor quantum dots*, Opt. Express **17** (10), 8548 (2009).

[162] N. Meinzer, M. Ruther, S. Linden, C. M. Soukoulis, G. Khitrova, J. Hendrickson, J. D. Olitzky, H. M. Gibbs, and M. Wegener, *Arrays of Ag split-ring resonators coupled to InGaAs single-quantum-well gain*, Opt. Express **18** (23), 24140 (2010).

[163] D. A. Bobb, G. Zhu, M. Mayy, A. V. Gavrilenko, P. Mead, V. I. Gavrilenko, and M. A. Noginov, *Engineering of low-loss metal for nanoplasmonic and metamaterials applications*, Appl. Phys. Lett. **95** (15), 151102 (2009).

[164] J. Rodriguez-Fernandez, A. M. Funston, J. Perez-Juste, R. A. Alvarez-Puebla, L. M. Liz-Marzan, and P. Mulvaney, *The effect of surface roughness on the plasmonic response of individual sub-micron gold spheres*, Phys. Chem. Chem. Phys. **11** (28), 5909 (2009).

[165] A. B. Dahlin, T. Sannomiya, R. Zahn, G. A. Sotiriou, and J. Vörös, *Electrochemical Crystallization of Plasmonic Nanostructures*, Nano Lett. , null (2011).

[166] M. A. Schneeweiss and D. M. Kolb, *Oxide formation on Au(111): An in situ STM study*, Solid State Ionics **94** (1-4), 171 (1997).

[167] G. Lippmann, *Relations entre les phénomènes électriques et capíllaires.*, Ann. de chim. et de phys. **5**, 494 (1875).

[168] G. Zosi, *Die Bestimmung der Korngrösse der dünnen Aufdampfschichten aus der Analyse von Röntgeninterferenzlinienprofilen*, Thin Solid Films **3** (1), R13 (January 1969).

Acknowledgments

rections of this thesis, fruitful discussions and a good friendship, which will certainly outlast the great time of working together.

My last words are dedicated to my inner circle, my best friend and companion Ronny, who attended me through my times of studying - physics and life, my partner Hanna for her love and support and my family and friends. All of them keep me grounded in all facets of my life.